

Discovery of a Novel, Selective Inhibitor of the Kir4.1/5.1
Heterotetramer, Development of a Novel mGlu4 PAM Chemotype,
and Progress Towards the Total Synthesis of Thiocladospolide A

By

Caitlin N. Kent

Dissertation

Submitted to the Faculty of the

Graduate School of Vanderbilt University

in partial fulfillment of the requirements

for the degree of

DOCTOR OF PHILOSOPHY

in

Chemistry

August 13, 2021

Nashville, Tennessee

Approved:

Craig W. Lindsley, Ph.D., Chair

Jerod Denton, Ph.D.

Steven Townsend, Ph.D.

David Cliffler, Ph.D.

To everyone who thought I could

ACKNOWLEDGMENTS

The research described herein was supported by the NIH division of mental health, and the William K. Warren, Jr. Chair in Medicine. I would like to thank these wonderful organizations, whom without their generosity and commitment to the advancement of science for the improvement of societal health, this work would not have been possible.

First, I would like to thank Dr. Steven Townsend, Dr. David Cliffler, and Dr. Jerod Denton for graciously agreeing to serve on my committee. I would like to thank my graduate advisor and committee chair Dr. Craig Lindsley, who gave me the opportunity to come to Vanderbilt to train in his laboratory. Before I met Dr. Lindsley, I was navigating how to move past my previous graduate school experience, and in this time, it became apparent to me that so much of my identity was rooted in being a scientist. Dr. Lindsley gave me back that identity along with world-class training, and it stands as the greatest kindness anyone has ever done for me. Thank you, Craig, for your unwavering support and encouragement. I promise to treat every single person I encounter with the same kindness, grace, and integrity you have always afforded me.

In regard to the work enclosed, it would not have been possible without the help from other collaborating labs. It was a pleasure to collaborate with Dr. Samantha McCleanhan and Dr. Jerod Denton on the Kir4.1/5.1 project. The work described in Chapter II was started by my colleague and dear friend Dr. Mark Fulton, and I am grateful to Dr. Colleen Niswender, Matthew Loch, and the MolPharm team for their help in completing this project. Further, the animal behavioral data in Chapter II was executed by

Dr. Jon Dickerson, Kaylee Stilwell, and Dr. Jerri Rook. Thank you all, for contributing to this final work on an unfavorable timeline.

I'd also like to thank all the Lindsley lab members, past and present, campus and Cool Springs. Dr. Bruce Melancon was my connection to the Lindsley lab and facilitated my transition to the WCNDD. Along with Bruce, I also had the pleasure of working with Paul Spearing and the mGlu team. I learned more about chemistry in four months working for Bruce and Paul than I had in my previous four years of graduate school. I would also like to thank the DMPK team lead by Dr. Annie Blobaum and Dr. Olivier Boutaud. Further, Nathan Kett and Nathalie Boutaud made life on campus easier and ensured the success of the enclosed work. My campus labmates Dr. Carson Reed, Dr. Jeanette Bertron, and Jacob Kalbfleisch, deserve a special thanks for their patience and knowledge, but most importantly for the laughter we shared during our time together. Jeanette is one of my closest friends and I am so grateful we found our way to each other. Finally, to my "Cool Springs friends," I am grateful for your acceptance and friendship. I'd like to formally apologize for every trivia question I've butchered, including the Thousand Island mishap of 2019 (the most popular salad dressing before 1992 was Italian).

Outside of Vanderbilt, I am forever indebted to my best friends who are also scientists: Dr. Elizabeth Slocum, Dr. Matthew Rhodes, Kristen Burns, and Dr. Micayla Bowman. Thank you for providing guidance and advice in both science and life. I am in awe of the support system I have manage to build in the last decade of my life. Additionally, I would like to thank all my friends and family who have been my cheerleaders throughout my undergraduate and graduate career. Thank you for being so

understanding and never making me feel for missing holidays, birthdays, graduations, weddings, and trips to Texas.

I owe special thanks to my immediate family. My maternal grandparents, Jack and Kathy, ensured that I would have access to the education I desired, and because of this kindness I have been able to take any opportunity presented to me. My paternal grandparents, Don and Jo, cultured my creative spirit, which has proved invaluable in my success as a scientist, but particularly as an organic chemist. My family, Chris, Kristy and Jack Kent, have been my greatest source of inspiration for the last five years. Thank you for the work ethic and moral compass you gave me. Every victory of mine, is yours. I you!

TABLE OF CONTENTS

	Page
DEDICATION.....	ii
ACKNOWLEDGMENTS.....	iii
LIST OF TABLES.....	x
LIST OF FIGURES.....	x
LIST OF SCHEMES.....	xi
LIST OF ABBREVIATIONS.....	xiii
CHAPTER	
I. Discovery and Development of a Novel, Selective Inhibitor of the Inward Rectifying Potassium Channel 4.1/5.1 Heterotetramer	
Background and Introduction	
Structure and Function of Inward Rectifying Potassium Channels... 1	
K _{ir} 4.1 and K _{ir} 4.1/5.1 Channels and Their Pharmacological Relevance..... 4	
Small Molecule Pharmacology of Kir4.1/5.1 Channels..... 6	
Conclusions..... 7	
Materials and methods	
General Synthetic Methods and Instrumentation..... 7	
Molecular Biology and Cell Line Construction..... 9	
Primary Screening Quantitative Thallium Flux Assay..... 10	
Whole-cell Patch Clamp Electrophysiology..... 11	

<i>In Vitro</i> DMPK Methods: Intrinsic Clearance in Rat Liver Microsomes.....	12
Rat Plasma Protein Binding.....	13
Rat Brain Homogenate Binding.....	14
LC/MS/MS Analysis of Samples from <i>In Vitro</i> Assays.....	15
<i>In vivo</i> PK methods.....	16
Single Time Point Tissue Distribution Studies	16
LC/MS/MS Bioanalysis of Samples from <i>In Vivo</i> Assays.....	17
Development of an Improved <i>In Vitro</i> Tool Compound, VU0493690, for Inhibition of the Heterotetrameric Kir4.1/5.1 Receptor	
Medicinal Chemistry Strategy for the Exploration of VU0493690 (1.4).....	18
Modification of the Eastern Aryl Sulfonamide: Analogs 1.8-1.21 ...	19
Exploration of the Central Piperazine Core: Analogs 1.24-1.29	23
Modification of the Western Aryl Ring: Analogs 1.31-1.51	26
Re-investigation of the Central Piperazine: Analogs 1.52-1.57	31
Exploration Conformational Constrain: Analogs 1.58-1.61	34
Assessment of VU6036720 as a Viable Tool Compound.....	36
Summary and Future Directions.....	38
Experimental methods	
General Synthetic Methods and Instrumentation.....	39
II. Development of a Novel Metabotropic Glutamate Receptor 4 Positive Allosteric Modulator Chemotype	
Background and Introduction	
G Protein-Coupled Receptors: Metabotropic	
Glutamate Receptors.....	47
Orthosteric vs. Allosteric Ligands for mGlu Receptors.....	49
mGlu ₄ and Parkinson's Disease.....	52
Conclusions.....	55
Materials and Methods	
General synthetic Methods and Instrumentation.....	56

GIRK-mediated Thallium Flux Assay.....	57
<i>In vitro</i> DMPK Methods: Intrinsic Clearance in Rat Liver Microsomes.....	59
Rat Plasma Protein Binding.....	60
Rat Brain Homogenate Binding.....	61
LC/MS/MS Analysis of Samples from <i>In Vitro</i> Assays.....	62
<i>In vivo</i> PK Methods.....	62
Single Time Point Tissue Distribution Studies.....	63
LC/MS/MS bioanalysis of samples from <i>in vivo</i> assays.....	64
<i>In vivo</i> Behavioral Methods.....	64
Haloperidol Induced Catalepsy.....	65
Development of an Improved <i>In Vitro</i> Tool Compound, VU0493690, for Inhibition of the Heterotetrameric Kir4.1/5.1 Receptor	
Medicinal Chemistry Strategy.....	66
Improved Synthetic Methods for Accessing the Oxo-thiazepine core.....	67
SAR of the Arene Ring: Analogues 2.15-2.29	71
Evaluating the Importance of the Oxo-thiazepine core.....	76
Assessment of VU0622296 (2.20) as a Viable Tool Compound...76	
Summary and Future Directions.....	79
Experimental Methods	
General Synthetic Methods and Instrumentation.....	80
III. Progress Towards the Total Synthesis of Thiocladospolide A	
Background and Introduction	
Natural Products in Antibiotic Drug Discovery.....	85
Sulfur-containing Macrolides and the Discovery of the Thiocladospolides.....	85
A Failed Synthetic Route to Thiocladospolide A.....	89
Conclusions and Future Directions.....	93
Experimental Methods	
General Synthetic Methods and Instrumentation.....	96

Appendices

A. Relevant Spectra for Chapter I.....	105
B. Relevant Spectra for Chapter II.....	120
C. Relevant Spectra for Chapter III.....	129
References.....	142

LIST OF TABLES

Chapter I

Table	Page
1.1 SAR of the Eastern Aryl Sulfonamide: Analogs 1.8-1.21	21
1.2 SAR of the Central Piperazine Core: Analogs 1.24-1.29	25
1.3 SAR of the Western Aryl Ring: Analogs 1.31-1.44	27
1.4 SAR of the Western Aryl Ring: Analogs 1.45-1.51	30
1.5 Re-investigation of the Central Piperazine: Analogs 1.52-1.57	32
1.6 Conformationally Constrained Analogs of 1.32 and 1.4	34
1.7 <i>In Vitro</i> and <i>In Vivo</i> DMPK Profiles of 1.55	37

Chapter II

Table	Page
2.1 SAR of the arene ring: analogues 2.15-2.26	73
2.2 SAR of the arene ring: analogues 2.26-2.29	75
2.3 <i>In Vitro</i> and <i>In Vivo</i> DMPK Profiles of 2.20 and 2.21	77

Chapter III

Table	Page
3.1 Reported Antimicrobial Activities of Thiocladospolides A-D.....	88

LIST OF FIGURES

Chapter I

Figure	Page
1.1 Description of the inward-rectifier (K_{ir}) subtype of potassium channels.....	2
1.2 Structures of known $K_{ir}4.1$ small molecule modulators.....	6
1.3 Medicinal chemistry strategy for the exploration of VU0493690 (1.4).....	18
1.4 Manual patch clamp experiments with VU6036720 (1.55).....	36

Chapter II

Figure	Page
2.1 General structure of an mGlu receptor.....	48
2.2 Structures of reported mGlu ₄ PAMs 2.1–2.4	55
2.3 Structures of VU0544412 (2.6) and VU6014297 (2.7).....	66
2.4 Comparison of the oxo-thiazepine scaffold and Lundbeck candidate, 2.3	71
2.5 Thiomorpholine derivatives 2.30 and 2.31	76
2.6 Anti-PD activity of VU6022296 (2.20).....	78
2.7 Summary of SAR that lead to the discovery of 2.20	

Chapter III

Figure	Page
3.1 Structures of thio-adduct natural products.....	86
3.2 Structures of Thiocladospolides A-D.....	87
3.3 Retrosynthetic analysis of Thiocladospolide A.....	90
3.4 Revised synthetic route to Thiocladospolide A.....	95

LIST OF SCHEMES

Chapter I

Scheme	Page
1.1 SAR of the Eastern Aryl Sulfonamide: Synthesis of Analogs 1.8-1.21	19
1.2 SAR of the Central Piperazine Core: Synthesis of Analogs 1.24-1.29	24
1.3 SAR of the Western Aryl Ring: Synthesis of Analogs 1.31-1.51	26
1.4 Synthesis of 1.62	35

Chapter II

Scheme	Page
2.1 Original synthesis of oxo-thiazepine VU0544412 analogs.....	68

2.2	Improved synthesis of the oxo-thiazepine from L-cysteine and 2.10	69
2.3	Synthetic route to access HMBT (2.11) and the HMBT ester (2.10).....	69
2.4	Modified synthesis from Scheme 2.1	70
2.5	Synthesis of 2.15-2.31	71

Chapter III

Scheme		Page
3.1	Furan oxidation strategy to yield 4-oxo-2-alkeneoic acid 3.14	91
3.2	Direct furan oxidation strategy to yield 4-oxo-2-alkeneoic acid 3.14	92
3.3	Modified HWE with glyoxylic acid monohydrate to access 3.14	92
3.4	Improved generation of β -ketophosphonate 3.19	93
3.5	Steglich esterification conditions yielded 3.12 , which failed to undergo RCM.....	94

LIST OF ABBREVIATIONS

°C	Degrees Celsius
6-OHDA	Oxidopamine
7-TM	Seven-transmembrane domain
AC	Adenylate cyclase
Acetyl-CoA	Acetyl coenzyme A
AM	Allosteric modulator
Ar	Aryl
ATP	Adenosine triphosphate
BBB	Blood-brain barrier
BG	Basal ganglia
BHB	Brain homogenate binding
Bn	Benzyl
Boc	<i>tert</i> -butyloxycarbonyl
cAMP	Cyclic adenosine monophosphate
CHO	Chinese hamster ovary
CL _{HEP}	Predicted hepatic clearance
CL _{INT}	Intrinsic clearance

Cn	Concentration
cLogP	Partition coefficient between n-octanol and water
CNS	Central Nervous System
CRC	Concentration response curve
CRD	Cysteine rich domain
DAG	Diacyl glycerol
DBS	Deep brain stimulation
DCC	<i>N,N'</i> -dicyclohexylcarbodiimide
DCM	Dichloromethane
DIEA	<i>N,N</i> -Diisopropylethylamine
DMF	Dimethylformamide
DMPK	Drug metabolism and pharmacokinetics
DMSO	Dimethylsulfoxide
EC50	Half maximal effective concentration
ESI	Electrospray ionization
Et3N	Triethylamine
Et2O	Diethyl ether
EtOAc	Ethyl acetate

EtOH	Ethanol
F	Bioavailability
FDA	Food and drug administration
fu	Fraction unbound
G	Guanine nucleotide-binding proteins
GABA	γ -aminobutyric acid
GPCR	G protein-coupled receptor
GTP	Guanosine triphosphate
H ₂	Hydrogen gas
H ₂ O	Water
HATU	1-[Bis(dimethylamino)methylene]-1 <i>H</i> -1,2,3-triazolo[4,5- <i>b</i>]pyridinium 3-oxid hexafluorophosphate
HEK	Human embryonic kidney
HEPES	4-(2-hydroxyethyl)-1-piperazineethanesulfonic acid
HIC	Haloperidol induced catalepsy
HMBT	2-(2'-hydroxy-4'-methoxyphenyl)benzothiazole
HPLC	High-performance liquid chromatography
HRMS	High-resolution mass spectrometry

HTS	High-throughput screening
IC50	Half maximal inhibitory concentration
I.P.	Intraperitoneal
IP3	Inositol 1,4,5-triphosphate
IV	Intravenous
K	Potassium
K _{ir}	Inward-rectifying potassium channel
K _v	Voltage gated potassium channel
K ₂ CO ₃	Potassium carbonate
K ₃ PO ₄	Potassium phosphate tribasic
K _p	Brain:plasma partition coefficient
K _{p,uu}	Unbound brain:plasma partition coefficient
L-AP4	L-2-amino-4-phosphonobutyric acid
L-DOPA	Levodopa
LC/MS	Liquid chromatography / Mass spectrometry
LUMO	Lowest unoccupied molecular orbital
M	Muscarinic receptor
MeCN	Acetonitrile

MED	Mean effective dose
MeOH	Methanol
Mg	Magnesium
MgCl ₂	Magnesium chloride
mGlu	Metabotropic glutamate
MgSO ₄	Magnesium sulfate
MPTP	1-methyl-4-phenyl-1,2,3,6-tetrahydropyridine
MRM	Multiple reaction monitoring
MS	Molecular sieves
MW	Molecular weight
N/A	Not applicable
NF	No fit
Na ⁺	Sodium
NaHCO ₃	Sodium bicarbonate
NAL	Neutral allosteric ligand
NAM	Negative allosteric modulator
NaOH	Sodium hydroxide
<i>n</i> -BuLi	<i>n</i> -butyl lithium

NMR	Nuclear magnetic resonance
PAM	Positive allosteric modulator
Pd/C	Palladium on carbon
Pd ₂ (dba) ₃	Tris(dibenzylideneacetone)dipalladium (0)
PGP	P-glycoprotein
PEG	Polyethylene glycol
PK	Pharmacokinetic
PKA	Protein kinase A
PLC	Phospholipase C
PO	Oral administration
PPB	Plasma protein binding
PSA	Polar Surface Area
PyCIU	Chlorodipyrrolidinocarbenium hexafluorophosphate
PyBroP	Bromotripyrrolidinophosphonium hexafluorophosphate
Pyr	Pyridine
Rt	Room temperature
SAR	Structure-activity relationship
SD	Sprague-Dawley

SEM	Standard error of mean
SUR	Sulfonylurea receptor
$t_{1/2}$	Half life
T3P	Propylphosphonic anhydride
TFA	Trifluoroacetic acid
THF	Tetrahydrofuran
TI	Thallium
TLC	Thin-layer chromatography
TOF	Time of flight
Tol	Toluene
VFD	Venus flytrap domain
VICB	Vanderbilt Institute of Chemical Biology
VOID	Vanderbilt University identification number
Zn	Zinc

CHAPTER I

DISCOVERY AND DEVELOPMENT OF A NOVEL, SELECTIVE INHIBITOR OF THE INWARD RECTIFYING POTASSIUM CHANNEL 4.1/5.1 HETEROTETRAMER

Background and Introduction

Structure and Function of Inward Rectifying Potassium Channels

The voltage-dependent changes that result from the conductance of biologically relevant cations via their channels underlie the electrical signals or action potentials that are essential to all excitable processes, and to life itself.^{1, 2} Potassium (K^+) channels are the most widely distributed, transmembrane ion channels and mediate the flow of K^+ ions across the cellular membrane. The superfamily of channels most often set or reset the resting potential of many cell types.³ For example, in excitable cells like neurons or myocytes, the delayed counter flow of K^+ down its electrochemical gradient by voltage-gated K^+ channels into the extracellular space shapes the action potential (**Figure 1.1A**).⁴

There are two broad classes of K^+ channels defined by transmembrane topology: the six-transmembrane-helix voltage-gated (K_v) and the two-transmembrane-helix inward-rectifier (K_{ir}) subtypes (**Figure 1.1B**).³ In contrast to K_v channels, inwardly rectifying K_{ir} channels allow K^+ to move more easily into the cells than into the extracellular space.⁵ K_{ir} channels derive their name, inwardly-rectifying, from the current-voltage relationship. When the current through the channel is plotted as a function of membrane potential, the inward current, or negative current, is typically much larger than the positive or 'outward' current (**Figure 1.1C**).⁶ This property is

referred to as inward rectification, to distinguish it from the classical ‘outward’ rectification expected of a passive K_v pore in the presence of high internal and low external potassium.⁷ The K_{ir} family members are divided into weak and strong inward rectifiers. Strongly rectifying K_{ir} channels play an important role in controlling resting potential and excitability but contribute little to the action potential itself. In contrast, weak inward rectifiers will both stabilize the resting potential and shorten the action potential.⁷⁻⁹

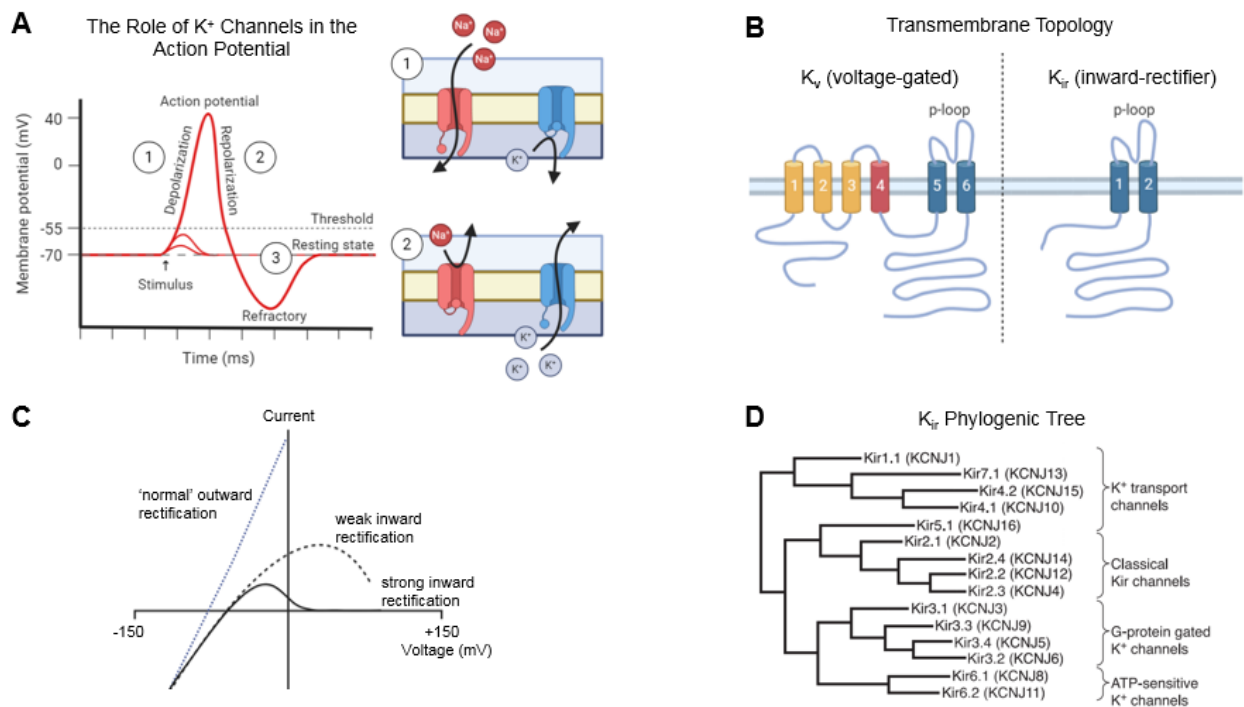


Figure 1.1: (A) Illustration of how the flow of K^+ ions across the cellular membrane shapes the action potential. (B) Transmembrane topology of the six-transmembrane-helix voltage-gated (K_v) and the two-transmembrane-helix inward-rectifier (K_{ir}) subtypes. (C) The current-voltage relationship of outward and inward rectifying K^+ channels (D) Phylogenetic tree of the K_{ir} family. All components of this figure were generated using BioRender.

K_{ir} channels have evolved distinct voltage-independent mechanisms for opening and closing, including gating by G proteins, pH, and ATP.⁸ Seven structurally distinct subfamilies of the K_{ir} family have been identified in mammals with 16 gene members that can be classified into four functional groups: classical K_{ir} channels (K_{ir}2.X) are constitutively active, G protein-gated K_{ir} channels (K_{ir}3.X) are regulated by G protein-coupled receptors, ATP-sensitive K⁺ channels (K_{ir}6.X) are tightly linked to cellular metabolism, and K⁺ transport channels (K_{ir}1.X, K_{ir}4.X, K_{ir}5.X, and K_{ir}7.X) (**Figure 1.1D**).¹⁰

The primary structure of the two transmembrane subunit is insufficient to form a complete ion channel, thus functional K_{ir} channels are made up of four subunits in a tetrameric complex.¹¹ The homology between the K_{ir} subunits allow for the formation of both homo- and heterotetrameric combinations to form a functional channel.

Heterotetramerization typically occurs between two members of the same K_{ir} subfamily, for example, K_{ir}2.1 is known to complex with other K_{ir}2.X subfamily members K_{ir}2.2, K_{ir}2.3, and K_{ir}2.4.^{12, 13} However, an exception to this rule is the K_{ir}4.1/5.1 channel, which is discussed in detail in subsequent sections. Heterotetrameric assemblies have been shown to have distinct properties, which further broadens the functional range of K_{ir} channels in different cell types.¹⁴

K_{ir} channels are found across several cell types, including macrophages, cardiac and kidney cells, leukocytes, neurons, and endothelial cells.⁸ Gain- or loss-of-function mutations in several K_{ir} family members are associated with human diseases, which positions them to be potentially useful pharmacological targets.¹⁵ For example, inhibitory sulfonylurea receptor (SUR) ligands that block the activity of K_{ATP} channels (comprised of K_{ir}6.2/SUR1 subunits) channels in pancreatic beta cells stimulate insulin secretion

and promote blood glucose homeostasis in people with type II diabetes.¹⁶ However, the dearth of pharmacological tool compounds that are potent and selective enough to modulate specific subtypes of K_{ir} channels has been a critical barrier to progress in this area.¹⁷

K_{ir}4.1 and K_{ir} 4.1/5.1 Channels and Their Pharmacological Relevance

Homotetrameric $K_{ir}4.1$ and heterotetrameric $K_{ir}4.1/5.1$ channels are two subtypes of K_{ir} channels thought to hold therapeutic potential for treating neurological and vascular diseases. $K_{ir}4.1$ forms functional homotetrameric channels on the plasma membrane when expressed in a heterologous *in vitro* expression system and in native tissues.¹⁸ In contrast, $K_{ir}5.1$ homotetramers have no function but can form functional heteromeric channels with $K_{ir}4.1$ (or $K_{ir}4.2$) *in vivo*, whose function differ greatly from the $K_{ir}4.1$ homotetramer.^{8, 19}

Homotetrameric $K_{ir}4.1$ channels are expressed primarily in brain astrocytes and glial cells where they help remove extracellular potassium released from actively firing neurons, in a process called spatial potassium buffering.^{20, 21} Changes in the expression levels of $K_{ir}4.1$ and associated extracellular potassium levels have been found in models of clinical depression, ischemic stroke, and Huntington's disease, suggesting a mechanistic link between $K_{ir}4.1$ and these diseases.²²⁻²⁴ $K_{ir}4.1$ channels have also been implicated in the behavioral and respiratory disturbances in Rett syndrome, although their specific contributions in this multigenic disease is unclear.²⁵ Further, loss-of-function mutations to $K_{ir}4.1$ (*KCNJ10*) lead to SeSAME/EAST syndrome, which is

characterized by neurological dysfunction (epilepsy, ataxia, and sensorineural deafness) and renal salt wasting.²⁶

Similarly, the Kir4.1/5.1 channel has been detected in various tissues including the kidney and brain. Heteromeric Kir4.1/5.1 channels are the dominant subtype expressed in the renal tubule. Although they appear to be expressed throughout most of the nephron, Kir4.1/5.1 channels play especially important roles in regulating sodium chloride and potassium balance by the distal convoluted kidney (DCT).^{27, 28} In the DCT, Kir4.1/5.1 channels appear to regulate the phosphorylation state and hence activity of the electroneutral sodium-chloride cotransporter, NCC, through a membrane potential-intracellular chloride-WNK kinase-SPAK kinase-dependent pathway.²⁹

As additional studies become available discerning the physiological roles of Kir4.1 and Kir4.1/5.1, the potential therapeutic value of this target has become apparent. For example, the importance of Kir4.1 and Kir4.1/5.1 channels in humans was definitively established with the discovery that loss-of-function mutations in *KCNJ10* cause EAST/SeSAME syndrome.³⁰ It is postulated that small-molecule activators might rescue the function of mutant Kir4.1/5.1 channels in SeSAME/EAST syndrome patients carrying specific mutations in *KCNJ10*. Further, the upregulation of distal nephron sodium chloride reabsorption capacity in the setting of loop diuretic resistance suggests that peripherally restricted Kir4.1/5.1-specific inhibitors might help reduce extracellular fluid volume and edema in patients with congestive heart failure and chronic kidney disease.²⁷ However, fully elucidating these phenomena is inhibited by the lack of potent, selective, small molecule tool compounds for Kir4.1 and Kir4.1/5.1.

Small Molecule Pharmacology of Kir4.1/5.1 Channels

Currently, the molecular pharmacology of both Kir4.1 and Kir4.1/5.1 channels is virtually undeveloped. The only selective inhibitor of homomeric Kir4.1 known to date is VU0134992, disclosed by the Denton lab in 2018.¹⁷ Otherwise, homomeric Kir4.1 channels are known to be inhibited by the selective serotonin reuptake inhibitor fluoxetine, and the tricyclic antidepressants amitriptyline and nortriptyline (**Figure 1.2**).^{31, 32} Unfortunately, these compounds are relatively weak inhibitors (i.e. IC₅₀s in the tens of micromolar) of Kir4.1 and exhibit broad inhibitory activity toward several other members of the Kir channel family, including Kir4.1/5.1.

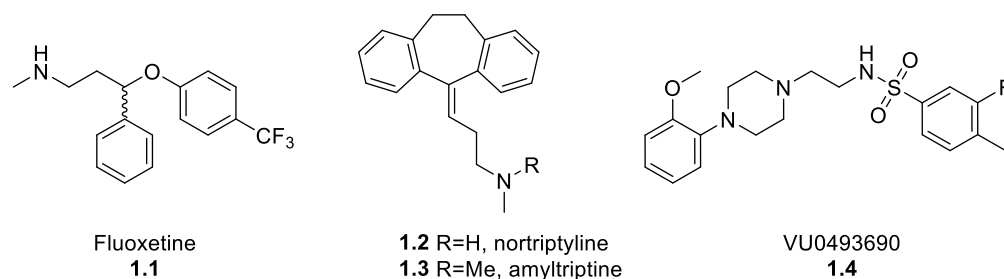


Figure 1.2: Structures of known Kir4.1 modulators, **1.1-1.3**, and the first Kir4.1/5.1 inhibitor VU0493690, (**1.4**) discovered by a HTS in the Denton lab.

In an effort to identify novel small-molecule modulators selective for Kir4.1/5.1, the Denton lab conducted a high-throughput screen (HTS) of nearly 6,900 compounds from the Vanderbilt Institute of Chemical Biology (VICB) chemical library. Both potentiators and inhibitors were identified in the screen, with VU0493690 (**1.4**) being the most potent inhibitor. In Kir4.1/5.1 thallium (Tl⁺) flux assays developed by the Denton lab, **1.4** dose-dependently inhibited Kir4.1/5.1 activity with an IC₅₀ of 3.2 μM (CI: 2.7-3.8 μM), which is approximately 6-fold more potent than fluoxetine (IC₅₀=19.5 μM; CI: 12.1-

31.3 μM). In gold-standard patch clamp experiments, **1.4** inhibited $\text{K}_{\text{ir}}4.1/5.1$ currents at -120 mV with an IC_{50} of 0.96 μM (CI: 0.25-1.6 μM). At concentrations ranging between 0.3 nM to 30 μM , **1.4** exhibits a greater than 30-fold improvement in selectivity for $\text{K}_{\text{ir}}4.1/5.1$ over homotetrameric $\text{K}_{\text{ir}}4.1$ channels, $\text{K}_{\text{ir}}1.1$, $\text{K}_{\text{ir}}2.1$, $\text{K}_{\text{ir}}2.2$, $\text{K}_{\text{ir}}2.3$, $\text{K}_{\text{ir}}4.2$, $\text{K}_{\text{ir}}6.2/\text{SUR1}$, $\text{K}_{\text{ir}}6.1/\text{SUR2b}$ and $\text{K}_{\text{ir}}7.1$ in established TI^+ -flux assays. Thus, **1.4** is the first potent and selective $\text{K}_{\text{ir}}4.1/5.1$ channel inhibitor known to date and is an excellent starting point for medicinal chemistry efforts.

Conclusions

Beginning with **1.4**, we will conduct an optimization campaign through traditional medicinal chemistry techniques to improve its inhibitory activity at $\text{K}_{\text{ir}}4.1/5.1$, while maintaining its selectivity over the $\text{K}_{\text{ir}}4.1$ homotetramer and other subfamily members. Structure-activity relationships (SAR) and drug metabolism and pharmacokinetic (DMPK) studies will guide our medicinal chemistry approaches, as there is no known crystal structure for this family of K^+ channels. In collaboration with the Denton lab, the activity of lead compounds will be confirmed in manual patch clamp experiments and single channel analysis. The following chapter will summarize our efforts that led to the discovery of a potent and selective *in vitro* tool compound, and the subsequent efforts to address its unfavorable DMPK profile.

Materials and Methods

General Synthetic Methods and Instrumentation

All NMR spectra were recorded on a 400 MHz AMX Bruker NMR spectrometer. ^1H and ^{13}C chemical shifts are reported in δ values in ppm downfield with the deuterated

solvent as the internal standard. Data are reported as follows: chemical shift, multiplicity (s = singlet, d = doublet, t = triplet, q = quartet, b = broad, m = multiplet), integration, coupling constant (Hz). Low resolution mass spectra were obtained on an Agilent 6120 or 6150 with ESI source. MS parameters were as follows: fragmentor: 70, capillary voltage: 3000 V, nebulizer pressure: 30 psig, drying gas flow: 13 L/min, drying gas temperature: 350 °C. Samples were introduced via an Agilent 1290 UHPLC comprised of a G4220A binary pump, G4226A ALS, G1316C TCC, and G4212A DAD with ULD flow cell. UV absorption was generally observed at 215 nm and 254 nm with a 4 nm bandwidth. Column: Waters Acquity BEH C18, 1.0 x 50 mm, 1.7 μ m. Gradient conditions: 5% to 95% MeCN in H₂O (0.1% TFA) over 1.4 min, hold at 95% MeCN for 0.1 min, 0.5 mL/min, 55 °C. High resolution mass spectra were obtained on an Agilent 6540 UHD Q-TOF with ESI source. MS parameters were as follows: fragmentor: 150, capillary voltage: 3500 V, nebulizer pressure: 60 psig, drying gas flow: 13 L/min, drying gas temperature: 275 °C. Samples were introduced via an Agilent 1200 UHPLC comprised of a G4220A binary pump, G4226A ALS, G1316C TCC, and G4212A DAD with ULD flow cell. UV absorption was observed at 215 nm and 254 nm with a 4 nm bandwidth. Column: Agilent Zorbax Extend C18, 1.8 μ m, 2.1 x 50 mm. Gradient conditions: 5% to 95% MeCN in H₂O (0.1% formic acid) over 1 min, hold at 95% MeCN for 0.1 min, 0.5 mL/min, 40 °C. For compounds that were purified on a Gilson preparative reversed-phase HPLC, the system comprised of a 333 aqueous pump with solvent-selection valve, 334 organic pump, GX-271 or GX-281 liquid handler, two column switching valves, and a 155 UV detector. UV wavelength for fraction collection was user-defined, with absorbance at 254 nm always monitored. Method 1:

Phenomenex Axia-packed Luna C18, 30 x 50 mm, 5 μ m column. Mobile phase: MeCN in H₂O (0.1% TFA). Gradient conditions: 0.75 min equilibration, followed by user defined gradient (starting organic percentage, ending organic percentage, duration), hold at 95% MeCN in H₂O (0.1% TFA) for 1 min, 50 mL/min, 23 °C. Method 2: Phenomenex Axia-packed Gemini C18, 50 x 250 mm, 10 μ m column. Mobile phase: MeCN in H₂O (0.1% TFA). Gradient conditions: 7 min equilibration, followed by user defined gradient (starting organic percentage, ending organic percentage, duration), hold at 95% MeCN in H₂O (0.1% TFA) for 7 min, 120 mL/min, 23 °C. All reagents were purchased from Aldrich Chemical Co. and were used without purification. All final compounds were >98% pure by LCMS (254 nm, 214 nM and ELSD). Following these purification protocols, final compounds were transferred to a barcode vial and diluted to a concentration of 10 μ M using molecular biology grade dimethylsulfoxide (DMSO). These compounds were registered into Dotmatics and assigned a VU identification (VUID) number before being tested in the primary screening assay.

Molecular Biology and Cell Line Construction

Expression plasmids carrying the complementary DNA (cDNA) sequence of human K_{ir}4.1 or K_{ir}5.1 were purchased from Origene Technologies. To ensure that both channel subunits are expressed in transfected cells, the cDNAs were subcloned into different multiple cloning sites of the bicistronic vector pBudCE4.1 (Invitrogen). The hK_{ir}4.1 cDNA was subcloned downstream of the CMV promoter, whereas the hK_{ir}5.1 cDNA was subcloned downstream of the EF-1 α promoter using gene synthesis

methods by GenScript. The correct cDNA sequences were verified using DNA sequencing.

HEK-293T cells were transfected using Lipofectamine LTX reagent according to the manufacturer's protocol and then placed under antibiotic selection using 700 µg/ml zeocin. Single clones were isolated from stably transfected polyclonal cells using limiting dilution methods, expanded, and then screened for robust $K_{ir}4.1/5.1$ -mediated Tl^{+} flux using the methods described below. Whole-cell patch clamp analysis was used to confirm that HEK-293- $K_{ir}4.1/5.1$ cells exhibited robust outwardly barium-inhibitable, pH-sensitive K^{+} currents that are typical of published $K_{ir}4.1/5.1$ currents. Stably transfected cell lines expressing other Kir channels were generated as described previously (REFS) [OR Stably transfected monoclonal T-Rex-human embryonic kidney 293 (HEK-293) cell lines expressing $K_{ir}1.1$, $K_{ir}2.2$, $K_{ir}2.3$, $K_{ir}4.1$, $K_{ir}4.2$, $K_{ir}6.2/SUR1$, or $K_{ir}7.1-M125R$ from a tetracycline-inducible promoter.

Primary Screening Quantitative Thallium Flux Assay

High-throughput Tl^{+} flux fluorescence-based assay was performed essentially as described before (RFE) using HEK-293- $K_{ir}4.1/5.1$ cells. Briefly, cells were culture overnight in Delbecco's modified Eagle's medium (DMEM) containing 10% FBS at 37°C and 5% CO_2 in 384-well plates. The following day, the cells were incubated with dye-loading assay buffer (Hank's balanced salt solutions, 20 mM HEPES, pH 7.3) containing 0.01% (w/v) Pluronic F-127 (Life Technologies) and 1.2 µM Tl^{+} -reporting dye Thallos Gold or "Pluronic" and Brilliant Tl^{+} (Ion biosciences, Austin, TX) in ambient conditions for 1 h with 20 µL/well assay buffer, washing before and after dye using Hanks' balanced

salt solution/20 mM HEPES (assay buffer). Media and buffer exchange were performed on the ELx405 plate washer (BioTek, Winooski, VT). Dye-loaded cells were then transferred to a Panoptic Kinetic Imaging Plate Reader (Wavefront Bioscience, Franklin, TN) to collect live measurements at 1 Hz (480/40 nm excitation and 540/40 nm emission) during simultaneous 384-well pipetting of 10 μ M small molecules (0.1% dimethylsulfoxide assay buffer) or control (100 μ M fluoxetine). Compounds were incubated for 4 min before the addition of TI⁺ stimulus (125 mM NaHCO₃, 1.8 mM CaSO₄, 1 mM MgSO₄, 5 mM glucose, 1.8 mM TI₂SO₄, and 10 mM HEPES, pH 7.4). Live measurements were collected 10 sec before the addition of compounds to 2 min after TI⁺ stimulus addition.

For identified hits in the primary screen and structure-activity relationship libraries, compounds were tested at concentrations to obtain 11-point, 3-fold dilution concentration-response curves. Data acquisition and analysis were performed using Waveguide (VU-HTS center) and Microsoft Excel. EC₅₀ values were determined by fitting the Hill equation using variable-slope nonlinear regression analyses performed with GraphPad Prism version 5.01 (GraphPad Software, San Diego, CA).

Whole-cell Patch Clamp Electrophysiology

HEK-293T cells were transfected with wild-type (WT) pBudCE4.1-K_{ir}4.1/5.1 or combinations of pcDNA5-K_{ir}4.1 and pcDNA5-K_{ir}5.1 with pcDNA3.1-EGFP (0.5 mg; transfection marker) using Lipofectamine LTX reagent according to the manufacturer's instructions. The cells were dissociated the following day and plated on poly-L-lysine-coated coverslips and allowed to recover for at least 1 h in a 37 °C 5% CO₂/95% air

incubator before beginning experiments. Patch-clamp experiments were performed essentially as described previously. Briefly, patch electrodes (2–3 MV) were filled with an intracellular solution containing 135 mM KCl, 2 mM MgCl₂, 1 mM EGTA, 10 mM HEPES-free acid, and 2 mM Na₂ATP (Roche Diagnostics, Risch-Rotkreuz, Switzerland), pH 7.3, 275 mOsmol/kg water. The standard bath solution contained 135 mM NaCl, 5 mM KCl, 2 mM CaCl₂, 1 mM MgCl₂, 5 mM glucose, and 10 mM HEPES free acid, pH 7.4. Macroscopic currents were recorded under whole-cell voltage-clamp conditions using an Axopatch 200B Amplifier (Molecular Devices, Sunnyvale, CA). Cells were voltage clamped at a holding potential of -75 mV and stepped every 5 sec to -120 mV for 200 milliseconds before ramping to +120 mV at a rate of 1.2 mV/ms. Data were collected at 5 kHz and filtered at 1 kHz. Data acquisition and analysis were performed using the pClamp 9.2 software suite (Molecular Devices). Pharmacology experiments were terminated by applying 2 mM barium (Ba²⁺) chloride to measure leak current. Cells exhibiting < 90% block by Ba²⁺ were excluded from analysis. The mean current amplitude recorded over five successive steps to -120 mV in cells at a single concentration were expressed as the mean ± S.D. Statistical analysis was performed using one-way analysis of variance with Bonferroni multiple-comparisons test with statistical significance defined at P < 0.05. IC₅₀ values were determined by fitting the Hill equation to CRCs using variable-slope nonlinear regression analyses. All the analyses were performed with GraphPad Prism version 5.01 (GraphPad Software).

In Vitro DMPK Methods: Intrinsic Clearance in Rat Liver Microsomes

Rat liver microsomes (0.5 mg/mL) and 1 µM test compound were incubated in 100 mM potassium phosphate pH 7.4 buffer with 3 mM MgCl₂ at 37 °C with constant

shaking. After a 5 min preincubation, the reaction was initiated by addition of NADPH (1 mM). At selected time intervals (0, 3, 7, 15, 25, and 45 min), 50 μ L aliquots were taken and subsequently placed into a 96-well plate containing 150 μ L of cold acetonitrile with internal standard (50 ng/mL carbamazepine). Plates were then centrifuged at 3000 rcf (4 $^{\circ}$ C) for 10 min, and the supernatant was transferred to a separate 96-well plate and diluted 1:1 with water for LC/MS/MS analysis. The *in vitro* half-life ($T_{1/2}$, min, Eq. 1), intrinsic clearance (CL_{INT} , mL/min/kg, Eq. 2) and subsequent predicted hepatic clearance (CL_{HEP} , mL/min/kg, Eq. 3) were determined employing the following equations:

$$(1) \quad T_{1/2} = \frac{\ln(2)}{k}$$

where k represents the slope from linear regression analysis of the natural log percent remaining of test compound as a function of incubation time

$$(2) \quad CL_{int} = \frac{0.693}{in\ vitro\ T_{1/2}} \times \frac{mL\ incubation}{mg\ microsomes} \times \frac{45\ mg\ microsomes}{grams\ liver} \times \frac{45^a\ gram\ liver}{kg\ body\ weight}$$

^ascale-up factor that is species specific

$$(3) \quad CL_{hep} = \frac{Q_h \cdot CL_{int}}{Q_h + CL_{int}}$$

Where Q_h (hepatic blood flow) is species specific

Rat Plasma Protein Binding

The protein binding of each compound was determined in rat or mouse plasma via equilibrium dialysis employing HTDialysis Teflon dialysis chamber and cellulose membranes (MWCO 12-14 K) (HTDialysis LLC, Gales Ferry, CT). Plasma was added to

the 96-well plate containing test compound and mixed thoroughly for a final concentration of 5 μ M. Subsequently, 150 μ L of the plasma-compound mixture was transferred to the dialysis chamber, with an accompanying 150 μ L of phosphate buffer (25 mM, pH 7.4) on the other side of the membrane. The device plate was sealed and incubated for 4 h at 37 $^{\circ}$ C with shaking. At completion, aliquots from each chamber were diluted 1:1 with either plasma (for the buffer sample) or buffer (for the plasma sample) and transferred to a new 96-well plate, at which time ice-cold acetonitrile containing internal standard (50 ng/mL carbamazepine) (2 volumes) was added to extract the matrices. The plate was centrifuged (3000 rcf, 10 min) and supernatants transferred and diluted 1:1 (supernatant: water) into a new 96 well plate, which was then sealed in preparation for LC/MS/MS analysis. Each compound was assayed in triplicate within the same 96-well plate. Fraction unbound was determined using the following equation:

$$F_u = \frac{Conc_{buffer}}{Conc_{plasma}}$$

Rat Brain Homogenate Binding

The brain homogenate binding of each compound was determined in brain homogenate via equilibrium dialysis employing HTDialysis Teflon dialysis chamber and cellulose membranes (MWCO 12-14 K) (HTDialysis LLC, Gales Ferry, CT). Brain tissue homogenate was prepared by diluting one volume whole mouse or rat brain tissue with one to three volumes (species specific) of phosphate buffer (25 mM, pH 7.4). The mixture was then subjected to mechanical homogenization employing a MiniBeadbeater™ and 1.0 mm Zirconia/Silica Beads (BioSpec Products). Brain

homogenate spiked with test compound and mixed thoroughly for a final concentration of 5 μ M. Subsequently, 150 μ L of the brain homogenate-compound mixture was transferred to the dialysis chamber with an accompanying 150 μ L of phosphate buffer (25 mM, pH 7.4) on the other side of the membrane. The block was sealed and incubated for 6 h at 37 °C with shaking. At completion, aliquots from each side of the chamber were diluted 1:1 with either brain homogenate (to the buffer side) or buffer (to the brain homogenate side) in a new 96 well plate, at which time ice-cold acetonitrile containing internal standard (50 ng/mL carbamazepine) was added to extract the matrices. The plate was centrifuged (3000 rcf, 10 min) and supernatants transferred and diluted 1:1 (supernatant: water) into a new 96 well plate, which was then sealed in preparation for LC/MS/MS analysis. Each compound was assayed in triplicate within the same 96-well plate. Fraction unbound was determined using the following equation:

$$F_{u,tissue} = \frac{1/D_f}{\left(\frac{1}{F_{u,hom}} - 1\right) + 1/D_f}$$

Where $F_{u,hom}$ represent the measured fraction unbound in the diluted homogenate and D_f represents dilution factor.

LC/MS/MS Analysis of Samples from In Vitro Assays

Samples were analyzed via electrospray ionization (ESI) on an AB Sciex API4000 (Foster City, CA) triple-quadrupole instrument that was coupled with Shimadzu LC-10AD pumps (Columbia, MD) and a Leap Technologies CTC PAL auto-sampler (Carrboro, NC). Analytes were separated by gradient elution using a Fortis C18 3.0 x 50 mm, 3 μ m column (Fortis Technologies Ltd, Cheshire, UK) thermostated at 40 °C.

HPLC mobile phase A was 0.1% formic acid in water (pH unadjusted), mobile phase B was 0.1% formic acid in acetonitrile (pH unadjusted). The gradient started at 10% B after a 0.2 min hold and was linearly increased to 90% B over 1.2 min; held at 90% B for 0.1 min and returned to 10% B in 0.1 min followed by a re-equilibration (0.9 min). The total run time was 2.5 min and the HPLC flow rate was 0.5 mL/min. The source temperature was set at 500 °C and mass spectral analyses were performed using multiple reaction monitoring (MRM), with transitions specific for each compound utilizing a Turbo-Ionspray® source in positive ionization mode (5.0 kV spray voltage).

In Vivo PK Methods

All rodent PK experiments were conducted in accordance with the National Institute of Health regulations of animal care covered in Principles of Laboratory Animal Care (National Institutes of Health publication 85-23, revised 1985) and were approved by the Institutional Animal Care and Use Committee.

Single Time Point Tissue Distribution Studies

IV cassette PK experiments in rats were carried out according to methods described previously. Briefly, a cassette of compounds (n = 4–5/cassette) were formulated from 10 mM solutions of compounds in DMSO. In order to reduce the absolute volume of DMSO that was administered, the compounds were combined and diluted with ethanol and PEG 400 to achieve a final concentration of 0.4–0.5 mg/mL for each compound (2 mg/mL total) administered in each cassette. The final dosing solutions consisted of approximately 10% ethanol, 40% PEG400, and 50% DMSO (v/v). For time course PK studies, each cassette dose was administered IV via the jugular

vein to two dual-cannulated (carotid artery and jugular vein) adult male Sprague–Dawley rats, each weighing between 250 and 350 g (Harlan, Indianapolis, IN) for a final dose of 0.2–0.25 mg/kg per compound. Whole blood collections via the carotid artery were performed at 0.033, 0.117, 0.25, 0.5, 1, 2, 4, 7, and 24 h post dose and plasma samples prepared for bioanalysis. For single time point tissue distribution studies, compounds were formulated as described above (in cassette format) and dosed to male Sprague-Dawley rats for a final dose of 0.2-0.25 mg/kg per compound. Brain dissection and blood collections via the carotid artery were performed 0.25 hr post dose. The brain samples were rinsed in PBS, snap frozen and stored at -80 °C. Prior to LC/MS/MS analysis, brain samples were thawed to room temperature and subjected to mechanical homogenation employing a Mini-Beadbeater™ and 1.0 mm Zirconia/Silica Beads (BioSpec Products).

LC/MS/MS Bioanalysis of Samples from In Vivo Assays

In vivo samples were analyzed via electrospray ionization (ESI) on an AB Sciex API-4000 (Foster City, CA) triple-quadrupole instrument that was coupled with Shimadzu LC-10AD pumps (Columbia, MD) and a Leap Technologies CTC PAL autosampler (Carrboro, NC). Analytes were separated by gradient elution using a Fortis C18 3.0 x 50 mm, 3 µm column (Fortis Technologies Ltd, Cheshire, UK) thermostated at 40 °C. HPLC mobile phase A was 0.1% formic acid in water (pH unadjusted), mobile phase B was 0.1% formic acid in acetonitrile (pH unadjusted). The source temperature was set at 500 °C and mass spectral analyses were performed using multiple reaction monitoring (MRM), with transitions specific for each compound utilizing a Turbolonspray® source in positive ionization mode (5.0 kV spray voltage). The

calibration curves were constructed, and linear response was obtained by spiking known amounts of test compound in blank brain homogenate or plasma. All data were analyzed using AB Sciex Analyst software v1.5.1. The final PK parameters were calculated by noncompartmental analysis using Phoenix (version 6.2) (Pharsight Inc., Mountain View, CA).

Development of an Improved *In Vitro* Tool Compound, VU0493690, For Inhibition of the Heterotetrameric Kir4.1/5.1 Receptor

Medicinal Chemistry Strategy for the Exploration of VU0493690 (1.4)

VU0493690 (1.4) was an attractive start for our medicinal chemistry campaign due to its selectivity for Kir4.1/5.1 over other Kir channels, including the hERG channel. With the lack of a crystal structure and homology model, we hypothesized that through methodical derivatization of the molecule, we could drive down potency. The initial optimization plan for 1.4 is depicted in **Figure 1.3**, and generated analogs were screened the TI⁺-flux assay developed by the Denton lab to determine SAR. Iterative, parallel syntheses were employed to diversify three regions of the molecule.

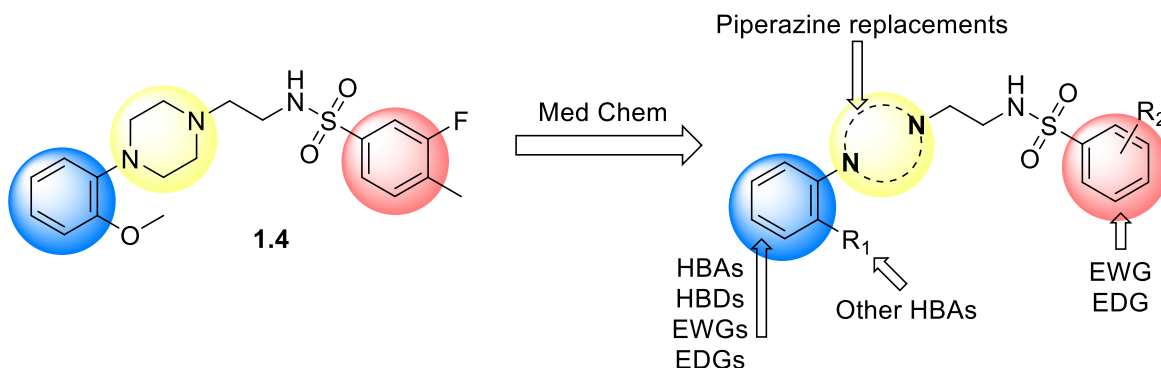
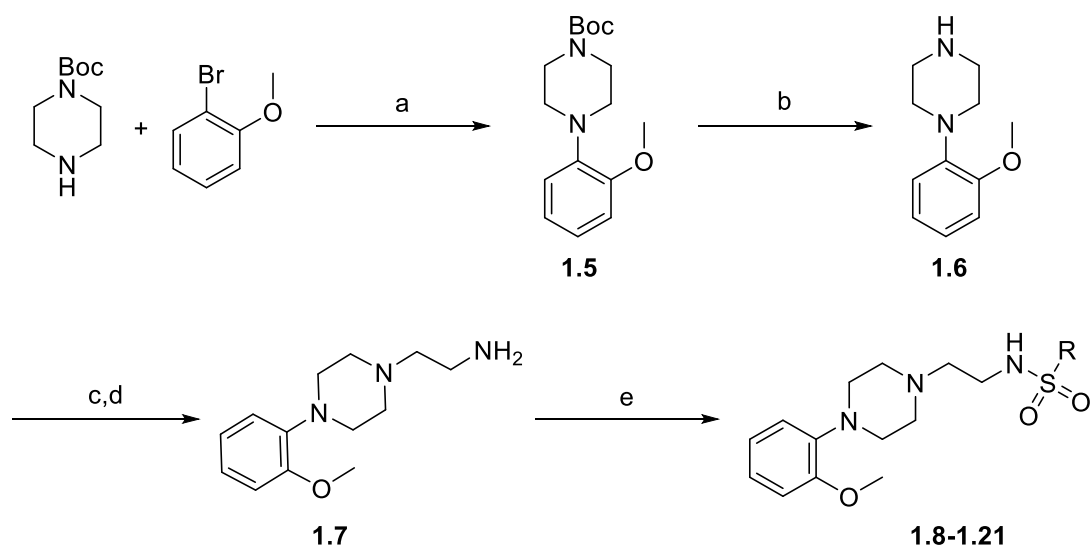


Figure 1.3: Medicinal chemistry strategy for the exploration of VU0493690

Modification of the Eastern Aryl Sulfonamide: Analogs **1.8-1.21**

Initial SAR efforts began with the eastern aryl sulfonamide moiety of **1.4** in an effort to define its role in binding $K_{i4.1/5.1}$. The arene ring lacks an obvious HBD or HBA and suggests that it contributes to binding via a pi-stacking interaction or by occupying a lipophilic pocket. A compound set was designed using electron withdrawing and electron donating groups with different aromatic substitution patterns that would create small perturbations capable of elucidating a pi-stacking relationship. Additionally, other aromatic heterocyclic ring systems were included within this SAR library under the assertion that they would be inactive should there be a lipophilic binding pocket within the binding site.



Scheme 1.1: (a) Pd₂(dba)₃, XPhos, Na₂CO₃, toluene, 100 °C, 30 min, microwave irradiation, 36% (b) 4N HCl in dioxanes, 0 °C to rt, 30 min, quantitative yield (c) *tert*-butyl (2-oxoethyl)carbamate, NaBH₃CN, AcOH, MeOH, rt, 12 h, 78% (d) 4N HCl in dioxanes, 0 °C to rt, 30 min, quantitative yield (e) RSO₂Cl, DIPEA, DCM, 0 °C to rt, 8 h, 56-87%.

Analogs of this nature were rapidly synthesized from readily available starting materials in a five-step sequence outlined in **Scheme 1.1** that prioritized late-stage diversification. Commercial building blocks 1-Boc-piperazine and 1-bromo-2-methoxybenzene were coupled together using Buchwald-Hartwig conditions to access **1.5** in low but acceptable yields. Acid-catalyzed deprotection of **1.5** gave the desired *N*-arylpiperazine, **1.6**, in quantitative yields. Reductive amination conditions were then utilized to couple **1.6** with a Boc-protected 2-aminoacetaldehyde, followed by a Boc-deprotection using acidic conditions to yield **1.7** in excellent yields. The resulting primary amine was carried forward crude as the hydrochloride salt, then coupled with commercially available sulfonyl chlorides to yield final compounds **1.8-1.21**. **Table 1.1** details the activities of this compound library.

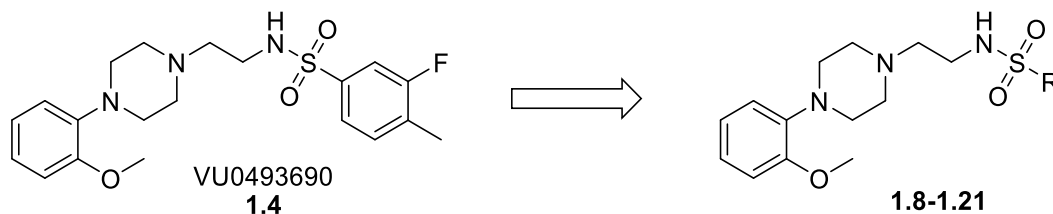
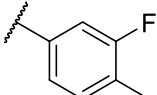
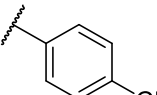
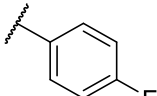
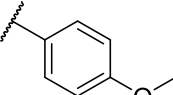
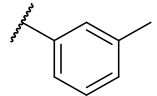
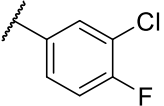
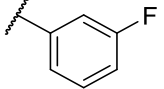
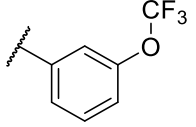
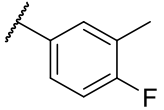
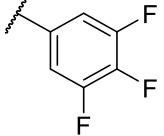
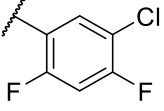
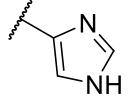
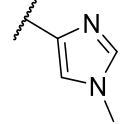
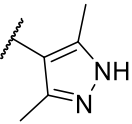
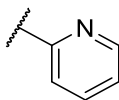


Table 1.1: Structures of aryl sulfonamide analogs of VU0493690 (**1.4**) for the initial analysis of potency. Associated potency and efficacy data from 11-point, 3-fold dilution, CRC-format screen at HEK-293-K_{ir}4.1/5.1 cells. TI⁺ flux responses for each compound are reported as an IC₅₀ value, determined by fitting the Hill equation to CRCs using variable-slope nonlinear regression analyses. Values listed as NF indicate no line fit. VUID denotes the compound identifier assigned by Vanderbilt University. Data represent the mean of at least 3 replicate experiments with similar results.

R	VUID	Compound Number	K _{ir} 4.1/5.1 IC ₅₀ (μM)
	VU0493690	1.4	4.83
	VU6032282	1.8	7.91
	VU6032283	1.9	16.9
	VU6032285	1.10	4.26
	VU6032286	1.11	4.28

	VU0909814	1.12	3.56
	VU6032284	1.13	9.33
	VU0909816	1.14	7.36
	VU0909815	1.15	11.2
	VU6036357	1.16	4.7
	VU6036364	1.17	NF
	VU6032288	1.18	NF
	VU0909813	1.19	NF
	VU6032289	1.20	NF



VU0522348

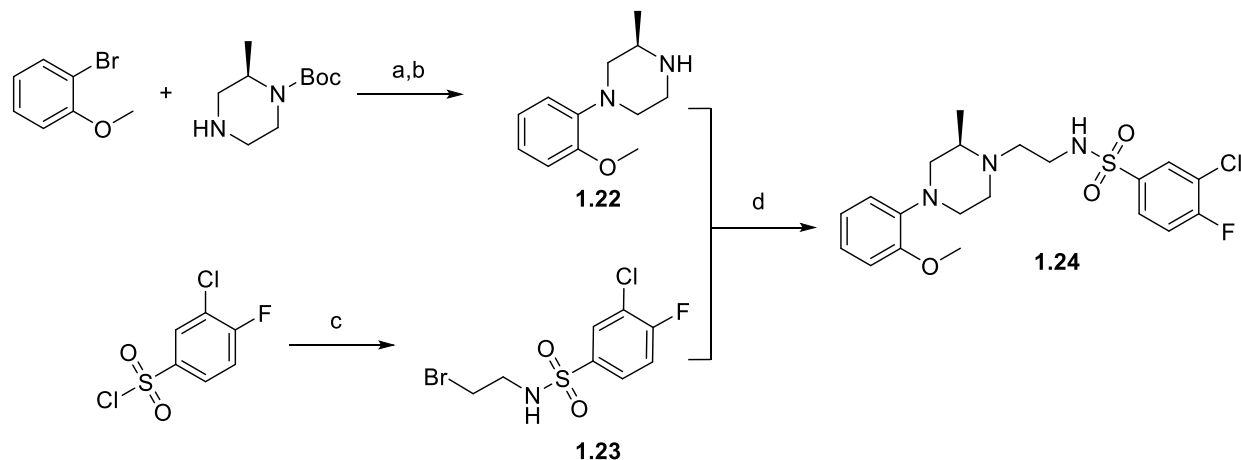
1.21

NF

The introduction of apparent electron withdrawing groups to the 3- or 4-position of the arene ring (**1.8**, **1.9**, **1.13**, **1.14**) resulted in a loss of potency, while more donating groups (**1.10**, **1.11**) maintained the activity of **1.4**. Various 5- and 6-membered heterocycles (analogs **1.18-1.21**) were completely inactive. The only improvement in potency was with di-halide **1.12**, with a reported IC₅₀ of 3.56 μM in the TI⁺-flux assay. From the SAR, it is impossible to deduce if the modest improvement seen with **1.4** was a result of further engaging in a pi-stacking relationship, or by maintaining the lipophilicity. Regardless, **1.12** was carried forward for further derivatization.

Exploration of the Central Piperazine Core: Analogs 1.24-1.29

With the optimized eastern aryl sulfonamide of **1.12**, a series of compounds with piperazine bioisosteres and derivatives were designed to elucidate the role of the central piperazine core in binding (**Table 1.2**). Piperazines and their derivatives are a commonly encountered motif in medicinal chemistry. While they may be responsible for engaging in meaningful interactions with their target protein, they are most often an important group in modulating favorable physicochemical properties.³³ Thus, we sought to explore if this chemical space could be better occupied to improve activity at Kir4.1/5.1.



Scheme 1.2: (a) $\text{Pd}_2(\text{dba})_3$, XPhos, Na_2CO_3 , toluene, $100\text{ }^\circ\text{C}$, 30 min, microwave irradiation, (b) 4N HCl in dioxanes, $0\text{ }^\circ\text{C}$ to rt, 30 min, (c) 2-bromoethan-1-amine hydrobromide, DIPEA, DCM, $0\text{ }^\circ\text{C}$ to rt, 8 h, (d) K_2CO_3 , NaI, DCM, $80\text{ }^\circ\text{C}$, 8 h.

These compounds were obtained by following the synthetic route outlined in **Scheme 1.2** which produced the desired library quickly and in acceptable yields. Commercial building blocks 1-bromo-2-methoxybenzene and the desired *N*-Boc protected piperazine were coupled together using Buchwald-Hartwig conditions followed by an acid-catalyzed deprotection gave the desired *N*-aryl piperazine, **1.22**, in low yields. **1.22** was carried forward as the hydrochloride salt and subjected to $\text{S}_{\text{N}}2$ coupling conditions with alkyl bromide **1.23**, to yield compounds **1.24-1.29**. The results of this SAR campaign are summarized in Table **1.2**.

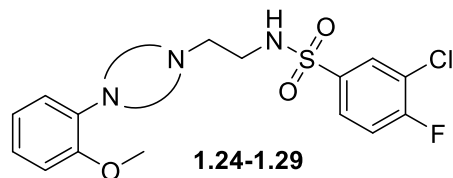
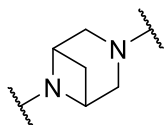


Table 1.2: Structures of piperazine-replacement analogs of **1.12** for the initial analysis of potency. Associated potency and efficacy data from 11-point, 3-fold dilution, CRC-format screen at HEK-293-K_{ir}4.1/5.1 cells. TI⁺ flux responses for each compound are reported as an IC₅₀ value, determined by fitting the Hill equation to CRCs using variable-slope nonlinear regression analyses. Values listed as NF indicate no line fit. VUID denotes the compound identifier assigned by Vanderbilt University. Data represent the mean of at least 3 replicate experiments with similar results.

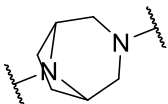
R	VUID	Compound Number	K _{ir} 4.1/5.1 IC ₅₀ (μM)
	VU6035884	1.24	17.3
	VU6035886	1.25	NF
	VU6035892	1.26	8.92
	VU6035894	1.27	5.00



VU6035885

1.28

>100



VU6035889

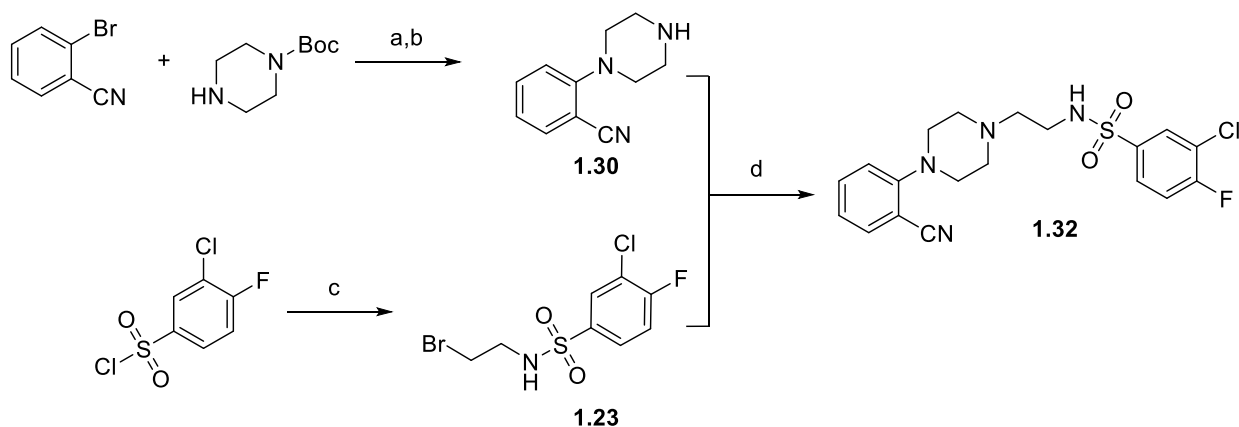
1.29

NF

No enhancements to potency were achieved with this set of compounds.

Spirocycle **1.24**, fused bicycle **1.25**, and bridged (**1.28**, **1.29**) analogues were weakly or totally inactive. Both enantiomers of 2-methylpiperazine were tolerated, with preference for the (*R*) enantiomer **1.27**, but were not an improvement upon **1.12**.

Modification of the Western Aryl Ring: Analogs **1.31-1.51**



Scheme 1.3: (a) $\text{Pd}_2(\text{dba})_3$, XPhos, Na_2CO_3 , toluene, 100 °C, 30 min, microwave irradiation, (b) 4N HCl in dioxanes, 0 °C to rt, 30 min, (c) 2-bromoethan-1-amine hydrobromide, DIPEA, DCM, 0 °C to rt, 8 h, (d) K_2CO_3 , NaI, DCM, 80 °C, 8 h.

Similar to **Scheme 1.2**, the desired compound library was produced quickly and in acceptable yields following the route outlines in **Scheme 1.3**. Commercial building blocks 1-boc-piperazine and the desired aryl halide were coupled together using

Buchwald-Hartwig conditions, followed by an acid-catalyzed deprotection which gave the desired *N*-arylpiperazine, **1.30**, in low but workable yields. **1.30** was carried forward as the hydrochloride salt and subjected to S_N2 coupling conditions with alkylbromide **1.23** to produce compounds **1.31-1.43**.

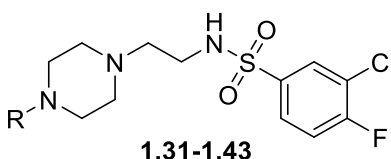
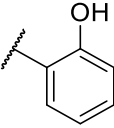
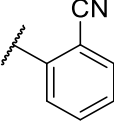
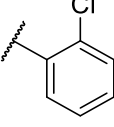
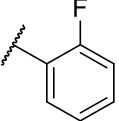
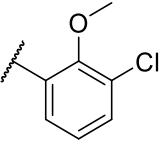
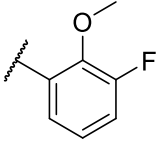
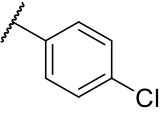
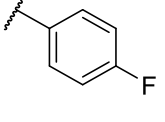
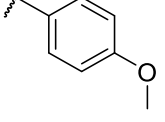
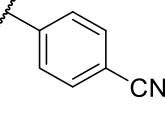
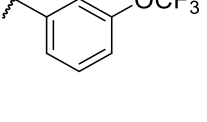
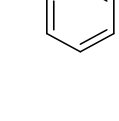
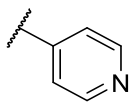


Table 1.3: Analogs **1.31-1.43** for the initial analysis of potency. Associated potency and efficacy data from 11-point, 3-fold dilution, CRC-format screen at HEK-293-K_{ir}4.1/5.1 cells. Tl⁺ flux responses for each compound are reported as an IC₅₀ value, determined by fitting the Hill equation to CRCs using variable-slope nonlinear regression analyses. Values listed as NF indicate no line fit. VUID denotes the compound identifier assigned by Vanderbilt University. Data represent the mean of at least 3 replicate experiments with similar results.

R	VUID	Compound Number	K _{ir} 4.1/5.1 IC ₅₀ (μM)
	VU6035860	1.31	NF
	VU6035866	1.32	2.63
	VU6035867	1.33	11.9

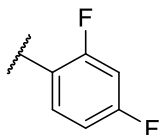
	VU6032285	1.34	4.26
	VU6035897	1.35	NF
	VU6036365	1.36	NF
	VU6035862	1.37	NF
	VU6035864	1.38	22.2
	VU6035863	1.39	48.8
	VU6035895	1.40	NF
	VU6035896	1.41	16.2
	VU6036356	1.42	12.6



VU6035899

1.43

NF



VU6035865

1.44

9.43

Replacement of the 2-methoxy proved to be detrimental for activity, except for compound **1.32**, in which the 2-nitrile showed an improved IC_{50} of 2.63 μ M in the Tl^{+} -flux assay, a 2-fold improvement over **1.4**. Substitution at the 3- and 4-position of the arene ring reduced potency by 3-fold or more as seen with analogues **1.31-1.41**. Additionally, pyridinyl analogues (**1.42**, **1.43**) were inactive. It was then hypothesized that both the 2-methoxy and 2-nitrile of **1.4** and **1.32**, respectively, were acting as hydrogen bonding acceptors. We then conducted methyl and halide walks around the arene ring while maintaining the 2-nitrile in an attempt to further strengthen this interaction. Unfortunately, compounds **1.45-1.51** were weakly active or completely inactive and are shown below in Table **1.4**. Thus, we carried forward with **1.32** as our lead compound.

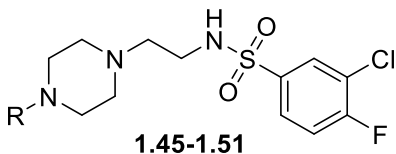
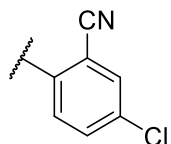


Table 1.4: Structures of analogs of **1.32** for the initial analysis of potency. Associated potency and efficacy data from 11-point, 3-fold dilution, CRC-format screen at HEK-293-K_{ir}4.1/5.1 cells. TI⁺ flux responses for each compound are reported as an IC₅₀ value, determined by fitting the Hill equation to CRCs using variable-slope nonlinear regression analyses. Values listed as NF indicate no line fit. VUID denotes the compound identifier assigned by Vanderbilt University. Data represent the mean of at least 3 replicate experiments with similar results.

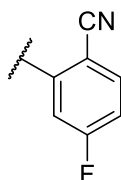
R	VUID	Compound Number	K _{ir} 4.1/5.1 IC ₅₀ (μM)
	VU6036730	1.45	NF
	VU6036729	1.46	7.79
	VU6036731	1.47	14.4
	VU6035899	1.48	NF
	VU6036758	1.49	6.81



VU6036726

1.50

12.5



VU0522348

1.51

NF

*Re-investigation of the Central Piperazine: Analogs **1.52-1.57***

With the significant improvement seen with **1.32**, we moved to re-investigate the role of the piperazine core in binding $K_{i4.1/5.1}$. Following the same synthetic route outlined **Scheme 1.2**, compounds **1.52-1.57** were synthesized rapidly and screened for inhibitory activity against $K_{i4.1/5.1}$. Similar to previous attempts, spirocycle **1.52** and fused bicycle **1.53**, were weakly or completely inactive. Enantiopure 2- and 3-methyl piperazine analogues **1.54-1.57** provided important insight to the observed SAR trends.

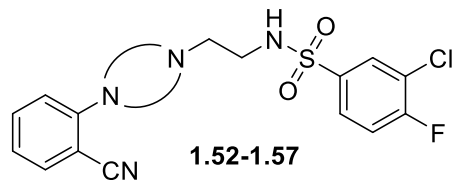
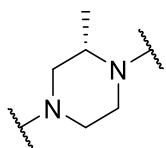


Table 1.5: Structures of piperazine bioisostere analogs of **1.32** for the initial analysis of potency. Associated potency and efficacy data from 11-point, 3-fold dilution, CRC-format screen at HEK-293-K_{ir}4.1/5.1 cells. TI⁺ flux responses for each compound are reported as an IC₅₀ value, determined by fitting the Hill equation to CRCs using variable-slope nonlinear regression analyses. VUID denotes the compound identifier assigned by Vanderbilt University. Values listed as NF indicate no line fit. Data represent the mean of at least 3 replicate experiments with similar results.

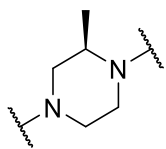
R	VUID	Compound Number	K _{ir} 4.1/5.1 IC ₅₀ (μM)
	VU6036759	1.52	NF
	VU6036757	1.53	10.6
	VU6036721	1.54	NF
	VU6036720	1.55	0.735



VU6036724

1.56

6.09



VU6036722

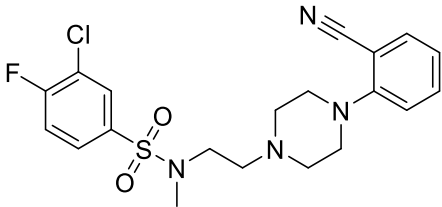
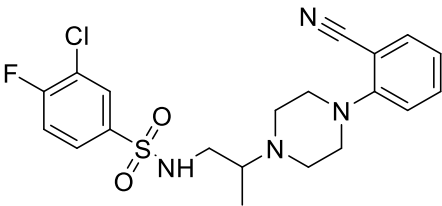
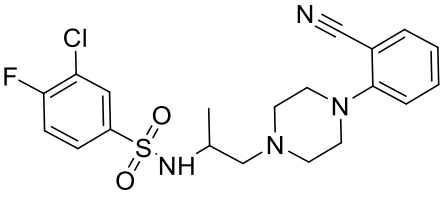
1.57

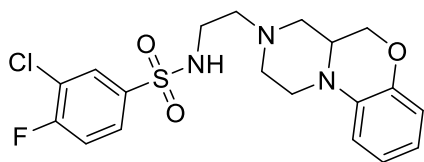
NF

As seen in Table 1.5, the 2-(*R*)-methylpiperazine analog, **1.55**, resulted in a 3.5-fold improvement over **1.32**, while the other 2- and 3-methyl piperazine analogues **1.54**, **1.56**, and **1.57** were devoid of activity. We attempted to rationalize the observed consequences of introducing axial or equatorial methyl groups at the 2- and 3- position of the piperazine core, illustrated in **Figure 1.4**. With compounds **1.56** and **1.57**, we hypothesized that an axial or equatorial methyl group at the 3-position introduced steric clash and reoriented the eastern aromatic ring within the binding pocket. Such conformational constrain might prevent the 2-benzonitrile from engaging in its proposed hydrogen-bonding interaction, and result in the observed loss of potency. In contrast, an axial methyl at the 2-position of the piperazine core (**1.55**) was advantageous. It was then hypothesized, that this introduction of strain forces the molecule to exist predominantly in its bioactive conformation. Reducing the conformational flexibility of the ligand would decrease to entropic cost of ligand binding and result in increased potency, as observed with **1.55**.³⁴ Thus, we moved to design additional derivatives of **1.32** and **1.4** with conformational constrain to further explore our hypothesis.

Exploration Conformational Constrains: Analogs **1.58-1.61**

A set of four compounds were designed with the intent of introducing conformational constrain. These compounds and their activities are shown in Table **1.6**. Analogs **1.59-1.61** were attempts to reduce the flexibility of the ethylene linker of **1.32**. Interestingly, *N*-methylation of the sulfonamide resulted in a four-fold loss of potency as seen with **1.59**. It is difficult to discern if this loss of activity is due to rigidification, or if the sulfonamide acts as a hydrogen bond donor. While racemic **1.60** and **1.61** were not as potent as **1.55**, they maintained potency and enantiopure derivatives may be as or more potent than that of the lead, **1.32**.

Structure	VOID	Cpd Num	K _{ir} 4.1/5.1 IC ₅₀ (μM)
	VU6036734	1.59	11.1
	VU6036735	1.60	1.3
	VU6036736	1.61	4.2

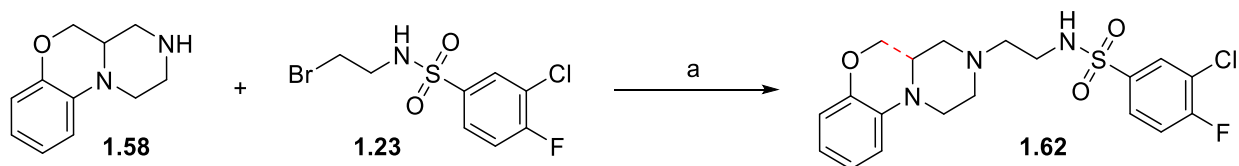


VU6036352

1.62

7.90

Table 1.6: Conformationally constrained analogs of **1.32** and **1.4** for the initial analysis of potency. Associated potency and efficacy data from 11-point, 3-fold dilution, CRC-format screen at HEK-293-K_{ir}4.1/5.1 cells. TI⁺ flux responses for each compound are reported as an IC₅₀ value, determined by fitting the Hill equation to CRCs using variable-slope nonlinear regression analyses. Values listed as NF indicate no line fit. VUID denotes the compound identifier assigned by Vanderbilt University. Data represent the mean of at least 3 replicate experiments with similar results.



Scheme 1.4: (a) K₂CO₃, NaI, DCM, 80 °C, 8 h.

Compound **1.62** was envisioned to be a tied-back version of **1.12**, which would lock the eastern arene ring into place. It was hypothesized that removing the flexibility associated with the methyl ether might allow it to better engage in its hydrogen bonding interaction. Jacob Kalbfleisch kindly donated tricyclic **1.58** from the mGlu₇ campaign, to access **1.62** (Scheme 1.4). Unfortunately, **1.62** was 2-fold less active than **1.12**.

Assessment of VU6036720 as a Viable Tool Compound

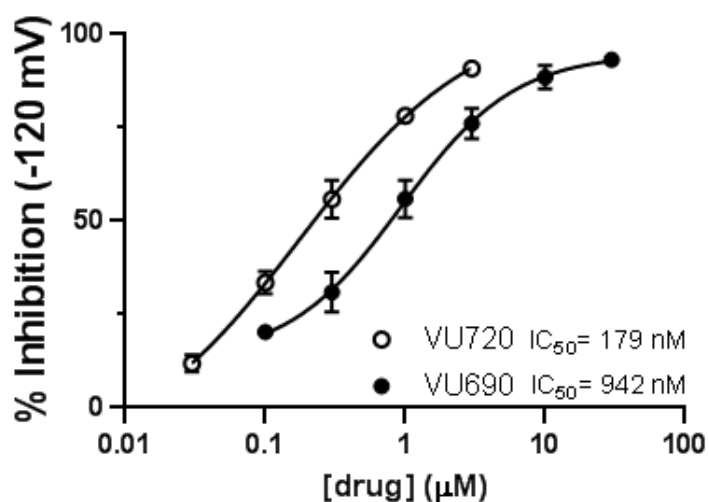


Figure 1.4: Manual patch clamp studies illustrating the improvement of VU690 (**1.4**) with VU720 (**1.55**).

The activity of **1.55** was confirmed in manual patch clamp experiments, in which it inhibited $K_{ir4.1/5.1}$ currents at -120 mV with an IC_{50} of 179 nM. This is a significant improvement in activity over the original hit compound **1.4** (**Figure 1.5**). Compound **1.55** also appears to be 'drug-like,' considering its low molecular weight (MW <500), acceptable cLogP, and a total polar surface area similar to that of CNS drugs on the market (cLogP of 3.4, tPSA of 75, **Table 1.7**).³⁵ Due to the potential utility of a selective $K_{ir4.1/5.1}$ inhibitor, lead compound **1.55** was tested for its DMPK properties to determine if this scaffold could potentially serve as an *in vivo* tool compound.

Property	1.55
MW	436.9
cLogP	3.4
tPSA	76.4
<i>Pharmacokinetic parameters</i>	
CL _{INT} (mL/min/kg), rat	5984
CL _{HEP} (mL/min/kg), rat	69.2
CL _{HEP (f_u)p} (mL/min/kg), rat	25.1
CL _{INT} (mL/min/kg), human	344
CL _{HEP} (mL/min/kg), human	19.8
PPB (f _u), rat	0.009
PPB (f _u), human	0.008
BHB (f _u), rat	0.007
<i>Tissue distribution</i>	
C _n plasma (ng/mL)	17.1
C _n brain (ng/mL)	49.1
K _p , brain	2.87
K _{p,uu} brain	2.23

Table 1.7: *In vitro* and *in vivo* DMPK profiles of **1.55**.

Unfortunately, **1.55** suffers from high hepatic clearance with a CL_{HEP} of 69.2 mL/min/kg in rats. The free unbound fraction of **1.55** is also unattractive with <1% free fraction; however, this provides a more acceptable CL_{HEP (f_u)p} of 25.1 (mL/min/kg) when corrected for the unbound fraction. When considering fraction unbound data with the plasma/brain ratio (K_p), the unbound partition coefficient (K_{p,uu}) is 2.23; indicating influx of **1.55** at the blood-brain barrier (BBB). While there is significant room for improvement,

1.55 could be considered for *in vivo* studies considering its novel action, potency, brain penetrance, and the selectivity of the scaffold.

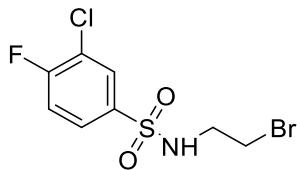
Summary and Future Directions

To summarize, an SAR campaign was conducted with VU0493690 (**1.4**) where we efficiently improved inhibitory activity at $K_{ir4.1/5.1}$ greater than 5-fold in both fluorescence and electrophysiology-based assays. The lead compound, **1.55**, stands as the first inhibitor of the $K_{ir4.1/5.1}$ heterotetrameric channel. Unfortunately, DMPK studies concluded that **1.55** is highly cleared, a major liability with this scaffold. However, considering the novel action of the scaffold, **1.55** could be co-administered with 1-aminobenzotriazole (ABT) to inhibit CYP metabolism in animal models to get initial, proof of concept studies. At first glance, it is tempting to associate the observed hepatic clearance due to the metabolically labile sulfonamide in **1.55**. It is also possible that the western aryl ring undergoes a CYP-mediated oxidation. Medicinal chemistry efforts are needed to address these issues. Further, while the selectivity for $K_{ir4.1/5.1}$ over other K_{ir} channels and the hERG channel has been confirmed for this scaffold with **1.4**, **1.55** should be subjected to the same scrutiny. Fortunately, compound **1.55** is brain penetrant with a $K_{p,uu}$ of 2.23, and *in vivo* studies are underway with **1.55** to explore the integrative physiology and therapeutic potential of $K_{ir4.1/5.1}$ channels in diseases associated with channel dysfunction.

Experimental Methods

General Synthetic Methods and Instrumentation

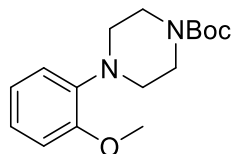
Unless otherwise stated, all reactions were conducted in flame-dried or oven-dried glassware under inert atmospheres of argon. All commercially available reagents and reaction solvents were used as received, unless otherwise noted. Thin layer chromatography (TLC) was performed on glass-backed silica of 250 μm thickness. Visualization was accomplished with UV light and/or the use of bromocresol green stain. Chromatography on silica gel was performed using Teledyne ISCO pre-packed silica gel columns using gradients of EtOAc/hexanes. ^1H and ^{13}C chemical shifts are reported in δ values in ppm downfield with the deuterated solvent as the internal standard. Data are reported as follows: chemical shift, multiplicity (s = singlet, d = doublet, t = triplet, q = quartet, b = broad, m = multiplet), integration, coupling constant (Hz). Low resolution mass spectra were obtained on an Agilent 6120 or 6150 with ESI source. MS parameters were as follows: fragmentor: 70, capillary voltage: 3000 V, nebulizer pressure: 30 psig, drying gas flow: 13 L/min, drying gas temperature: 350 $^{\circ}\text{C}$. Samples were introduced via an Agilent 1290 UHPLC comprised of a G4220A binary pump, G4226A ALS, G1316C TCC, and G4212A DAD with ULD flow cell. UV absorption was generally observed at 215 nm and 254 nm with a 4 nm bandwidth. Column: Waters Acquity BEH C18, 1.0 x 50 mm, 1.7 μm . Gradient conditions: 5% to 95% MECN in H₂O (0.1% TFA) over 1.4 min, hold at 95% MECN for 0.1 min, 0.5 mL/min, 55 $^{\circ}\text{C}$. All reagents were purchased from Aldrich Chemical Co. and were used without purification. Sure-Seal solvents were purchased from Sigma Aldrich.



***N*-(2-bromoethyl)-3-chloro-4-fluorobenzenesulfonamide (1.23)**: A mixture of 2-bromoethan-1-amine hydrobromide (2.5 mmol), triethylamine (3.0 mmol), DMAP (0.25 mmol) and 3-chloro-4-fluorobenzenesulfonyl chloride (2.75 mmol) was stirred in DCM for 16 h at rt. The crude product was purified by column chromatography (10 – 40% EtOAc/hexanes) to provide the title compound as a white solid (125 mg, 63%). **¹H NMR (400 MHz, CDCl₃)** δ 7.90 (dd, *J* = 6.7, 2.3 Hz, 1H), 7.72 (ddd, *J* = 8.7, 4.3, 2.3 Hz, 1H), 7.26 – 7.15 (m, 1H), 3.35 (q, *J* = 4.4, 3.9 Hz, 4H). **¹³C NMR (101 MHz, CDCl₃)** δ 160.66 (d, *J*_{CF} = 257.7 Hz), 136.94 (d, *J*_{CF} = 4.1 Hz), 127.42 (d, *J*_{CF} = 8.5 Hz), 122.53 (d, *J*_{CF} = 18.8 Hz), 117.51 (d, *J*_{CF} = 22.4 Hz), 44.51, 31.33. **LC-MS [m/z+H]** = 315.8.

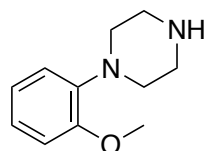
General Synthesis of *N*-aryl Piperazines: In oven dried Biotage microwave vial, arylhalide (1.1 equiv.), *N*-Boc-protected piperazine (1 equiv.), Pd₂(dba)₃ (0.1 equiv.), XPhos (0.25 equiv.), (CH₃)₃CONa (4 equiv.), were dissolved in toluene (0.2 M) under an atmosphere of argon. The reaction was subjected to 30 min of microwave irradiation at 120 °C. The reaction was then diluted with DCM and washed with sat. NH₄Cl. The organic layer was washed with sat. NaHCO₃ and brine, dried over Na₂SO₄, filtered, and concentrated. The crude product was purified by column chromatography (EtOAc/hexanes gradient) to provide the pure Boc-protected *N*-aryl Piperazine. The Boc-protected amine was taken up in a commercially available 4N HCl in Dioxanes solution at rt and stirred for 2 h. The reaction mixture was concentrated under reduced

pressure and triturated with diethyl ether to yield the desired *N*-aryl piperazine as the hydrochloride salt.



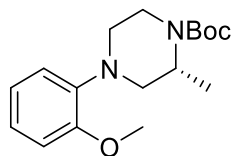
Synthesis of *tert*-butyl 4-(2-methoxyphenyl)piperazine-1-carboxylate (1.5).

Following the general procedure, crude **1.5** was purified by column chromatography (10 – 40% EtOAc/hexanes) to provide the title compound as a clear oil (125 mg, 43%). **¹H NMR (400 MHz, CDCl₃)** δ 7.05 (t, J = 8.5 Hz, 1H), 6.98 – 6.87 (m, 3H), 3.89 (s, 3H), 3.64 (t, J = 5.1 Hz, 4H), 3.04 (d, J = 5.7 Hz, 4H), 1.50 (s, 9H). **¹³C NMR (101 MHz, CDCl₃)** δ 154.83, 152.27, 121.06, 111.33, 79.74, 55.42, 50.74, 28.46, 28.44. **LC-MS [m/z+H] = 293.3.**



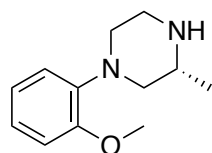
Synthesis of 1-(2-methoxyphenyl)piperazine (1.6).

Following the general procedure, 1-(2-methoxyphenyl)piperazine was isolated as an off white solid (15 mg, quantitative yield). **LC-MS [m/z+H] = 193.1.**



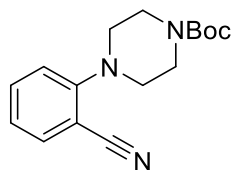
Synthesis of *tert*-butyl (*R*)-4-(2-methoxyphenyl)-2-methylpiperazine-1-carboxylate.

Following the general procedure, crude reaction material was purified by column chromatography (10 – 40% ethyl acetate in hexanes) to provide the title compound as a clear oil (35 mg, 23%). ¹H NMR (400 MHz, CDCl₃) δ 7.20 – 6.57 (m, 4H), 4.28 (s, 1H), 3.92 (d, *J* = 14.0 Hz, 1H), 3.83 (d, *J* = 2.3 Hz, 3H), 3.31 (d, *J* = 11.8 Hz, 2H), 1.42 (dt, *J* = 6.5, 3.2 Hz, 9H). ¹³C NMR (101 MHz, CDCl₃) δ 154.74, 152.37, 132.54, 133.77, 121.33, 112.06, 106.36, 79.78, 55.97, 55.67, 50.42, 49.62, 38.89, 28.44, 15.94. [m/z+H] = 307.2.



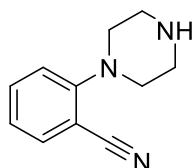
Synthesis of (*R*)-1-(2-methoxyphenyl)-3-methylpiperazine (1.22).

Following the general procedure, (*R*)-1-(2-methoxyphenyl)-3-methylpiperazine was isolated as an off white solid (15 mg, quantitative yield). [m/z+H] = 207.3.



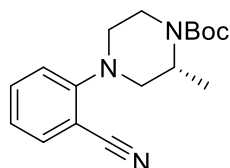
Synthesis of *tert*-butyl 4-(2-cyanophenyl)piperazine-1-carboxylate. Following the general procedure, crude reaction mixture was purified by column chromatography (10

– 40% ethyl acetate in hexanes) to provide the title compound as a clear oil (105 mg, 33%). **¹H NMR (400 MHz, CDCl₃)** δ 7.62 (dt, J = 7.7, 1.6 Hz, 1H), 7.54 (ddq, J = 9.6, 7.5, 1.2 Hz, 1H), 3.70 (tt, J = 3.7, 2.0 Hz, 4H), 3.28 – 3.14 (m, 4H), 1.51 (s, 9H). **¹³C NMR (101 MHz, CDCl₃)** δ 154.60, 134.42, 133.89, 122.60, 119.17, 117.94, 106.37, 80.05, 51.62, 43.52, 28.33. **LC-MS [m/z+H]** = 287.4.



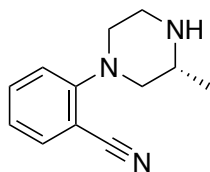
2-(piperazin-1-yl)benzonitrile (1.30).

Following the general procedure, 2-(piperazin-1-yl)benzonitrile was isolated as an off white solid (45 mg, quantitative yield). For characterization purposes, 2-(piperazin-1-yl)benzonitrile was taken up in DCM and basified to pH = 11. The organic layer passed through a phase separator, and concentrated to yield **1.30** as a yellow oil. **¹H NMR (400 MHz, CDCl₃)** δ 7.56 (dd, J = 7.9, 1.7 Hz, 1H), 7.53 – 7.45 (m, 1H), 7.04 – 6.97 (m, 2H), 3.23 – 3.16 (m, 4H), 3.11 – 3.05 (m, 4H). **¹³C NMR (101 MHz, CDCl₃)** δ 156.10, 134.33, 133.81, 121.71, 118.70, 118.46, 105.98, 52.77, 46.09. **LC-MS [m/z+H]** = 202.7.



tert-butyl (R)-4-(2-cyanophenyl)-2-methylpiperazine-1-carboxylate.

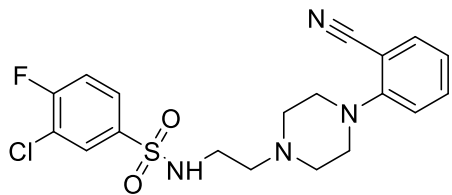
Following the general procedure, crude reaction mixture was purified by column chromatography (10 – 40% ethyl acetate in hexanes) to provide the title compound as a clear oil (75 mg, 23%). **¹H NMR (400 MHz, CDCl₃)** δ 7.51 (dd, *J* = 7.7, 1.7 Hz, 1H), 7.45 – 7.39 (m, 1H), 7.00 – 6.91 (m, 2H), 4.30 (d, *J* = 6.7 Hz, 1H), 3.91 (dd, *J* = 13.2, 3.3 Hz, 1H), 3.38 – 3.20 (m, 3H), 2.90 (dd, *J* = 11.6, 3.7 Hz, 1H), 2.76 (td, *J* = 11.5, 3.4 Hz, 1H), 1.41 (s, 8H), 1.35 (d, *J* = 6.8 Hz, 3H). **¹³C NMR (101 MHz, CDCl₃)** δ 155.64, 154.54, 134.44, 133.76, 122.17, 118.93, 118.09, 106.36, 79.78, 56.26, 51.51, 47.14, 38.87, 28.36, 15.51. **LC-MS [m/z+H] = 302.3.**



(R)-2-(3-methylpiperazin-1-yl)benzonitrile.

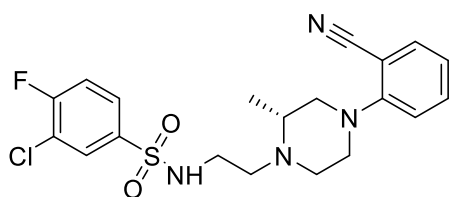
Following the general procedure, (R)-2-(3-methylpiperazin-1-yl)benzonitrile was isolated as an off white solid (25 mg, quantitative yield). **LC-MS [m/z+H] = 202.1.**

General Procedure for S_N2 Reaction: In a close reaction vessel, arylhalide (1.1 equiv.), the hydrochloride salt of the desired *N*-arylpiperazine (1 equiv.), NaI (1.5 equiv.), and K₂CO₃ (2 equiv.), were dissolved in DCM (0.2 M). The reaction mixture stirred at 95 °C for 6 h. The reaction was then diluted with DCM, filtered, dried over MgSO₄, and concentrated. The crude product was purified by column chromatography (30-70% EtOAc/hexanes) to provide the final compound.



3-chloro-*N*-(2-(4-(2-cyanophenyl)piperazin-1-yl)ethyl)-4-fluorobenzenesulfonamide (1.32).

Following the general procedure, (3-chloro-*N*-(2-(4-(2-cyanophenyl)piperazin-1-yl)ethyl)-4-fluorobenzenesulfonamide was isolated as an off white amorphous solid (12 mg, 83%). **¹H NMR (400 MHz, CDCl₃)** δ 7.97 (dd, *J* = 6.7, 2.3 Hz, 1H), 7.80 (ddd, *J* = 8.7, 4.3, 2.3 Hz, 1H), 7.57 (dd, *J* = 7.7, 1.6 Hz, 1H), 7.51 (ddd, *J* = 9.2, 7.6, 1.7 Hz, 1H), 7.29 (t, *J* = 8.5 Hz, 1H), 7.04 (qd, *J* = 8.5, 8.0, 2.9 Hz, 2H), 3.23 (t, *J* = 4.8 Hz, 4H), 3.12 (t, *J* = 5.7 Hz, 2H), 2.67 (t, *J* = 4.8 Hz, 4H), 2.63 (t, *J* = 5.8 Hz, 2H). **¹³C NMR (101 MHz, CDCl₃)** δ 160.58 (d, *J*_{CF} = 257.8 Hz), 155.24, 136.91 (d, *J*_{CF} = 3 Hz), 134.33, 133.94, 130.04, 127.62, 127.54, 122.49 (d, *J*_{CF} = 18 Hz), 122.32, 118.81, 118.26, 117.42 (d, *J*_{CF} = 22 Hz), 106.35, 55.89, 52.69, 51.17, 39.05. **LC-MS [m/z+H] = 423.3.**



(*R*)-3-chloro-*N*-(2-(4-(2-cyanophenyl)-2-methylpiperazin-1-yl)ethyl)-4-fluorobenzenesulfonamide (1.55).

Following the general procedure, (*R*)-3-chloro-*N*-(2-(4-(2-cyanophenyl)-2-methylpiperazin-1-yl)ethyl)-4-fluorobenzenesulfonamide was isolated as a yellow oil (10

mg, 78%). **¹H NMR (400 MHz, CDCl₃)** δ 7.98 (dd, *J* = 6.7, 2.3 Hz, 1H), 7.83 (ddd, *J* = 8.6, 4.3, 2.3 Hz, 1H), 7.58 (dd, *J* = 7.7, 1.6 Hz, 1H), 7.53 (ddd, *J* = 8.3, 7.5, 1.7 Hz, 1H), 7.29 (t, *J* = 8.5 Hz, 1H), 7.09 (td, *J* = 7.6, 1.0 Hz, 1H), 7.05 (d, *J* = 8.3 Hz, 1H), 3.55 – 3.05 (m, 8H), 2.84 (d, *J* = 41.4 Hz, 2H), 1.37 (d, *J* = 5.9 Hz, 3H). **¹³C NMR (101 MHz, CDCl₃)** δ 160.61 (d, *J*_{CF} = 257.2 Hz), 154.33, 136.91 (d, *J*_{CF} = 3.9 Hz), 134.20 (d, *J*_{CF} = 11.6 Hz), 133.60, 131.74, 130.04, 127.63 (d, *J*_{CF} = 8.4 Hz), 123.16, 122.44 (d, *J*_{CF} = 18.7 Hz), 119.30, 118.01, 117.54 (d, *J*_{CF} = 22.4 Hz), 106.72, 56.61, 53.62, 49.85, 38.84, 14.23, 1.03. **LC-MS [m/z+H] = 437.5.**

CHAPTER II

DEVELOPMENT OF AN METABOTROPIC GLUTAMATE RECEPTOR 4 POSITIVE ALLOSTERIC MODULATOR

Background and Introduction

G Protein-Coupled Receptors: Metabotropic Glutamate Receptors

Glutamate is the most abundant neurotransmitter in the central nervous system (CNS) and is involved in virtually every excitatory brain function.³⁶ The metabotropic glutamate (mGlu) receptors are G protein-coupled receptors (GPCRs) that are widely distributed throughout the CNS.³⁷ GPCRs encompass a wide variety of extracellular proteins that are responsible for sensing diverse chemical messengers and activating internal signal transduction pathways.³⁸ In eukaryotes, GPCRs are the most prevalent transmembrane proteins with greater than 800 GPCRs identified in the human genome and are involved in endocrinal signaling pathways, anti-inflammatory and immune responses, physiological homeostasis, human behavior, and the chemical senses of smell and taste.³⁹ Considering their abundance in human biology, GPCRs have proven to be pharmacologically lucrative targets with 475 drugs approved by the Food and Drug Administration (FDA) clinically available that target 108 different GPCRs.⁴⁰

Structurally, all GPCRs all share a common counter-clockwise bundle structure of seven transmembrane (7TM) helices and associate with intracellular heterotrimeric guanine nucleotide-binding proteins (G proteins).³⁸ GPCRs are divided into 6 classes based on sequence homology and structural similarity, with mGlu

receptors belonging to Class C.³⁷ Class C mGlu exist as constitutive, covalently linked dimers of two mGlu subunits.⁴¹

The Class C family is further characterized by the large extracellular N-terminus domain, specifically termed the Venus flytrap domain (VFD) for mGlu (**Figure 2.1**). Evidence suggests that two VFDs dimerize together, back to back, forming a hydrophobic binding pocket.⁴² The Venus flytrap nomenclature is derived from the mechanism in which the two lobes of the VFD ‘bite’ down on glutamate upon binding, inducing the conformational change necessary to induce receptor activation and subsequent signaling cascades.⁴³ Following glutamate binding, conformational changes are conducted down the structurally-rigid cysteine-rich domain (CRD), comprised of 9 cysteine residues, of which 8 engage in disulfide bonds.⁴⁴ The 9th cysteine forms a disulfide bridge with the VFD, which propagates the structural changes from the VFD to the 7TM, inducing its rearrangement.⁴⁵ This rearrangement results in the dissociation of the heterotrimeric G protein complex in which the $G_{\beta\gamma}$ and G_{α} subunits can participate in secondary messenger cascades.^{41, 46, 47}

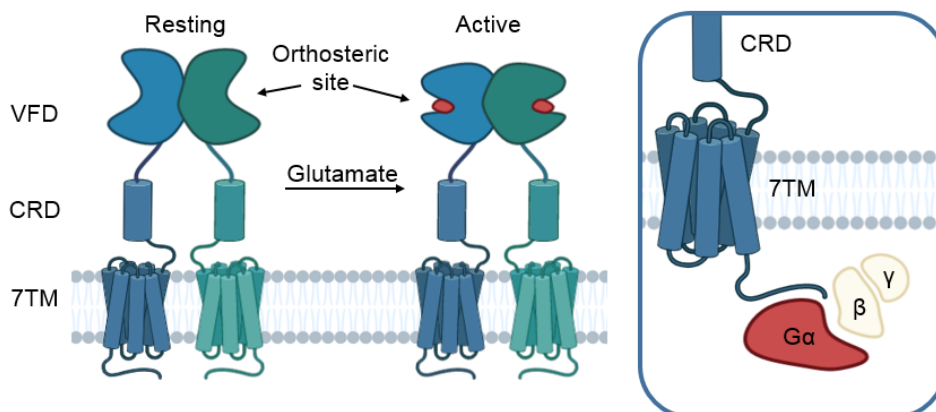


Figure 2.1: General structure of an mGlu receptor in its resting and activated state, and the intracellular heterotrimeric G-protein complex.

The mGlu family is composed of three groups of 8 members (mGlu₁₋₈), which are categorized based on sequence homology, G protein signaling, and ligand binding. Group I consists of mGlu_{1,5}, group II of mGlu_{2,3}, and group III with mGlu_{4,6,7,8}.⁴⁸ Group I is coupled to G_{αq}, wherein activation of the receptor results in the release of the G_{αq} subunit from the heterotrimeric G protein.^{46, 49} G_{αq} activates phospholipase C (PLC), which cleaves phosphatidylinositol 4,5-bisphosphate (PIP₂) into diacyl glycerol (DAG) and inositol 1,4,5-trisphosphate (IP₃), the latter of which is cytosolic and activates a number of receptors.⁵⁰ Importantly, it activates endoplasmic reticulum (ER) bound calcium channels, which allows for influx of calcium ions into the cytosol.^{51, 52} Group 2 and 3 are both coupled to G_{αi}, where the interaction of the G protein with adenylate cyclase (AC) results in a reduced activation of AC, which converts adenosine triphosphate (ATP) into cyclic adenosine monophosphate (cAMP).⁵¹ This reduction in cellular cAMP can have a myriad of intracellular effects, including impacts on cellular ion channels and the ser/thr-specific protein kinase A (PKA) family of protein kinases.⁴⁴ G_{i/o} GPCRs can also directly affect ion channels via the βγ subunits and this may be even more important in modulating synaptic transmission than changes in cAMP.⁵³

Orthosteric vs. Allosteric Ligands for mGlu receptors

Traditional probe development approaches target the orthosteric site of a target protein, where its endogenous ligands bind. However, such an approach would be unsuccessful for modulating the mGlu receptor subtypes. As all mGlu receptors bind glutamate, the orthosteric binding site is highly conserved across all subtypes.⁵⁴ Such homology within the active site does not provide opportunities to confer subtype

selectivity needed for interrogating the physiological importance of a single mGlu receptor subtype.⁵⁵

Further, orthosteric ligands have proven to be an unsuccessful approach when the therapeutic activity for receptor activation is small.⁵⁶ Orthosteric modulation results in sustained receptor activation or deactivation, and chronic dosing can result in receptors become desensitized and internalized, or over-activated.⁵⁷ Thus, orthosteric drugs lose efficacy over time. For example, drugs of abuse that target the opioid receptor, such as heroin and morphine require increasing doses to achieve the same therapeutic effect over chronic administration due to receptor desensitization.⁵⁸⁻⁶¹

The detriments associated with orthosteric modulation of CNS GPCRs is further exemplified by xanomeline, a muscarinic acetylcholine receptor 1 and 4 (M₁/M₄) preferring orthosteric agonist.⁶² Xanomeline was developed with the intention of improving cognition in schizophrenia patients. Unfortunately, during the clinical trial, patients suffered from severe side effects that were indicative of cholinergic toxicity.⁶³ This was attributed to over-activation of the muscarinic receptors and off-target activity at M₂ and M₃ receptors.⁶⁴

Finally, orthosteric ligand development for the mGlu family would require pursuing small-molecules derived from glutamate. Such medicinal chemistry efforts would result in amino acid-like molecules, known to have poor *in vivo* pharmacokinetic (PK) properties. Small, charged molecules are known to suffer from high hepatic clearance and would not be brain penetrant with traditional methods of administration.⁶⁵ This problem is not unique to the mGlu family and plagues several types of CNS

receptors as their endogenous ligands range from neurotransmitters to large peptides, such as hormones.

Due to the challenges associated with orthosteric drug discovery, allosteric modulation has become a burgeoning area for medicinal chemistry efforts.⁶⁶⁻⁶⁹ Allosteric modulators act at an alternative site distinct from the orthosteric site (allosteric site), to potentiate the action of the endogenous ligand. Allosteric modulators can be classified as either positive allosteric modulators (PAMs), negative allosteric modulators (NAMs), or neutral allosteric ligands (NALs).⁶⁷ Pure PAMs increase the potency and efficacy of the endogenous ligand, but do not result in signaling in the absence of agonist. Potentiation is accomplished by stabilizing an active conformation of the receptor, which can improve affinity, efficacy, or both. Agonist-PAMs (or ago-PAMs) are capable of activating the target in the absence of the orthosteric agonist, but also potentiates the receptor activation upon interaction with the orthosteric ligand.⁷⁰ NAMs reduce the effect of the receptors orthosteric ligand by stabilizing an inactive conformation of the target. NALs have no impact on signaling through the orthosteric site but can block the effect of other allosteric ligands that bind in the same pocket.

The first class of allosteric modulators to gain FDA approval were the benzodiazapienes, which have sedative and anxiolytic effects by enhancing the effect of γ -aminobutyric acid (GABA) at GABA receptors.^{68, 71, 72} Otherwise, few drugs that are allosteric modulators are clinically available, due to the inherent difficulty associated with developing allosteric modulators.⁷³ First, SAR tends to be steep; subtle changes can completely negate activity, or result in a mode switch (i.e. NAM to PAM switch). Additionally, allosteric sites are often not evolutionarily conserved like orthosteric sites,

which complicates the translation of activity from animal models to human patients. Finally, allosteric modulators tend to be extremely lipophilic, as allosteric sites are often on the exterior of the target protein. Thus, they rely on hydrophobic interactions to drive binding, which results in small molecules with unfavorable pharmacological profiles.

Despite the challenges of development, allosteric modulators (AMs) have proven to function as invaluable tool compounds in preclinical studies and in human patients.⁶⁸ In summary, allosteric modulation has been proven to offer several benefits over orthosteric agents: (1) AMs provide greater receptor and receptor subtype selectivity due to the high sequence divergence in allosteric sites relative to the conserved orthosteric domains⁷⁴ (2) AMs are quiescent in the absence of endogenous ligand and thus do not disrupt the physiological cycle of receptor activation,⁷⁵ and (3) AMs allow for a high degree of titratability of the pharmacological effect necessary for targets with narrow windows of therapeutic relevance.⁶⁷

mGlu₄ and Parkinson's Disease

Behind Alzheimer's disease, Parkinson's Disease (PD) is the second most common neurodegenerative disorder affecting 1.8% of individuals aged 65 or older worldwide.⁷⁶ The estimated economic burden of PD is estimated to be \$25 billion per year in the US alone.⁷⁷ PD is characterized by the progressive loss of dopaminergic neurons in the Substantia Nigra pars compacta (SNpc), causing dysfunction of the basal ganglia motor circuit and the eventual onset of the hallmark motor symptoms of PD (resting tremor, rigidity, bradykinesia and postural instability) which can be fatal

(asphyxiation).⁷⁸ The cause of PD is unknown, with known genetic and environmental factors associated with an increase in risk.⁷⁷

There are currently no disease-modifying treatments for PD, with only palliative treatments and dopamine replacement strategies (levodopa) as the main avenues. Some patients qualify for deep brain stimulation (DBS), a surgical treatment in which electrodes are implanted into the brain.⁷⁹ DBS sends continuous electrical pulses to the target areas in the brain, modifying the abnormal activity in that area of the brain that is causing symptoms.⁸⁰ However, this is an invasive surgery that is not appropriate for all PD patients. Thus, the dopamine precursor levodopa (L-DOPA), remains the gold standard for PD treatment.

During the first years of L-DOPA treatment, it markedly improves the motor symptoms associated with PD and in turn, patient quality of life. However, following long-term treatment with L-DOPA and as the disease progresses, increasing doses of L-DOPA become necessary.⁸¹ This leads to the emergence of debilitating side effects, including motor fluctuations and dyskinesia.⁸² Consequently, there has been a major push towards the discovery of novel therapies that work to prevent or delay the onset of PD, or manage the motor complications in PD patients.

One promising approach is targeting the pathways within the basal ganglia (BG). The output of the BG is dictated by two major neural circuits that exert opposing influences.⁸³ Coordination between the direct (stimulatory) and indirect (inhibitory) networks are important for facilitating the execution of motor planning and motor movements.⁸⁰ In both pathways, dopamine regulates the glutamatergic inputs and

therefore controls the ultimate output. In PD, the loss of dopaminergic control leads to an imbalance in favor of a hyperactive indirect pathway, and a subsequent pathological inhibition of the motor cortex.^{83, 84} Thus, restraining the aberrant inhibitory activity of the indirect pathway proves to be a promising approach towards controlling the motor dysfunction of PD.⁸³ Receptor classes present in the indirect pathway have been studied in order to identify novel targets that may provide disease-modifying treatment options for PD.⁸⁰

One such receptor is mGlu₄, localized on pre-synaptic terminals of intrinsic basal ganglia pathways where their positive allosteric modulation may serve to restrict neurotransmitter release and result in anti-PD benefits.⁸⁵ Several mGlu₄ PAM *in vivo* tool compounds have been developed (**Figure 2.2**), offering evidence that mGlu₄ PAMs could be novel, disease-modifying treatment options. Valenti et al. showed that stimulation of presynaptic mGlu₄ at these synapses reduced excessive glutamate release.⁸⁶ Battaglia et al. and Betts et al. further demonstrated that administration of mGlu₄ PAMs prevented dopaminergic cell death in the substantia nigra induced by either MPTP or 6-OHDA treatment (both selectively destroy dopaminergic neurons).⁸⁷ Additionally, administration of an mGlu₄ PAM reduced ischemic brain damage, and an mGlu₄ PAM has also been shown to reduce inflammatory responses in microglia, providing potential mechanisms for neuroprotection.

The structural classes of disclosed mGlu₄ PAMs are wide-ranging, from triaryl amines⁸⁸, **2.1**, cyclohexyl amides⁸⁹, **2.2**, picolinamides⁹⁰, **2.3**, and pyrazolo[4,3-*b*]pyridines, **2.4**, which speaks to the variability or number of allosteric binding sites of the receptor. Although much of the work remains in the preclinical stage, Prexton

Therapeutics advanced their lead molecule, **2.5**, into clinical studies in Europe.⁹¹ However, **2.5** failed in Phase II clinical trial due to a lack of efficacy in modulating the effects of long-term L-DOPA use.⁸¹ Therefore, bringing forth multiple new structural classes of PAMs for clinical evaluation is a high priority for the validation of this receptor in the clinic.⁷⁸

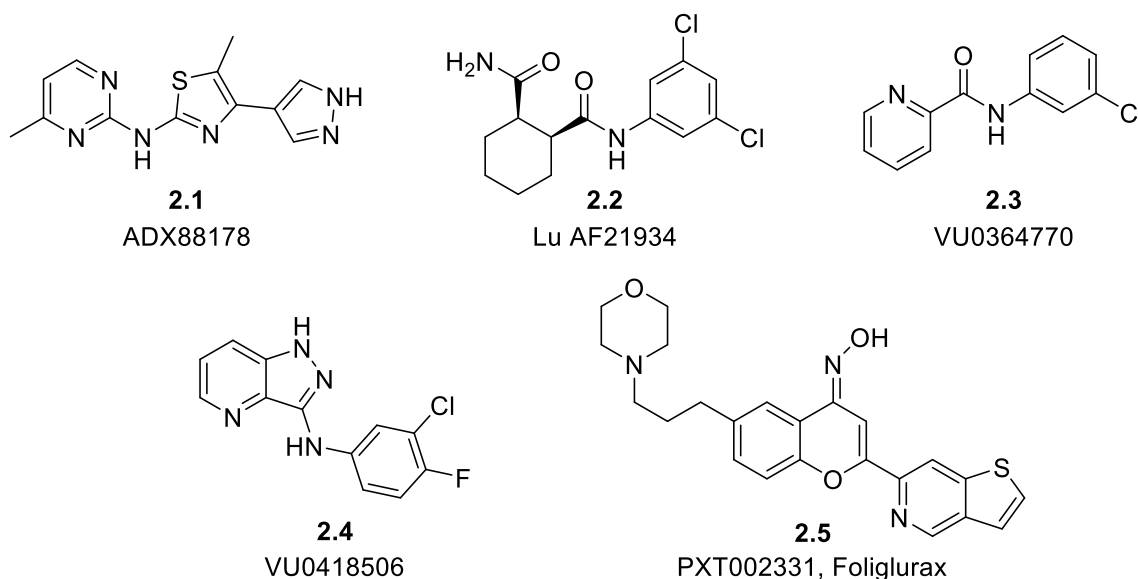


Figure 2.2: Structures of reported mGlu₄ PAMs **2.1–2.4** with efficacy in preclinical rodent and/or nonhuman primate models of PD and **2.5**, the first mGlu₄ PAM to advance into clinical trial.

Conclusions

Using a scaffold identified in a previous HTS campaign identifying PAMs for the mGlu_{2/4} receptor heterodimer, we will work to develop a novel chemotype that is structurally different from previously disclosed mGlu₄ PAMs. SAR and DMPK studies will be used to guide our chemical approaches, as a co-crystal structure of mGlu₄ is unavailable. We hope to achieve the necessary subtype selectivity and potency

required for *in vivo* validation via behavioral studies. The following section of this chapter will summarize our efforts that led to the discovery of a novel mGlu₄ PAM chemotype.

Materials and Methods

General Synthetic Methods and Instrumentation

All NMR spectra were recorded on a 400 MHz AMX Bruker NMR spectrometer. ¹H and ¹³C chemical shifts are reported in δ values in ppm downfield with the deuterated solvent as the internal standard. Data are reported as follows: chemical shift, multiplicity (s = singlet, d = doublet, t = triplet, q = quartet, b = broad, m = multiplet), integration, coupling constant (Hz). Low resolution mass spectra were obtained on an Agilent 6120 or 6150 with ESI source. MS parameters were as follows: fragmentor: 70, capillary voltage: 3000 V, nebulizer pressure: 30 psig, drying gas flow: 13 L/min, drying gas temperature: 350 °C. Samples were introduced via an Agilent 1290 UHPLC comprised of a G4220A binary pump, G4226A ALS, G1316C TCC, and G4212A DAD with ULD flow cell. UV absorption was generally observed at 215 nm and 254 nm with a 4 nm bandwidth. Column: Waters Acquity BEH C18, 1.0 x 50 mm, 1.7 μ m. Gradient conditions: 5% to 95% MEEN in H₂O (0.1% TFA) over 1.4 min, hold at 95% MEEN for 0.1 min, 0.5 mL/min, 55 °C. High resolution mass spectra were obtained on an Agilent 6540 UHD Q-TOF with ESI source. MS parameters were as follows: fragmentor: 150, capillary voltage: 3500 V, nebulizer pressure: 60 psig, drying gas flow: 13 L/min, drying gas temperature: 275 °C. Samples were introduced via an Agilent 1200 UHPLC comprised of a G4220A binary pump, G4226A ALS, G1316C TCC, and G4212A DAD

with ULD flow cell. UV absorption was observed at 215 nm and 254 nm with a 4 nm bandwidth. Column: Agilent Zorbax Extend C18, 1.8 μm , 2.1 x 50 mm. Gradient conditions: 5% to 95% MECN in H_2O (0.1% formic acid) over 1 min, hold at 95% MECN for 0.1 min, 0.5 mL/min, 40 $^\circ\text{C}$. For compounds that were purified on a Gilson preparative reversed-phase HPLC, the system comprised of a 333 aqueous pump with solvent-selection valve, 334 organic pump, GX-271 or GX-281 liquid handler, two column switching valves, and a 155 UV detector. UV wavelength for fraction collection was user-defined, with absorbance at 254 nm always monitored. Method 1: Phenomenex Axia-packed Luna C18, 30 x 50 mm, 5 μm column. Mobile phase: MECN in H_2O (0.1% TFA). Gradient conditions: 0.75 min equilibration, followed by user defined gradient (starting organic percentage, ending organic percentage, duration), hold at 95% MECN in H_2O (0.1% TFA) for 1 min, 50 mL/min, 23 $^\circ\text{C}$. Method 2: Phenomenex Axia-packed Gemini C18, 50 x 250 mm, 10 μm column. Mobile phase: MECN in H_2O (0.1% TFA). Gradient conditions: 7 min equilibration, followed by user defined gradient (starting organic percentage, ending organic percentage, duration), hold at 95% MECN in H_2O (0.1% TFA) for 7 min, 120 mL/min, 23 $^\circ\text{C}$. All reagents were purchased from Aldrich Chemical Co. and were used without purification. All final compounds were >98% pure by LCMS (254 nm, 214 nM and ELSD). Following these purification protocols, final compounds were transferred to a barcode vial and diluted to a concentration of 10 μM using molecular biology grade dimethylsulfoxide (DMSO). These compounds were registered into Dotmatics and assigned a VU identification (VUID) number before being tested in the primary screening assay.

GIRK-Mediated Thallium Flux Assay

Cells were plated into 384 well, black-walled, clear-bottom poly-D-lysine coated plates (Greiner) at a density of 15,000 cells/20 μ l/well in DMEM containing 10% dialyzed FBS, 20 mM HEPES, and 100 units/ml penicillin/streptomycin (Assay Media). Plated cells were incubated overnight at 37 °C in the presence of 5% CO₂. The following day, the medium was removed from the cells and 20 μ l/well of 330 nM Fluo Zn₂ (Invitrogen; prepared as a stock in DMSO and mixed in a 1:1 ratio with pluronic acid F-127) in Assay Buffer (Hanks Balanced Salt Solution (Invitrogen) containing 20 mM HEPES pH 7.3) was added to the plated cells. Cells were incubated for one h at room temperature and the dye was replaced with the 20 μ l of Assay Buffer. Glutamate was diluted in Thallium Buffer (125 mM sodium bicarbonate (added fresh the morning of the experiment), 1 mM magnesium sulfate, 1.8 mM calcium sulfate, 5 mM glucose, 12 mM thallium sulfate, 10 mM HEPES, pH 7.3) at 5x the final concentration to be assayed. For concentration-response curve experiments, compounds were serially diluted 1:3 into 10 point concentration response curves in DMSO, transferred to daughter plates using the Echo, and diluted in Assay Buffer to a 2X final concentration. Cell plates and compound plates were loaded onto a Hamamatsu FDSS 6000 or 7000 kinetic imaging plate reader. Baseline readings were taken (10 images at 1 Hz, excitation, 470 \pm 20 nm emission, 540 \pm 30 nm) and test compounds were added in a 20 μ l volume and incubated for 2.5 min prior to the addition of 10 μ l of Thallium Buffer \pm agonist. After the addition of agonist, data were collected for an additional 2 min. The slope of the fluorescence increase beginning 5 sec after thallium/agonist addition and ending 15 sec

after thallium/agonist addition was calculated. Data were analyzed using a four-parameter logistical equation in Dotmatics or GraphPad Prism software.

In vitro DMPK Methods: Intrinsic Clearance in Rat Liver Microsomes

Rat liver microsomes (0.5 mg/mL) and 1 μ M test compound were incubated in 100 mM potassium phosphate pH 7.4 buffer with 3 mM MgCl₂ at 37 °C with constant shaking. After a 5 min preincubation, the reaction was initiated by addition of NADPH (1 mM). At selected time intervals (0, 3, 7, 15, 25, and 45 min), 50 μ L aliquots were taken and subsequently placed into a 96-well plate containing 150 μ L of cold acetonitrile with internal standard (50 ng/mL carbamazepine). Plates were then centrifuged at 3000 rcf (4 °C) for 10 min, and the supernatant was transferred to a separate 96-well plate and diluted 1:1 with water for LC/MS/MS analysis. The in vitro half-life ($T_{1/2}$, min, Eq. 1), intrinsic clearance (CL_{INT} , mL/min/kg, Eq. 2) and subsequent predicted hepatic clearance (CL_{HEP} , mL/min/kg, Eq. 3) were determined employing the following equations:

$$(1) \quad T_{1/2} = \frac{\ln(2)}{k}$$

where k represents the slope from linear regression analysis of the natural log percent remaining of test compound as a function of incubation time

$$(2) \quad CL_{int} = \frac{0.693}{in\ vitro\ T_{1/2}} \times \frac{mL\ incubation}{mg\ microsomes} \times \frac{45\ mg\ microsomes}{grams\ liver} \times \frac{45^a\ gram\ liver}{kg\ body\ weight}$$

^ascale-up factor that is species specific

$$(3) \quad CL_{hep} = \frac{Q_h \cdot CL_{int}}{Q_h + CL_{int}}$$

Where Qh (hepatic blood flow) is species specific

Rat Plasma Protein Binding

The protein binding of each compound was determined in rat or mouse plasma via equilibrium dialysis employing HTDialysis Teflon dialysis chamber and cellulose membranes (MWCO 12-14 K) (HTDialysis LLC, Gales Ferry, CT). Plasma was added to the 96-well plate containing test compound and mixed thoroughly for a final concentration of 5 μ M. Subsequently, 150 μ L of the plasma-compound mixture was transferred to the dialysis chamber, with an accompanying 150 μ L of phosphate buffer (25 mM, pH 7.4) on the other side of the membrane. The device plate was sealed and incubated for 4 h at 37 $^{\circ}$ C with shaking. At completion, aliquots from each chamber were diluted 1:1 with either plasma (for the buffer sample) or buffer (for the plasma sample) and transferred to a new 96-well plate, at which time ice-cold acetonitrile containing internal standard (50 ng/mL carbamazepine) (2 volumes) was added to extract the matrices. The plate was centrifuged (3000 rcf, 10 min) and supernatants transferred and diluted 1:1 (supernatant: water) into a new 96 well plate, which was then sealed in preparation for LC/MS/MS analysis. Each compound was assayed in triplicate within the same 96-well plate. Fraction unbound was determined using the following equation:

$$F_u = \frac{Conc_{buffer}}{Conc_{plasma}}$$

Rat Brain Homogenate Binding

The brain homogenate binding of each compound was determined in brain homogenate via equilibrium dialysis employing HTDialysis Teflon dialysis chamber and cellulose membranes (MWCO 12-14 K) (HTDialysis LLC, Gales Ferry, CT). Brain tissue homogenate was prepared by diluting one volume whole mouse or rat brain tissue with one to three volumes (species specific) of phosphate buffer (25 mM, pH 7.4). The mixture was then subjected to mechanical homogenization employing a MiniBeadbeater™ and 1.0 mm Zirconia/Silica Beads (BioSpec Products). Brain homogenate spiked with test compound and mixed thoroughly for a final concentration of 5 µM. Subsequently, 150 µL of the brain homogenate-compound mixture was transferred to the dialysis chamber with an accompanying 150 µL of phosphate buffer (25 mM, pH 7.4) on the other side of the membrane. The block was sealed and incubated for 6 h at 37 °C with shaking. At completion, aliquots from each side of the chamber were diluted 1:1 with either brain homogenate (to the buffer side) or buffer (to the brain homogenate side) in a new 96 well plate, at which time ice-cold acetonitrile containing internal standard (50 ng/mL carbamazepine) was added to extract the matrices. The plate was centrifuged (3000 rcf, 10 min) and supernatants transferred and diluted 1:1 (supernatant: water) into a new 96 well plate, which was then sealed in preparation for LC/MS/MS analysis. Each compound was assayed in triplicate within the same 96-well plate. Fraction unbound was determined using the following equation:

$$F_{u,tissue} = \frac{1/D_f}{\left(\frac{1}{F_{u,hom}} - 1\right) + 1/D_f}$$

Where $F_{u, \text{hom}}$ represent the measured fraction unbound in the diluted homogenate and Df represents dilution factor.

LC/MS/MS Analysis of Samples from In Vitro Assays

Samples were analyzed via electrospray ionization (ESI) on an AB Sciex API4000 (Foster City, CA) triple-quadrupole instrument that was coupled with Shimadzu LC-10AD pumps (Columbia, MD) and a Leap Technologies CTC PAL auto-sampler (Carrboro, NC). Analytes were separated by gradient elution using a Fortis C18 3.0 x 50 mm, 3 μm column (Fortis Technologies Ltd, Cheshire, UK) thermostated at 40 °C. HPLC mobile phase A was 0.1% formic acid in water (pH unadjusted), mobile phase B was 0.1% formic acid in acetonitrile (pH unadjusted). The gradient started at 10% B after a 0.2 min hold and was linearly increased to 90% B over 1.2 min; held at 90% B for 0.1 min and returned to 10% B in 0.1 min followed by a re-equilibration (0.9 min). The total run time was 2.5 min and the HPLC flow rate was 0.5 mL/min. The source temperature was set at 500 °C and mass spectral analyses were performed using multiple reaction monitoring (MRM), with transitions specific for each compound utilizing a Turbo-Ionspray® source in positive ionization mode (5.0 kV spray voltage).

In Vivo PK Methods

All rodent PK experiments were conducted in accordance with the National Institute of Health regulations of animal care covered in Principles of Laboratory Animal Care (National Institutes of Health publication 85-23, revised 1985) and were approved by the Institutional Animal Care and Use Committee.

Time Course PK and Single Time Point Tissue Distribution Studies

IV cassette PK experiments in rats were carried out according to methods described previously. Briefly, a cassette of compounds (n = 4–5/cassette) were formulated from 10 mM solutions of compounds in DMSO. In order to reduce the absolute volume of DMSO that was administered, the compounds were combined and diluted with ethanol and PEG 400 to achieve a final concentration of 0.4–0.5 mg/mL for each compound (2 mg/mL total) administered in each cassette. The final dosing solutions consisted of approximately 10% ethanol, 40% PEG400, and 50% DMSO (v/v). For time course PK studies, each cassette dose was administered IV via the jugular vein to two dual-cannulated (carotid artery and jugular vein) adult male Sprague–Dawley rats, each weighing between 250 and 350 g (Harlan, Indianapolis, IN) for a final dose of 0.2–0.25 mg/kg per compound. Whole blood collections via the carotid artery were performed at 0.033, 0.117, 0.25, 0.5, 1, 2, 4, 7, and 24 h post dose and plasma samples prepared for bioanalysis. For single time point tissue distribution studies, compounds were formulated as described above (in cassette format) and dosed to male Sprague-Dawley rats for a final dose of 0.2–0.25 mg/kg per compound. Brain dissection and blood collections via the carotid artery were performed 0.25 h post dose. The brain samples were rinsed in PBS, snap frozen and stored at -80 °C. Prior to LC/MS/MS analysis, brain samples were thawed to room temperature and subjected to mechanical homogenation employing a Mini-Beadbeater™ and 1.0 mm Zirconia/Silica Beads (BioSpec Products).

LC/MS/MS Bioanalysis of Samples from In Vivo Assays

In vivo samples were analyzed via electrospray ionization (ESI) on an AB Sciex API-4000 (Foster City, CA) triple-quadrupole instrument that was coupled with Shimadzu LC-10AD pumps (Columbia, MD) and a Leap Technologies CTC PAL autosampler (Carrboro, NC). Analytes were separated by gradient elution using a Fortis C18 3.0 x 50 mm, 3 µm column (Fortis Technologies Ltd, Cheshire, UK) thermostated at 40 °C. HPLC mobile phase A was 0.1% formic acid in water (pH unadjusted), mobile phase B was 0.1% formic acid in acetonitrile (pH unadjusted). The source temperature was set at 500 °C and mass spectral analyses were performed using multiple reaction monitoring (MRM), with transitions specific for each compound utilizing a Turbolonspray® source in positive ionization mode (5.0 kV spray voltage). The calibration curves were constructed, and linear response was obtained by spiking known amounts of test compound in blank brain homogenate or plasma. All data were analyzed using AB Sciex Analyst software v1.5.1. The final PK parameters were calculated by noncompartmental analysis using Phoenix (version 6.2) (Pharsight Inc., Mountain View, CA).

In Vivo Behavioral Methods

Male Sprague-Dawley rats weighing between 292-324 grams (Harlan, Inc., Indianapolis, IN) were used. They were housed in the animal care facility certified by the American Association for the Accreditation of Laboratory Animal Care under a 12-hour light/dark cycle (lights on: 7 a.m.; lights off: 7 p.m.) and had free access to food and water. The experimental protocols performed during the light cycle were approved by

the Institutional Animals Care and Use Committee of Vanderbilt University and conformed to the guidelines established by the National Research Council Guide for the Care and Use of Laboratory Animals.

Halperidol Induced Catalepsy

VU6022296-02-01, and VU0418506-07 (both in-house synthesized by Lindsley Lab) was weighed and 2% Tween 80/0.5% methylcellulose was placed on top of the compound in serum bottles. The compounds were placed in the bath sonicator for 30 min. VU6022296 was adjusted to pH 7 and was dosed i.p. 2 ml/kg. VU506 was administrated at 10 times body weight p.o. The final solution is a suspension.

Adult male Sprague-Dawley rats were injected with 1.5 mg/kg of haloperidol i.p. (dissolved in 8% lactic acid and taken to volume of 50 ml with sterile water). One hour later some the animals are administered 10 mg/kg of VU0418506, the rest were administered VU'2296 **2.20** (3-30 mg/kg i.p.) or vehicle 15 minutes later. Cataleptic behavior is determined 15 minutes later by placing the forelimbs on a bar raised 6 cm above the table and recording the amount of time it takes for the rat to withdraw the forelimbs with a cutoff of 60 seconds. Data are expressed as mean latency to withdraw + SEM or percent inhibition of catalepsy + SEM. Blood and brain samples were taken to determine compound levels. The data for these dose-response studies were analyzed by a one-way analysis of variance. If there was a main effect of dose, then each dose group was compared with each of the other treated groups using GraphPad Prism (version 4.03, GraphPad, La Jolla, CA).

DEVELOPMENT OF AN METABOTROPIC GLUTAMATE RECEPTOR 4 POSITIVE ALLOSTERIC MODULATOR

Medicinal Chemistry Strategy

Oxo-thiazepine, VU0544412 (**2.6**, **Figure 2.3**), was identified in an HTS screen aimed at identifying a selective mGlu_{2/4} heterodimer PAMs, and preliminary investigation of this scaffold is disclosed in the dissertation of Dr. Mark Fulton. Initial interest in **2.6** was driven by the unique oxo-thiazepine core, and its resemblance to the Lundbeck scaffold (**2.2**), as both have flexible core structures and prefer halogens in the three position. Further, the unique chemotype fulfils the need to bring forth new structural classes of mGlu₄ PAMs for the validation of this receptor in the clinic. This oxo-thiazepine moiety is virtually untouched chemical space, with only a single patent in the literature disclosing similar cyclic cysteine derivatives with associated biological activities.⁹²

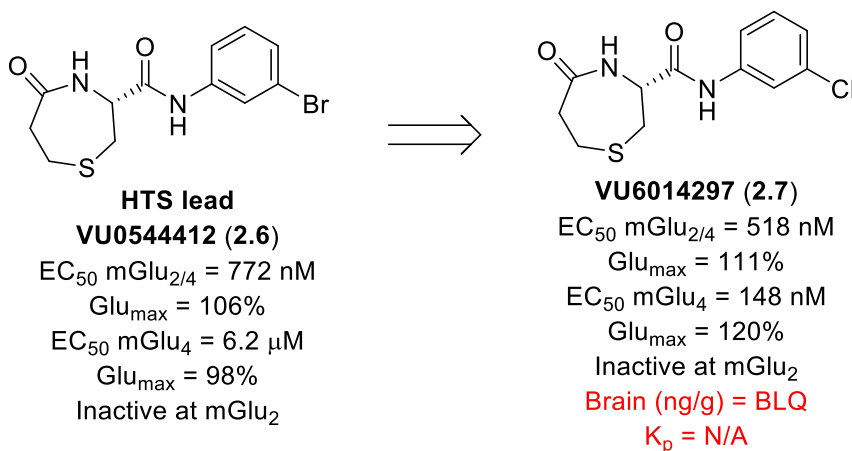
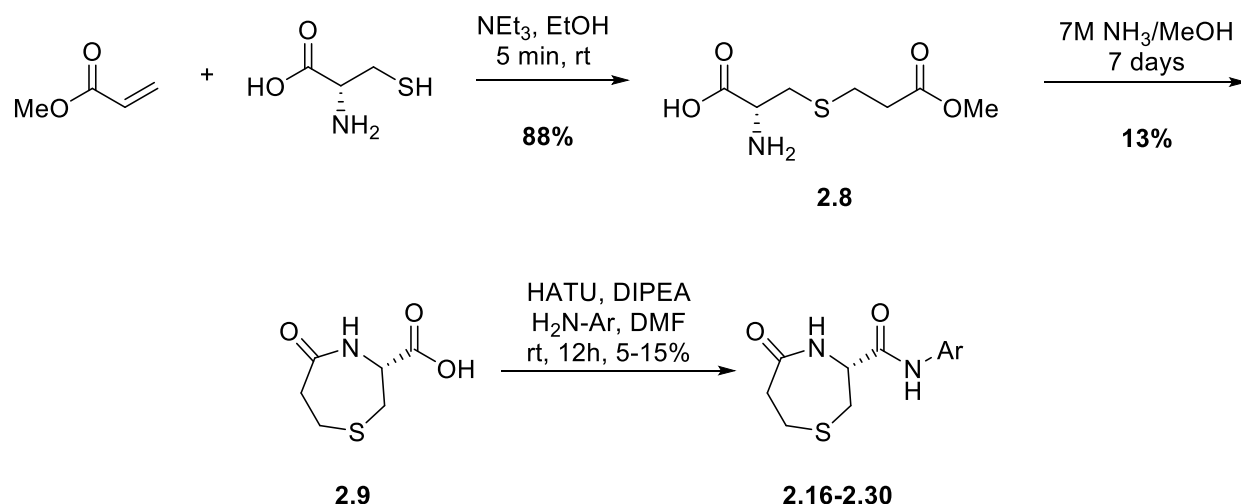


Figure 2.3: Structures of VU0544412 (**2.6**) and VU6014297 (**2.7**) from the mGlu_{2/4} campaign, with associated activities and relevant PK parameters.

Dr. Fulton improved the potency of the hit (**2.6** to **2.7**, **Figure 2.3**), but was unable to use this scaffold to develop a probe that was selective for the mGlu_{2/4} receptor heterodimer. Further, **2.7** displays modest pharmacological characteristics and is not brain penetrant, thus this scaffold was abandoned. However, the potency of these molecules in potentiating mGlu₄ activity, without mGlu₂ activity, is attractive and provides an excellent starting point for our medicinal chemistry efforts. Using Dr. Fulton's original compounds, and addressing the gaps in the SAR, we pushed to develop a novel, brain-penetrant mGlu₄ PAM. We aimed to validate this chemotype as a promising mGlu₄ PAM with *in vivo* behavioral studies.

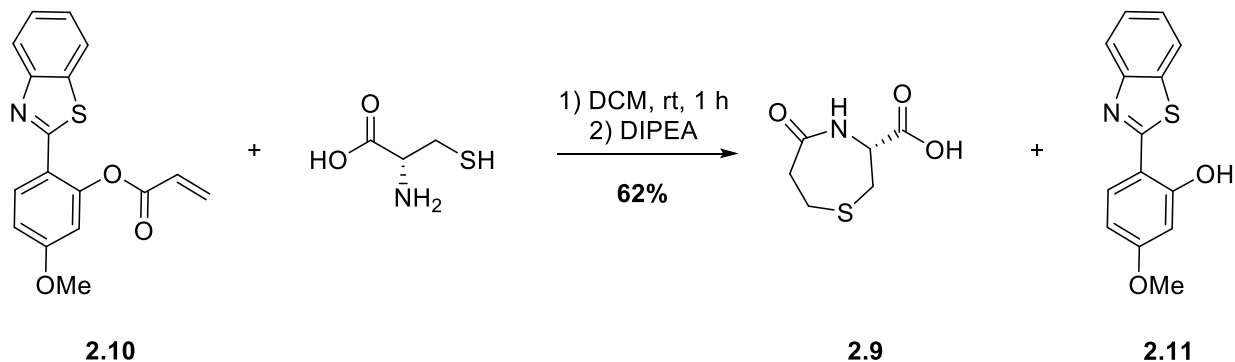
Improved Synthetic Methods for Accessing the Oxo-thiazepine Core

Previously, syntheses of **2.6** and its derivatives were conducted according to the only procedure reported in the literature.⁹³ First, methyl acrylate underwent Michael addition in the presence of L-cysteine and triethylamine gave the 1,4 thio-adduct (**2.8**) in good yields. Intramolecular cyclization was accomplished by diluting the intermediate in 7M ammonia/methanol for 7 days, with low yields. Workup of this reaction by acid base extraction gave the oxo-thiazepine carboxylic acid core, **2.9**. Derivatization occurred through a HATU-mediated amide coupling reaction with various anilines (**Scheme 2.1**). While the synthetic scheme is short, it is low yielding and time-consuming. Thus, we turned to the literature for synthetic inspiration to improve the route.



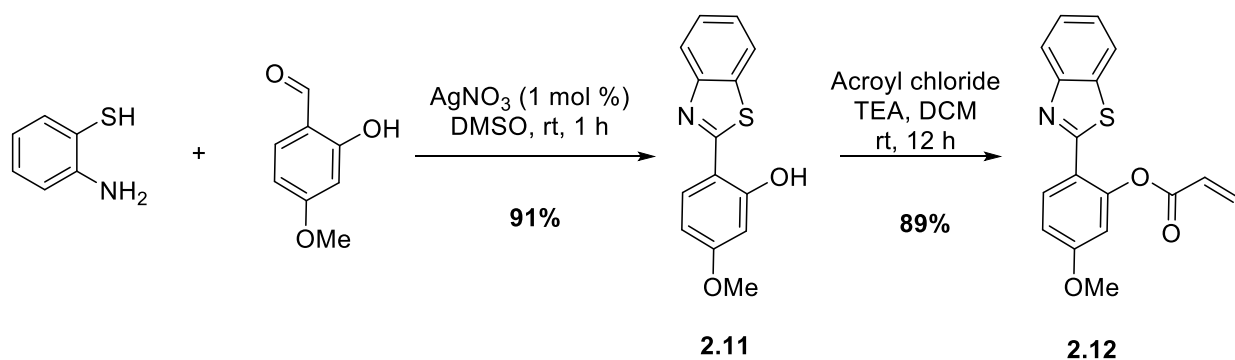
Scheme 2.1: Original synthesis of oxo-thiazepine VU0544412 analogs from L-cysteine and methyl acrylate.

While little is reported in the literature in regard to substituted 1,4-thiazepines as biological probes, there are several works that report our desired core as a byproduct of a fluorescent cysteine detection system.⁹⁴⁻⁹⁶ We hypothesized that we could use this system to readily access the oxo-thiazepine quickly, and in high yields. Using the fluorescent probe 2-(2'-hydroxy-4'-methoxyphenyl)benzothiazole (HMBT), masked with an α,β -unsaturated carbonyl moiety, we could achieve the desired conjugate addition upon addition of cysteine. The ensuing intramolecular cyclization reaction would occur with the HMBT ester. This would provide the (*R*)-5-oxo-1,4-thiazepane-3-carboxylic acid and the fluorescent probe HMBT, which could be recovered and reused (**Scheme 2.2**).



Scheme 2.2: Improved synthesis of the oxo-thiazepine from L-cysteine and masked HMBT **2.10**.

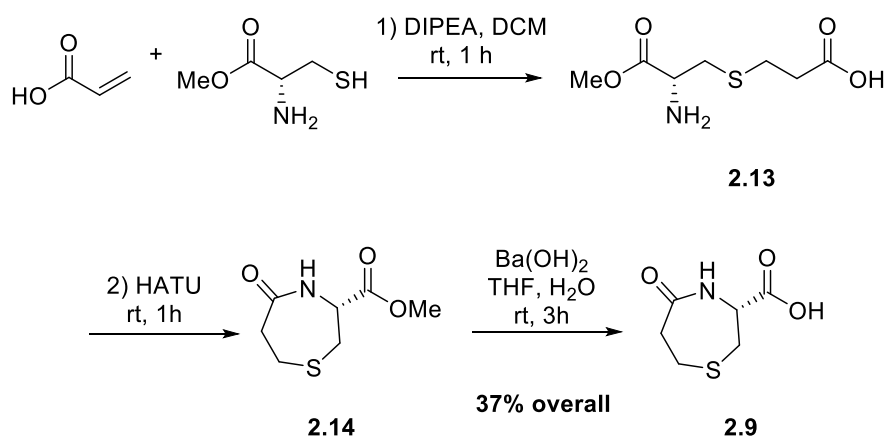
Synthesis of HMBT occurred via a condensation/intramolecular nucleophilic addition/oxidation process between 2-hydroxy-4-methoxybenzaldehyde and 2-aminothiophenol (**Scheme 2.3**) catalyzed by silver nitrate.⁹⁷ HMBT was then subjected to esterification conditions with acryloyl chloride and base. The desired electrophilic probe (**2.10**) was isolated in excellent yield with little difficulty. We then set to establish conditions to facilitate the chemistry proposed in **Scheme 2.2** for synthetic needs rather than cysteine detection in an aqueous biological system.



Scheme 2.3: Synthetic route to access HMBT (**2.11**) and the masked HMBT ester (**2.10**) from aminothiophenol and 2-hydroxy-4-methoxybenzaldehyde.

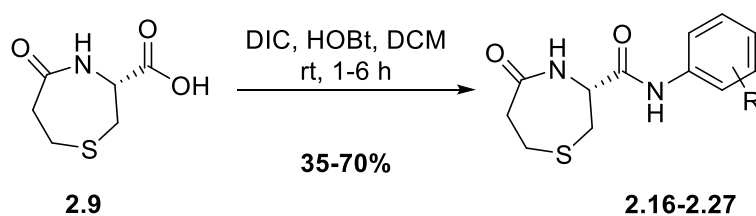
The conditions reported in the original disclosure did not repeat well in our hands.⁹⁸ With an aqueous reaction medium, the conjugated addition of cysteine onto the HMBT ester was monitored by LCMS and occurred quickly. Upon the addition of base, we saw hydrolysis of the ester to yield HMBT and the Michael adduct without the formation of the cyclized product. The use of DCM as the solvent provided the oxo-thiazepine in good yields and prevented HMBT ester hydrolysis by solvent water.

Further, it was envisioned that the same strategy used in **Scheme 2.1** could be altered to improve yields, shorten reaction time, and with fewer steps. First, Michael addition of methyl L-cysteinate onto acrylic acid using diisopropylethylamine as a base gave the Michael adduct (**2.13**) in good yields. HATU was then added portion-wise to facilitate cyclization. The crude methyl ester **2.14**, was carried forward and subjected to gentle saponification conditions with barium hydroxide to prevent racemization. Pure oxo-thiazepine (**2.9**) was isolated with acid-base work up conditions. This route provides **2.9** quickly and efficiently, in 37% yield over 3 steps, should the use of our improved route be inaccessible.



Scheme 2.4: Modified synthesis from **Scheme 2.1** to access oxo-thiazepine methyl L-cysteinate and acrylic acid.

Finally, we moved to explore conditions to improve the yield of the final amide coupling. We believed the low yields reported in Dr. Fulton's original scheme were due to the aniline coupling partners being weak nucleophiles. Several amide coupling conditions were screened that would avoid racemization and produce better yields (mixed anhydrides, DIC, DCC, EDC, Phosphonium reagents, Aminium/Uronium-Imonium Reagents, T3P, CDI). DIC proved to be the best coupling agent when paired with the racemization inhibitor HOBt (**Scheme 2.5**). Fortunately, DIU was not an issue during purification using reverse phase purification techniques and allowed us to generate analogs quickly and with improved yields.



Scheme 2.5: Optimized amide coupling conditions to generate final compounds **2.15-2.26**.

SAR of the arene ring: analogues 2.15-2.29

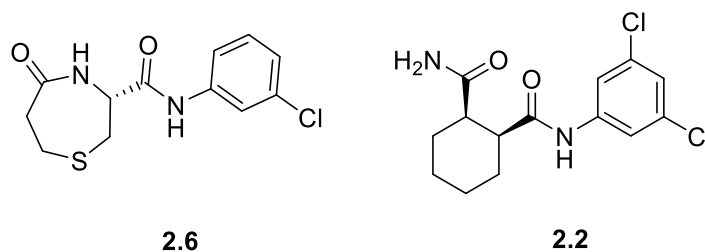


Figure 2.4: Comparison of the oxo-thiazepine scaffold and Lundbeck's candidate, **2.2**.

Considering the similarity between our oxo-thiazepine scaffold (**2.7**) and Lundbeck's clinical candidate (**2.2**, **Figure 2.4**), we set out to explore dihaloamide derivatives. All possible combinations of 3,5-dihaloamides were tested to determine what the ideal combination of halogen substitutions was for mGlu₄ activity. Additionally, 3,5 halogen isosteres (-Me, -CF₃, -OCF₃) substituted analogs, were synthesized to further confirm that halogen bonding is occurring. These data are shown in **Table 2.1**, below. As can be seen with analogs **2.20** and **2.21**, addition of a bromine to the arene ring resulted in a considerable increase in potency, with both the 3-bromo-5-chloro and 3,5-dibromo analogs resulting in compounds that were in the low nanomolar range. The 3,5-bis(trifluoromethyl) analog **2.26**, proved to maintain modest activity at mGlu₄, but confirms that halogen bonding interactions drive the potency observed with **2.20** and **2.21**.

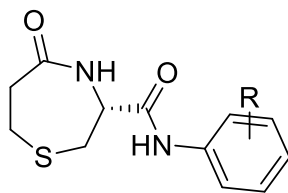


Table 2.1: 3,5-substituted analogs were explored to identify the halogen-bonding hypothesis in potency and efficacy, and to better understand the trends in this series. Associated potency and efficacy data from 10-point CRC-format screen at rat mGlu4 GIRK cell lines. Activities for each compound are reported as a percentage of the maximum response. VU number denotes the compound identifier assigned by Vanderbilt University. Data represent the mean of at least 3 replicate experiments with similar results.

R	VOID	Cmpd No	mGlu₄ EC₅₀ (nM)	mGlu₄ %Glu Max
3,5-F	VU6023806	2.15	8,920	102
3-Cl, 5-F	VU6023811	2.16	278	112
3-Br, 5-F	VU6023808	2.17	351	101
3-I, 5-F	VU6023809	2.18	558	102
3,5-Cl	VU6015338	2.19	273	88
3-Br, 5-Cl	VU6022296	2.20	32.8	108

3,5-Br	VU6023810	2.21	35.3	97
3-I, 5-Br	VU6023812	2.22	115	101
3,5-Me	VU6044298	2.23	11,900	NA
3-Cl, 5-Me	VU6044297	2.24	1,090	87
3-Br, 5-OCF ₃	VU6044296	2.25	2,660	22
3,5-CF ₃	VU6044303	2.26	951	102

Halogen bonding tracks well with the observed SAR trends. Halogen bonding is a phenomenon where lone pairs on a heteroatom interact with and stabilize the σ^* orbital of the halogen-carbon bond on the arene. This LUMO becomes lower in energy as the halogen size increases and the bonds get longer and weaker, thus iodine analogues should prove to be ideal. However, the iodo-analogs **2.18** and **2.22** exhibit a loss of activity compared to the chloro- and bromo-analogs, but could be explained by the fact that the iodine atom is susceptible to means of decomposition, and could disrupt favorable interactions with the protein through the introduction of steric clash due to its size.

Moving forward with the two most potent 3,5-dihaloamides, the opposite enantiomer was synthesized. Using the improved synthetic route with D-cysteine, we quickly accessed **2.27-2.29**. Unfortunately, activity at mGlu₄ proved to be enantioselective, with **2.28** and **2.29** being 2-fold less potent. Thus, we chose to explore the importance of the oxo-thiazepine core.

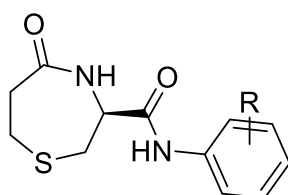


Table 2.2: The opposite enantiomer of lead compounds 2.21 and 2.22 was investigated to see if binding at mGlu₄ was stereospecific. Associated potency and efficacy data from 10-point CRC-format screen at rat mGlu₄ GIRK cell lines. Activities for each compound are reported as a percentage of the maximum response. VU number denotes the compound identifier assigned by Vanderbilt University. Data represent the mean of at least 3 replicate experiments with similar results.

R	VUID	Cmpd No	mGlu ₄ EC ₅₀ (nM)	mGlu ₄ %Glu Max
3-Br	VU6044301	2.27	Inactive	NA
3,5-Br	VU6044302	2.28	64.1	98
3-Br, 5-Cl	VU6044304	2.29	75.9	104

Evaluating the Importance of the Oxo-thiazepine Core

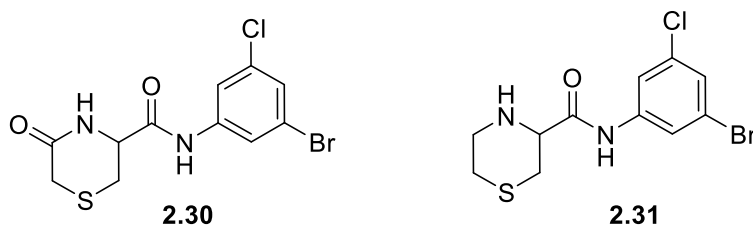


Figure 2.5: Thiomorpholine derivatives **2.30** and **2.31**.

No modification of the oxo-thiazepine core had been previously explored, thus we chose to assess thiomorpholine derivatives. This was less of an attempt improve potency, but to improve synthetic accessibility and remove the amino-acid like nature of the series. The orientation of the two amides within this chemotype are peptide-like, which indicates it could be a substrate of P-glycoprotein (PGP) transporters.⁹⁹ PGP transporters in the BBB plays a large role in keeping substrates out of the brain, and might be responsible for the lack of brain penetrance associated with this scaffold, particularly **2.6**. Unfortunately, both **2.30** and **2.31** proved to be inactive and is indicative that the thiazepine core is crucial to activity.

Assessment of VU0622296 (2.20) as a Viable Tool Compound

Considering the potency of **2.20** and **2.21** at mGlu₄, we chose to consider them as tool compounds. The addition of a halogen on the arene ring of **2.7** resulted in in a 4-fold increase in potency and notably changed the predicted cLogP. For several classes of CNS active substances, Hansch and Leo found that BBB penetration is optimal when the cLogP values are in the range of 1.5-2.7, with the mean value of 2.1.¹⁰⁰ While all analogs considered are technically 'drug-like' (cLogP <3, MW <400, tPSA <75), the

improvement in cLogP seen with **2.20** and **2.21** is closer to the ideal cLogP for brain penetration (cLogP 2.1).³⁵ *In vitro* and *in vivo* DMPK confirmed that the improvement in cLogP resulted in better brain penetration, with **2.20** having a $K_{p,uu}$ approaching unity.

Property	2.7	2.21	2.20
MW	284.77	408.12	363.65
cLogP	1.52	2.41	2.28
tPSA	58.1	58.4	58.2
<i>Pharmacokinetic parameters</i>			
CL _{INT} (mL/min/kg), rat		416	343
CL _{HEP} (mL/min/kg), rat	63.6	59.9	58.1
CL _{INT} (mL/min/kg), human		31	34.5
CL _{HEP} (mL/min/kg), human	9.4	12.5	13.1
PPB (f _u), rat		0.011	0.018
PPB (f _u), human		0.007	0.011
BHB (f _u), rat		0.006	0.028
<i>Tissue distribution</i>			
C _n plasma (ng/mL)		122	93.8
C _n brain (ng/mL)	BLQ	22.6	42.1
K _p , brain		0.19	0.45
K _{p,uu} brain		0.10	0.70

Table 2.3: *In vitro* and *in vivo* DMPK parameters for lead compounds **2.20** and **2.21**, compared to the original lead **2.7**.

However, **2.20** and **2.21** did not improve the scaffold's clearance issues (**Table 2.3**). The 3-bromo, 5-chloro analog (**2.20**) was moderately cleared in human (13.1 mL/min/kg), but highly cleared in rat (58.1 mL/min/kg). While clearance proves to be an issue for our animal behavioral models, first pass metabolism can be avoided via routes of administration. Thus, **2.20** was scaled up for evaluation in a haloperidol-induced catalepsy.

Haloperidol administration to mice induces a well-described condition of immobility characterized by muscle rigidity and frozen posture. This condition in mice resembles similar human conditions in disorders such as Parkinson's disease.¹⁰¹ The reversal of this phenotype with mGlu₄ PAMs is established by our group, and represents an excellent way to confirm anti-PD effects as a result of mGlu₄ activity.^{90, 102} Compound **2.20** reversed the haloperidol-induced PD phenotype in a dose-dependent manner with a mean effective dose (MED) of 10 mg/kg (**Figure 2.6**), and stands to be a viable mGlu₄ PAM tool compound.

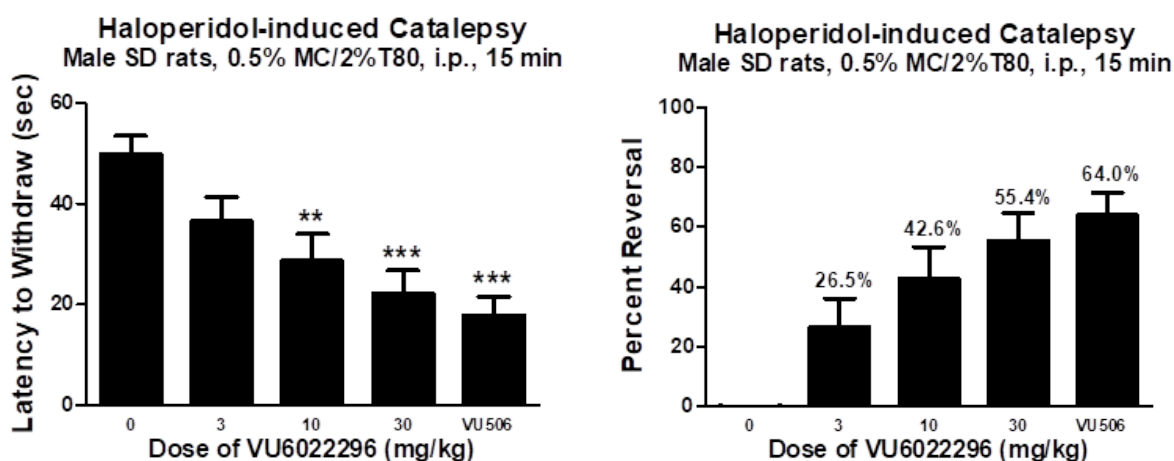


Figure 2.6: VU6022296 (**2.20**) exhibits anti-PD activity in reversing haloperidol-induced catalepsy with a MED of 10 mgs/kg in male Sprague-Dawley rats.

Summary and Future Directions

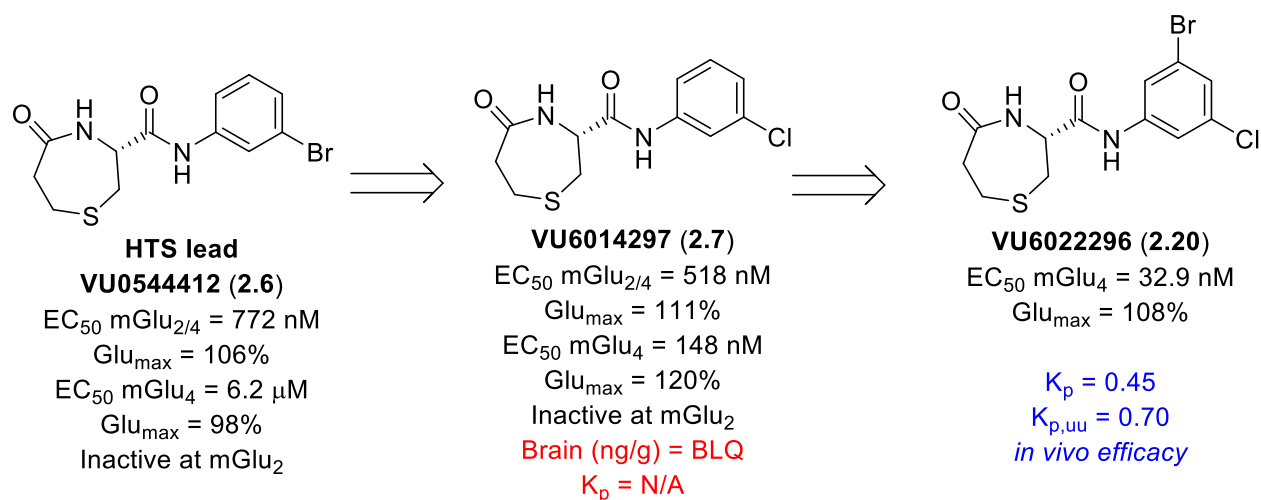


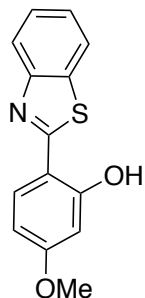
Figure 2.7: Summary of SAR that lead to the discovery of **2.20**.

In conclusion, we have identified a new mGlu_4 PAM tool compound containing a previously unexplored chemotype, and a novel route for its synthesis. This tool compound, **2.20** (Figure 2.7), was developed from a micromolar HTS lead to be a potent, brain-penetrant mGlu_4 PAM with *in vivo* efficacy. While this scaffold suffers from high hepatic clearance in rats, this can be overcome with routes of administration for *in vivo* animal studies. In collaboration with the Rook lab, we were able to show that **2.20** shows anti-PD efficacy as an *in vivo* tool compound in HIC animal models that correlates with compound exposure. We hope that with the development of novel mGlu_4 selective PAM chemotypes, we can further elucidate the physiological role of mGlu_4 in PD and other relevant disease states. Such basic science studies will be crucial to push other mGlu_4 PAMs into the clinic.

Experimental Methods

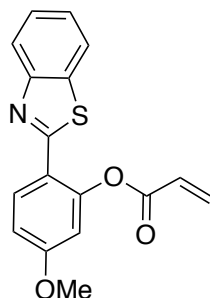
General Synthetic Methods and Instrumentation

Unless otherwise stated, all reactions were conducted in flame-dried or oven-dried glassware under inert atmospheres of argon. All commercially available reagents and reaction solvents were used as received, unless otherwise noted. Thin layer chromatography (TLC) was performed on glass-backed silica of 250 μM thickness. Visualization was accomplished with UV light and/or the use of bromocresol green stain. Chromatography on silica gel was performed using Teledyne ISCO pre-packed silica gel columns using gradients of EtOAc/hexanes. ^1H and ^{13}C chemical shifts are reported in δ values in ppm downfield with the deuterated solvent as the internal standard. Data are reported as follows: chemical shift, multiplicity (s = singlet, d = doublet, t = triplet, q = quartet, b = broad, m = multiplet), integration, coupling constant (Hz). Low resolution mass spectra were obtained on an Agilent 6120 or 6150 with ESI source. MS parameters were as follows: fragmentor: 70, capillary voltage: 3000 V, nebulizer pressure: 30 psig, drying gas flow: 13 L/min, drying gas temperature: 350 $^\circ\text{C}$. Samples were introduced via an Agilent 1290 UHPLC comprised of a G4220A binary pump, G4226A ALS, G1316C TCC, and G4212A DAD with ULD flow cell. UV absorption was generally observed at 215 nm and 254 nm with a 4 nm bandwidth. Column: Waters Acquity BEH C18, 1.0 x 50 mm, 1.7 μm . Gradient conditions: 5% to 95% ME CN in H₂O (0.1% TFA) over 1.4 min, hold at 95% ME CN for 0.1 min, 0.5 mL/min, 55 $^\circ\text{C}$. All reagents were purchased from Aldrich Chemical Co. and were used without purification. Sure-Seal solvents were purchased from Sigma Aldrich.



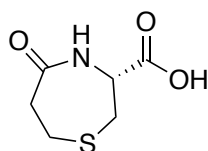
2-(benzo[d]thiazol-2-yl)-5-methoxyphenol (2.12).

To a solution of 2-hydroxy-4-methoxybenzaldehyde (1 mmol), 2-aminobenzenethiol (1 mmol) and AgNO_3 (0.01 mmol) in DMSO (3 mL) were added and the resulting mixture was stirred at rt for 4 h. The mixture was diluted with DCM, and washed with an excess of brine thrice. Organic layers were combined, dried over MgSO_4 , filtered and concentrated under reduced pressure. Purification of the residue by flash chromatography (hexanes/EtOAc = 3:2) afforded 246 mg of the desired benzothiazole as a white solid in 96% yield. $^1\text{H NMR}$ (400 MHz, MeOD) δ 8.00 – 7.90 (m, 2H), 7.75 – 7.67 (m, 1H), 7.51 (ddd, J = 8.3, 7.2, 1.3 Hz, 1H), 7.40 (ddd, J = 8.3, 7.3, 1.2 Hz, 1H), 6.62 – 6.54 (m, 2H), 3.85 (s, 3H). $^{13}\text{C NMR}$ (101 MHz, MeOD) δ 169.00, 163.76, 159.48, 151.85, 132.33, 129.47, 126.38, 124.90, 121.27, 121.14, 110.25, 107.05, 100.93, 54.59. LC-MS [$m/z+H$] = 312.5. Analytical data are in accordance with the literature.



2-(benzo[d]thiazol-2-yl)-5-methoxyphenyl acrylate (**2.13**).

To a solution of HMBT **2.12** (0.5 mmol) and Et₃N (2 eq) in DCM (10 mL), acryloyl chloride (1.25 eq, mixed with 4 mL of DCM) was added dropwise at 0 °C. After stirring at 90 min, the mixture was warmed to rt and stirred overnight. The solution was diluted with DCM (30 mL), washed with H₂O thrice, dried over anhydrous MgSO₄ and concentrated under reduced pressure. The crude mixture afforded **2.13** upon crystallization from hexanes/CHCl₃ (20:1) as a pale yellow solid (110 mg, 71% yield). **¹H NMR (400 MHz, CDCl₃)** δ 8.00 – 7.90 (m, 2H), 7.75 – 7.67 (m, 1H), 7.51 (ddd, *J* = 8.3, 7.2, 1.3 Hz, 1H), 7.40 (ddd, *J* = 8.3, 7.3, 1.2 Hz, 1H), 6.62 – 6.54 (m, 2H), 3.85 (s, 3H). **¹³C NMR (101 MHz, CDCl₃)** δ 149.60, 133.89, 131.52, 131.45, 127.72, 127.68, 126.70, 126.58, 125.40, 125.29, 122.43, 122.31, 121.22, 112.90, 108.87, 55.76, 55.73. **LC-MS [m/z+H]** = 312.5. Analytical data are in accordance with the literature.

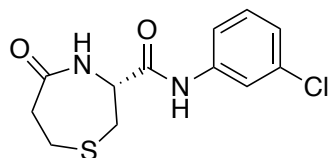


(*R*)-5-oxo-1,4-thiazepane-3-carboxylic acid (**2.8**).

To a 100 mL flask, **2.13** (0.3 mmol) and L-cysteine (0.375 mmol, 1.25 eq) were combined in 3 mL of DCM, and the mixture stirred at rt for 2 h. Then, Et₃N (80 μL) was

added and the solution stirred for 40 min. The reaction mixture under reduced pressure and the crude solid was subjected to column chromatography to afford 75 mg of HMBT **2.12** and 39 mg of **2.8** as an off-white solid. $^1\text{H NMR}$ (400 MHz, MeOD) δ 4.54 (dd, $J = 8.1, 2.0$ Hz, 1H), 3.10 (dd, $J = 14.5, 2.0$ Hz, 1H), 3.01 – 2.83 (m, 3H), 2.78 – 2.69 (m, 2H). $^{13}\text{C NMR}$ (101 MHz, MeOD) δ 177.15, 170.87, 57.53, 40.65, 33.48, 23.70. LC-MS $[\text{m/z}+\text{H}] = 176.3$. Analytical data are in accordance with the literature.

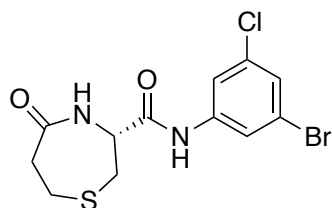
General Synthesis for Benzamides: To a solution of aniline (1.0 eq) in DCM (0.1 M), was added (*R*)-5-oxo-1,4-thiazepane-3-carboxylic acid (1.0 eq), HOBT (1.5 eq), and DIC (1.2 eq) at rt. Reaction progress was monitored by TLC and upon completion, the reaction mixture was washed with water, concentrated, and redissolved in DMSO. The urea by product of DIC is poorly soluble in DMSO and will crash out of solution after 15 min. Crude DMSO solutions were filtered of the solid DIU byproduct and purified using a Gilson HPLC system (30 x 50 mm column; H₂O with 0.1% TFA:acetonitrile). Fractions containing the desired product were quenched with saturated NaHCO₃, extracted with 4:1 CHCl₃:IPA, and concentrated to isolate the pure product.



(*R*)-*N*-(3-chlorophenyl)-5-oxo-1,4-thiazepane-3-carboxamide (2.7).

This compound was synthesized according to general procedure and isolated as a white solid, 62% yield. $^1\text{HNMR}$ (400 MHz, DMSO) δ 10.40 (s, 1H), 7.80 (t, $J = 2.0$ Hz,

1H), 7.48-7.44 (m, 1H), 7.36 (t, J = 8.0 Hz, 1H), 7.17-7.13 (m, 1H), 7.13-7.09 (m, 1H), 4.54-4.48 (m, 1H), 3.03 (dd, J = 14.4, 2.2 Hz, 1H), 2.95 (dd, J = 14.4, 8.2 Hz, 1H), 2.90-2.73 (m, 3H), 2.72-2.68 (m, 2H); ¹³CNMR (101 MHz, DMSO) δ 174.3, 168.1, 134.0, 133.1, 130.1, 123.5, 119.1, 118.0, 57.8, 40.3, 33.9, 23.5. LC-MS [m/z+H] = 285.5.



(R)-N-(3-bromo-5-chlorophenyl)-5-oxo-1,4-thiazepane-3-carboxamide (2.20): This compound was synthesized according to general procedure and isolated as a white solid, 37% yield. ¹H NMR (400 MHz, DMSO) δ 10.50 (s, 1H), 7.81 (t, J = 1.8 Hz, 1H), 7.72 (t, J = 1.9 Hz, 1H), 7.45 (t, J = 1.8 Hz, 1H), 7.19 (d, J = 6.7 Hz, 1H), 4.50 (ddd, J = 8.0, 6.6, 2.5 Hz, 1H), 3.04 (dd, J = 14.5, 2.5 Hz, 1H), 2.97 (dd, J = 14.5, 8.0 Hz, 1H), 2.90 – 2.74 (m, 2H), 2.70 (td, J = 4.9, 2.4 Hz, 2H). ¹³C NMR (101 MHz, DMSO) δ 174.77, 168.82, 141.41, 126.05, 122.54, 121.02, 118.53, 58.22, 40.79, 34.09, 23.88. LC-MS [m/z+H] = 362.9.

CHAPTER III

PROGRESS TOWARDS THE TOTAL SYNTHESIS OF THIOCLADOSPOLIDE A

Background and Introduction

Natural Products in Antibiotic Drug Discovery

Historically, natural products have been one of the most consistently productive sources for the development of new drugs.¹⁰³ Before the advent of more high-throughput techniques, more than 80% of drug and drug products were natural products or derived from one.¹⁰⁴ This class of drugs includes compounds from plants, microbes, and animals, in addition to semi-synthetic derivatives of such, that vary from anti-cancer, anti-effective, and anti-diabetic indications.¹⁰³ The use of natural products as a source has diminished in the past two decades as they suffer from several disadvantages: (1) difficulties with access and limited supply (2) complexities of synthesis, (3) inherent slowness in screening and development, and (4) concerns surrounding the rights to intellectual property.¹⁰⁵

However, nearly after a century of unchecked usage of antibiotics since their discovery have led to the emergence of antibiotic-resistant strains of bacteria.^{106, 107} Scientists have now warned for decades the emergence of antibiotic resistance will be one of the greatest public health threats in the coming decades.¹⁰⁸ As the threat of antibiotic resistance grows without the discovery of new therapeutic agents, the world's current antibiotic supply will quickly become irrelevant.¹⁰⁶ Modern combinatorial approaches have not yielded effective antibiotic drugs and research efforts are returning to the use of natural products with proven efficacy.¹⁰⁵

A viable approach for new antibiotic discovery is through bacterial and fungal co-culture.¹⁰⁹ It has been shown that “crosstalk” between microorganisms can activate silent gene clusters that lead to novel secondary metabolites with potent biological activities.¹¹⁰ Most secondary metabolites can be grouped into three chemical categories: polyketides derived from acyl-CoAs, terpenes derived from acyl-CoAs and small peptides derived from amino acids.¹¹⁰ To create protective and weaponized natural products, secondary metabolism typically occurs in instances of stress.¹¹¹ This class of molecules have natural antibiotic activities to help fungi remain competitive in highly competitive ecological systems. In fact, the magnitude of biosynthetic genes within fungal genomes suggest that fungal secondary metabolite natural products are a largely untapped resource for drug discovery.¹¹²

Sulfur-containing Macrolides and the Discovery of the Thiocladosporides

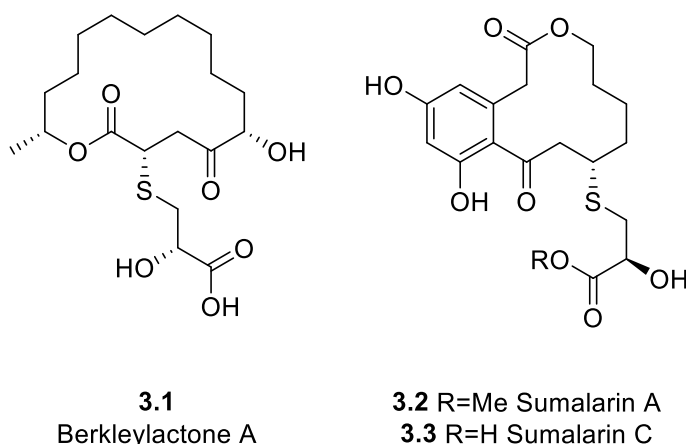


Figure 3.1: Structures of thio-adduct natural products Berkleylactone A and Sumalarins A and C.

A small class of potent, biologically relevant natural products are sulfur-containing metabolites from fungal sources. These compounds are frequently isolated

from marine organisms as sulfur-containing molecules, including cysteine, are abundant in seawater. Isolated sulfur containing metabolites like Berkleylactone A (**3.1**) and the Sumalarians A-C (**3.2** and **3.3**), have established antibiotic activity against antibiotic-resistant strains, in addition to other anti-inflammatory and anticancer activities (**Figure 3.1**).^{113, 114} These interesting marine natural products carry the potential to be novel antibiotics that address the predicted influx of hospital-acquired antibiotic-resistant infections in the coming decades.

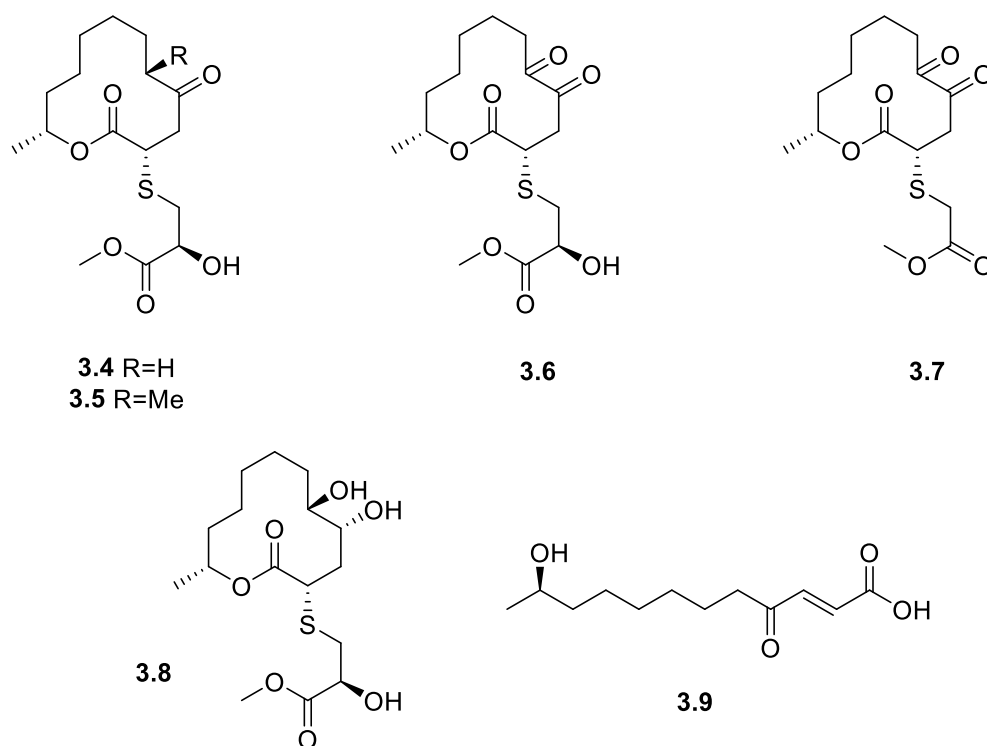


Figure 3.2: Structures of Thiocladospolides A **3.4**, B **3.6**, C **3.7**, D **3.8**, known Pandangolide **3.5**, and the hydrolysis product **3.9**.

As part of the continuing research on discovery of marine natural products with potent biological activities, the EtOAc-soluble media extract of the mangrove-derived fungal strain *Cladosporium cladosporioides* (MA-299) provided four new sulfur-

containing 12-membered macrolides, thiocladospolides A–D (**3.4**, **3.6**, **3.7**, **3.8**), each having a sulfur substitution at C-2 (**Figure 3.2**). Thiocladospolides A-D were isolated together with the related known analogue Pandangolide 3 (**3.5**) and the possible hydrolysis product (**3.9**), and were surveyed for biological activity.^{115, 116}

Table 3.1: Reported Antimicrobial Activities of Compounds **3.4**, **3.6**, **3.7**, **3.8** and **3.9** (MIC, $\mu\text{g/mL}$)^{a,116}

Strain	Compound No					Positive control
	3.4	3.6	3.7	3.8	3.9	
<i>E. tarda</i> ^b	1	–	–	–	–	0.5
<i>E. ictarda</i> ^b	8	–	–	1	–	0.5
<i>C. glecosporioides</i> ^c	2	2	1	1	2	0.5
<i>B. sorokiniana</i> ^c	–	–	–	–	8	0.5
<i>P. piricola</i> Nose ^c	–	32	32	32	–	2.0
<i>F. oxysporum f. sp. cucumerinum</i> ^c	–	1	32	1	–	0.5

^a(–) = MIC > 32 $\mu\text{g/mL}$.

^bChloramphenicol as positive control.

^cAmphotericin B as positive control.

The antimicrobial activities of **3.4**, **3.6**, **3.7**, **3.8** and **3.9** against 10 aquatic pathogens and one human pathogenic bacterium as well as 15 plant pathogenic fungi were tested. All tested compounds displayed activity against the plant pathogen *Colletotrichum glecosporioides* with MIC values of 1 or 2 $\mu\text{g/mL}$ (**Table 3.1**).¹¹⁶ Compounds **3.4** and **3.6** showed potent inhibitory activity against the aquatic pathogens *Edwardsiella tarda* and *E. ictarda*, respectively, each with an MIC value of 1 $\mu\text{g/mL}$, while compounds **3.6** and **3.8** demonstrated activities against *Fusarium oxysporum f.*

sp. cucumerinum, each with MIC values of 1 µg/mL. The closely related Pandangolides 2, 3, and 4 are known to be inactive against other Gram-positive and Gram-negative bacteria. While the thiocladospolides and similar compounds such as Berkeleylactone A exhibit activity against Gram-positive and Gram-negative bacteria.¹¹⁶ The above data indicates that sulfur substitution may drive the potent antibiotic nature of these macrolides.

Sulfur-substituted macrolides are likely fungal biotransformation products resulting from the long cultivation time or detoxification products under stressful environmental conditions. It is easy to envision that the thiocladospolides are 1,4 thiomichael adducts of patulolide A (**3.10**) with a cysteine derivative (**3.11**, **Figure 3.3**). While these small molecules are potent antibiotics, their extraction from their fungal source is costly and difficult (~8mg/100L over 50 days). Considering the potential therapeutic potential, attractive molecular structure, and lack of existing syntheses, a concise synthesis of the Thiocladospolide A has been planned.

A Failed Synthetic Route to Thiocladospolide A

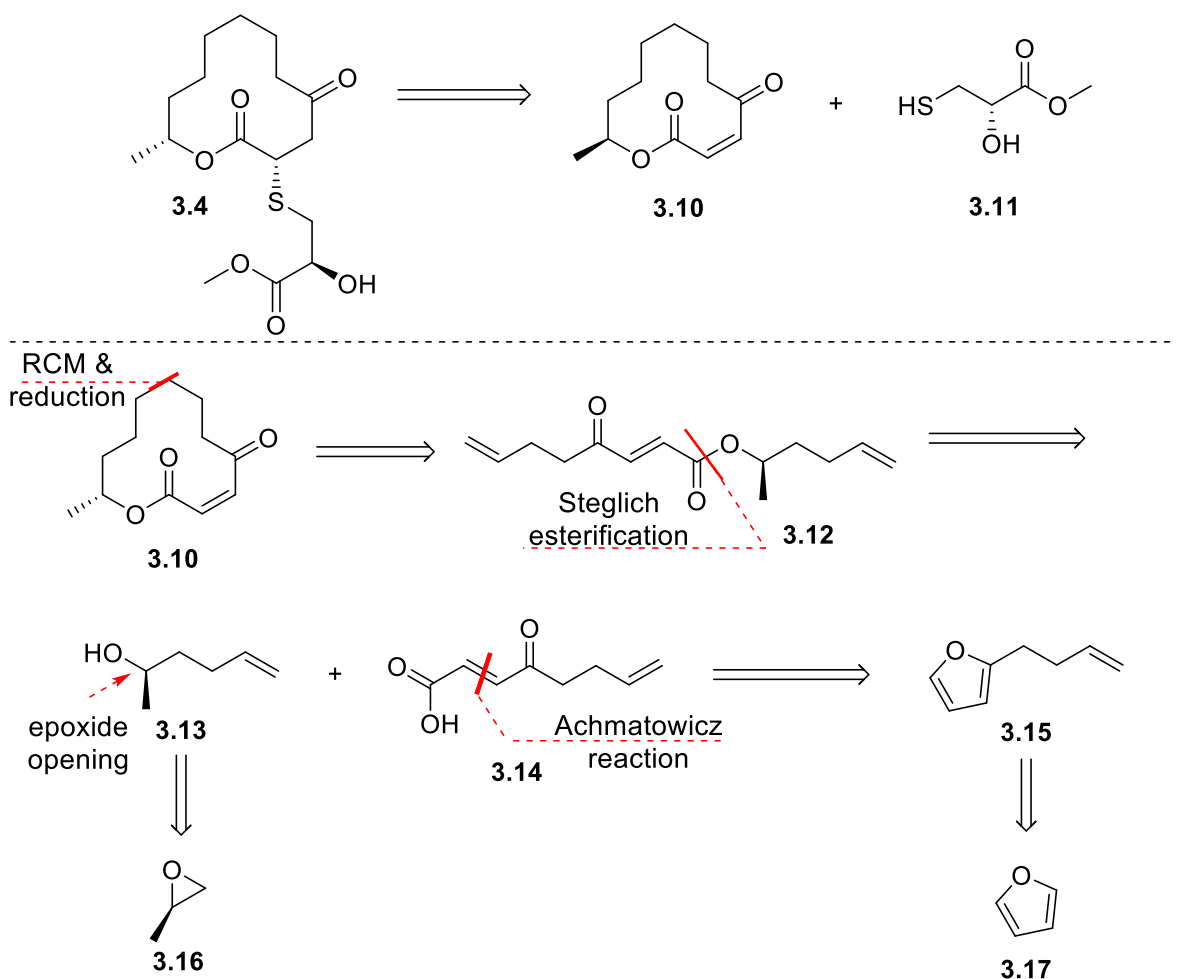
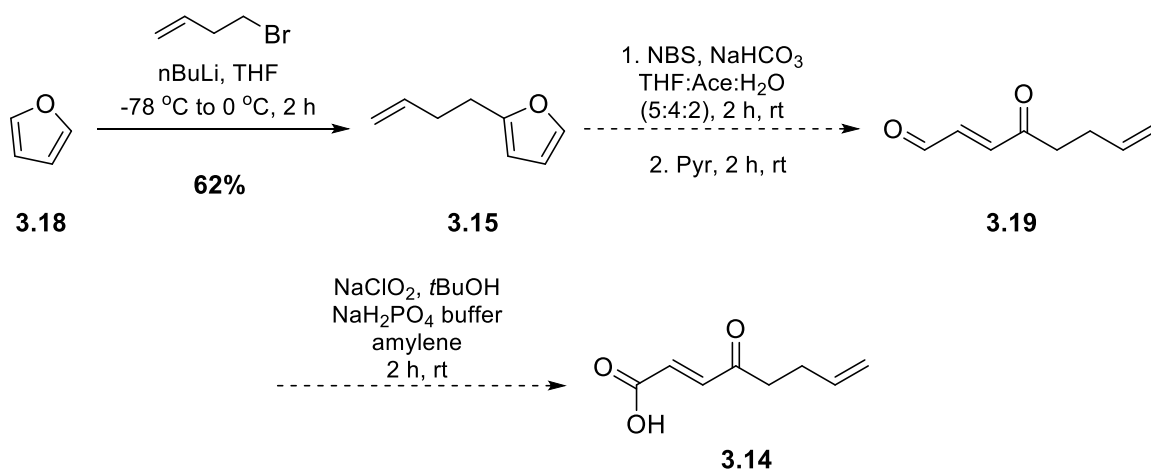


Figure 3.3: Retrosynthetic analysis of Thiocladospolide A.

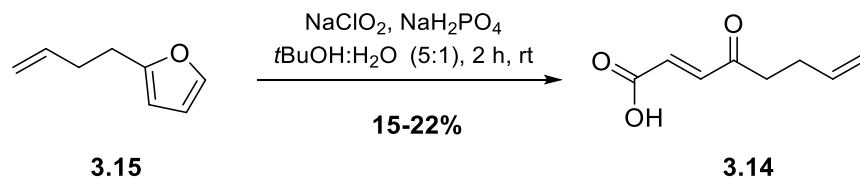
The retrosynthesis was planned in an effort to be synthetically different than published syntheses of closely-related patulolide A, prioritizing yield, step-count, and accessibility to unnatural analogs (**Figure 3.3**).¹¹⁷⁻¹²⁰ Our synthetic plan was dependent on a final, diastereoselective sulfa-Michael addition, in which the macrolide substrate controls the formation of the stereogenic center at C-2.^{113, 121} Formation of the 12-membered macrocyclic lactone should be accessed one-pot via a ring closing

metathesis (RCM) followed by chemoselective reduction of the non-conjugated double bond.¹²² The necessary linear diene **3.12**, could be accessed via an esterification between enantiopure hexenol **3.13** and 4-oxo-2-alkeneoic acid **3.14**.¹²³ It is easy to envision how (*R*)-2-methyloxirane could be opened with allylmagnesium bromide to yield the desired alcohol **3.13**.¹²⁴ Our synthetic efforts began with the synthesis of **3.14** via a furan oxidation strategy.



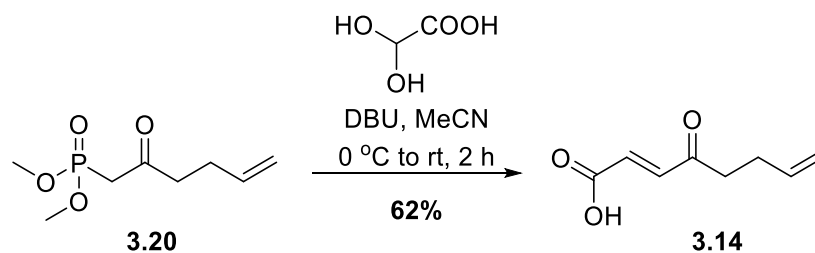
Scheme 3.1: Furan oxidation strategy via Achmatowicz chemistry to yield 4-oxo-2-alkeneoic acid **3.14**.

Freshly distilled furan was subjected to basic conditions with 4-bromobutene to give alkyl furan **3.15** in moderate yields. Conversion of the 2-substituted furan to the 4-oxo-2-alkenal was attempted using Achmatowicz reaction conditions.¹¹³ While starting material was consumed, the desired product was volatile and difficult to isolate. Additionally, several products formed, and proved to be an unfavorable approach. Thus, we attempted to develop a method in which we could directly oxidize the alkyl furan to the 4-oxo-2-alkeneoic acid, based on a literature procedure.¹²⁵



Scheme 3.2: Direct furan oxidation strategy to yield 4-oxo-2-alkeneic acid **3.14**.

Furan **3.15** was subjected to Pinnick oxidation-like conditions with sodium chlorite in slightly acidic media. This reaction proceeds through a 2-alkyl-2-hydroxybutenolide intermediate, a ring tautomer of 4-oxo-2-alkeneic acids. The published procedure detailed that stereoselective conversion of the alkyl butenolides intermediate into the 4-oxo-2(*E*)-alkeneic acid is accomplished with a catalytic amount of pyridine in 2 hours at room temperature.¹²⁵ However, with our substrate, we found that the reaction stalled at the butenolide and did not undergo ring opening even with excess pyridine, longer reaction times, and increased temperature.

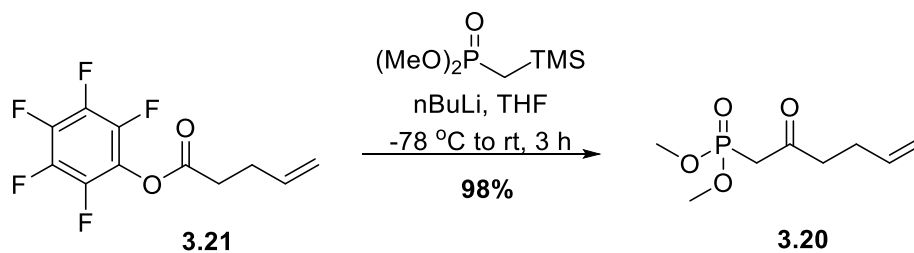


Scheme 3.3: Modified Horner-Wadsworth-Emmons with glyoxylic acid monohydrate generates 4-oxo-2-(*E*)alkeneic acids stereoselectively in excellent yields.

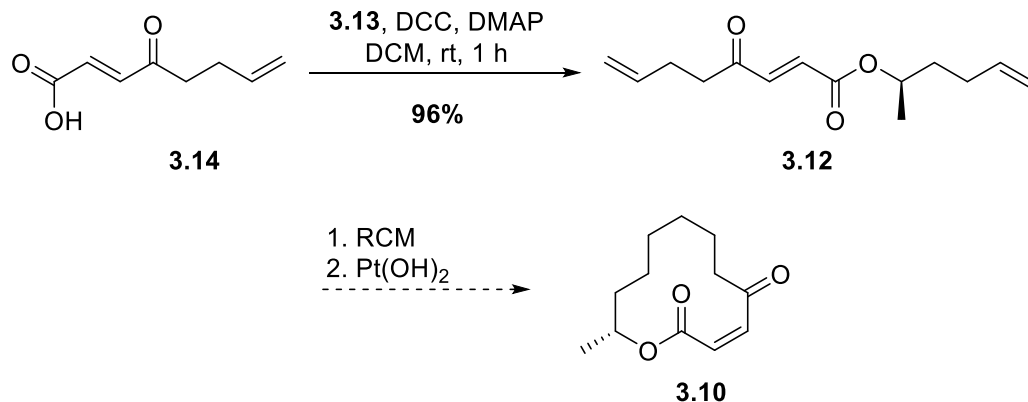
Abandoning our furan oxidation strategy, we then attempted to directly access the needed 4-oxo-2-alkeneic acids via a modified Horner-Wadsworth-Emmons (HWE) reaction with glyoxylic acid monohydrate and the corresponding β -ketophosphonate

(**Scheme 3.3**).¹²⁶ The β -ketophosphonate was obtained by generating the lithium anion of dimethyl methylphosphonate (DMMP) with *n*-BuLi followed by addition of commercially available benzyl 4-pentenoate in moderate yield. We were pleased to find that the β -ketophosphonate with a pre-dried solution of glyoxylic acid monohydrate smoothly converted to the 4-oxo-2(*E*)-alkenoic acid in excellent yields.

While we were excited to generate **3.14**, the above method generated the β -ketophosphonate **3.19** in moderate yields, with side products, and was difficult to purify from the excess DMMP. With room for improvement, we pursued an efficient and chemoselective method for the generation of β -ketophosphonates based on the Claisen condensation of the lithiated α -(trimethylsilyl)methylphosphonate with activated esters.¹²⁷ This reaction takes advantage of the α -effect of the silicon and the steric hindrance of the trimethylsilyl group, thereby increasing the chemoselectivity of the transformation. We found that using the pentafluorophenyl ester **3.20** with the mild lithiated phosphonate species seen in **Scheme 3.4**, we could access the β -ketophosphonate **3.19** in excellent yield.



Scheme 3.4: Improved generation of β -ketophosphonate **3.19** based on the Claisen condensation of lithiated α -(trimethylsilyl)methylphosphonate with our activated ester **3.20**.



Scheme 3.5: Steglich esterification conditions yielded **3.12**, which failed to undergo RCM.

With our desired electrophile in hand, opening of (*R*)-2-methyloxirane with allylmagnesium bromide yielded the desired alcohol **3.13** in excellent yield. Steglich esterification conditions provided diene **3.12** in high yields. However, we faced several challenges when attempting the RCM with **3.12**. Regardless of catalyst, reaction concentration, temperature, or length of reaction, we saw consumption of the starting material without formation of the desired product. We hypothesized that the final product was far too volatile to be able to deal with routinely for our desired medicinal chemistry efforts, and thus we abandoned our original synthetic route.

Conclusions and Future Directions

At this point, synthetic efforts have been offered to Jacob Kalbfleisch. A new synthetic route has been designed (**Figure 3.3**), that should prove to be successful based on successful preliminary experiments on model substrates, but have not been fully explored due to time restrictions. It is envisioned that using the activated ester **3.21** could undergo a cross metathesis with alcohol **3.13** to furnish **3.22**, inspired by

established chemistry with a similar substrate. Activated ester **3.20** could be readily converted to the oxo-alkenoic acid **3.9** with the chemistry disclosed previously. It is then envisioned that a stereoselective thio-Michael addition using the organocatalyst quinine would provide enantiopure thioether **3.23**, which would provide thiocladospolide A via macrolactonization conditions. Test reactions with a thionucleophile and linear ester **3.12** proved this approach provides the thioether readily, and can be stereocontrolled with the use of both quinine stereoisomers.¹²⁸ Protection strategies will likely be necessary to pursue this route, however, we believe this is the most robust route for the synthesis of Thiocladospolide A.

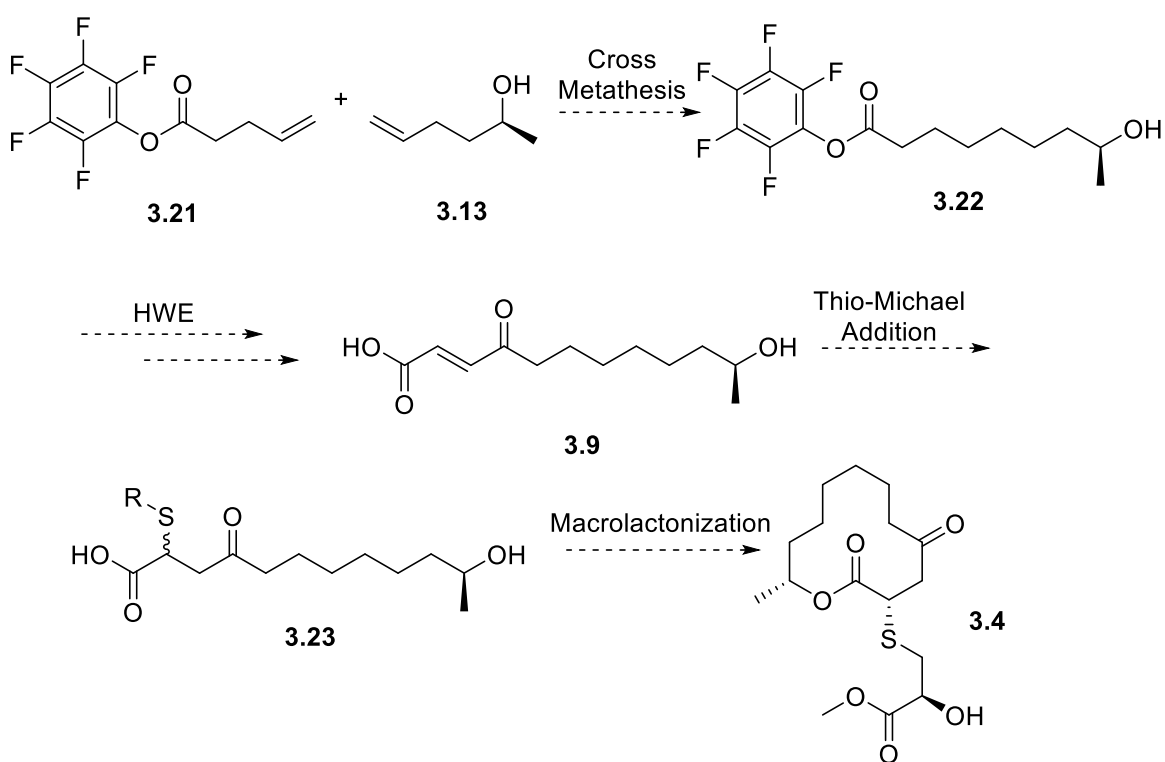
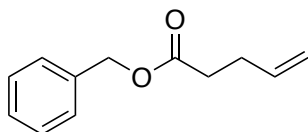


Figure 3.4: Proposed synthetic route to Thiocladospolide A **3.4**, which addresses previous challenges.

Experimental Methods

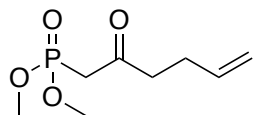
General Synthetic Methods and Instrumentation

Unless otherwise stated, all reactions were conducted in flame-dried or oven-dried glassware under inert atmospheres of argon. All commercially available reagents and reaction solvents were used as received, unless otherwise noted. Thin layer chromatography (TLC) was performed on glass-backed silica of 250 μM thickness. Visualization was accomplished with UV light and/or the use of bromocresol green stain. Chromatography on silica gel was performed using Teledyne ISCO pre-packed silica gel columns using gradients of EtOAc/hexanes. ^1H and ^{13}C chemical shifts are reported in δ values in ppm downfield with the deuterated solvent as the internal standard. Data are reported as follows: chemical shift, multiplicity (s = singlet, d = doublet, t = triplet, q = quartet, b = broad, m = multiplet), integration, coupling constant (Hz). Low resolution mass spectra were obtained on an Agilent 6120 or 6150 with ESI source. MS parameters were as follows: fragmentor: 70, capillary voltage: 3000 V, nebulizer pressure: 30 psig, drying gas flow: 13 L/min, drying gas temperature: 350 $^\circ\text{C}$. Samples were introduced via an Agilent 1290 UHPLC comprised of a G4220A binary pump, G4226A ALS, G1316C TCC, and G4212A DAD with ULD flow cell. UV absorption was generally observed at 215 nm and 254 nm with a 4 nm bandwidth. Column: Waters Acquity BEH C18, 1.0 x 50 mm, 1.7 μm . Gradient conditions: 5% to 95% MECN in H₂O (0.1% TFA) over 1.4 min, hold at 95% MECN for 0.1 min, 0.5 mL/min, 55 $^\circ\text{C}$. All reagents were purchased from Aldrich Chemical Co. and were used without purification. Sure-Seal solvents were purchased from Sigma Aldrich.



Synthesis of benzyl pent-4-enoate.

To a solution of pent-4-enoic acid (10.0 g, 99.9 mmol) and benzyl alcohol (14.1 g, 129 mmol, 1.3 equiv) in DCM (300 mL) at 0 °C were added DCC (30.7 g, 149 mmol, 1.5 equiv) and DMAP (61 mg, 19.8 mmol, 0.2 equiv). The mixture was stirred at rt for 1 h, after which a saturated solution of NH₄Cl was added. The mixture was extracted with EtOAc thrice, and the combined organic extracts were dried over MgSO₄, filtered, and concentrated under reduced pressure. Purification of the residue by flash chromatography (hexanes/EtOAc = 98:2) afforded of the desired ester as a clear oil in 82% yield. **¹H NMR (400 MHz, CDCl₃)** δ 5.86 (ddt, *J* = 16.5, 10.2, 6.2 Hz, 1H), 5.12 – 4.99 (m, 2H), 2.54 – 2.47 (m, 2H), 2.47 – 2.39 (m, 2H). **¹³C NMR (101 MHz, MeOD)** δ 172.97, 136.47, 136.16, 128.07, 127.77, 127.71, 114.48, 65.75, 33.00, 28.51. **R_f** = 0.9 (5% EtOAc/hexanes). Analytical data are in accordance with the literature.

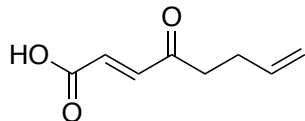


Synthesis of dimethyl (2-oxohex-5-en-1-yl)phosphonate (3.20).

Procedure 1: benzyl pent-4-enoate (0.6 g, 3.15 mmol) and dimethyl methylphosphonate (0.60 ml, 2.3 equiv, 5.6 mmol) in THF (30 ml) were added was

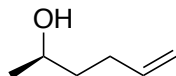
stirred and cooled to 0 °C (ice bath), and a freshly generated solution of LDA (1.42M in THF, 0.9 g, 7.3 mmol, 3.5 equiv) was added dropwise. The resulting mixture was stirred for 60 min at 0 °C, a saturated solution of NH₄Cl was added to quench, and the aqueous layer was extracted with DCM thrice. The combined organic extracts were dried over MgSO₄, filtered, and concentrated under reduced pressure. Purification of the residue by flash chromatography (hexanes/EtOAc = 4:1) afforded 629 mg of the desired phosphonate as a clear oil in 96% yield.

Procedure 2: To a solution of *n*-BuLi (2.6 mL, 2.5 M in hexanes, 6.6 mmol, 2.2 equiv) in THF (1.5 mL) at -78 °C was added α -(trimethylsilyl)methylphosphonate (750 μ L, 6.9 mmol, 2.3 equiv). After 30 min at -78 °C, a solution of activated ester (0.79 g, 3.0 mmol, 1 equiv) in THF (30 mL) was added dropwise. The reaction mixture was stirred for 30 min at -78 °C, and a saturated solution of NH₄Cl was added. The mixture was extracted with EtOAc, and the combined organic extracts were dried over MgSO₄, filtered, and concentrated under reduced pressure. Purification of the residue by flash chromatography (hexanes/EtOAc = 4:1) afforded 606 mg of the desired ester as a clear oil in 98% yield. **¹H NMR (400 MHz, CDCl₃)** δ 5.81 (ddt, *J* = 16.9, 10.2, 6.5 Hz, 1H), 5.10 – 4.94 (m, 2H), 3.80 (d, *J* = 11.2 Hz, 7H), 3.11 (d, *J* = 22.7 Hz, 2H), 2.74 (t, *J* = 7.3 Hz, 2H), 2.35 (q, *J* = 6.9 Hz, 2H). **¹³C NMR (101 MHz, MeOD)** δ 201.37, 136.68, 114.21, 52.31 (d, *J*_{CP} = 6.6 Hz), 42.59 (d, *J*_{CP} = 1.3 Hz), 39.97 (d, *J*_{CP} = 6.6 Hz), 26.91. **R_f = 0.32** (90% EtOAc/hexanes), stains teal with bromocresol green. Analytical data are in accordance with the literature.



Synthesis of (*E*)-4-oxoocta-2,7-dienoic acid (3.14).

A flask was charged with dimethyl (2-oxohex-5-en-1-yl)phosphonate (0.41 g, 2 mmol) and 0.33 M solution of glyoxylic acid monohydrate in MeCN (15 ml, 5 mmol, 1.5 equiv), stored for 24 h over 4 Å molecular sieves. The mixture was stirred and cooled to 0 °C (ice bath), DBU (0.800 g, 5.2 mmol, 2.6 equiv) was added dropwise over a period of 30 min. The solution was stirred for an additional 1 h at the same temperature. The mixture was quenched with 1M HCl, the aqueous layer was extracted with EtOAc thrice, the combined organics were dried over Na₂SO₄, filtered and concentrated. Purification of the residue by flash chromatography (hexanes/EtOAc = 1:3) afforded 190 mg of the desired acid as a pale yellow solid in 62% yield. **¹H NMR (400 MHz, CDCl₃)** δ 7.17 (d, J = 16.0 Hz, 1H), 6.71 (d, J = 16.0 Hz, 1H), 5.85 (ddt, J = 16.8, 10.1, 6.5 Hz, 1H), 5.21 – 4.76 (m, 2H), 2.79 (t, J = 7.3 Hz, 2H), 2.49 – 2.34 (m, 2H). **¹³C NMR (101 MHz, CDCl₃)** δ 198.48, 169.85, 140.94, 136.28, 129.52, 115.73, 40.70, 27.37. **R_f = 0.35** (100% EtOAc), stains yellow with bromocresol green. Analytical data are in accordance with the literature.

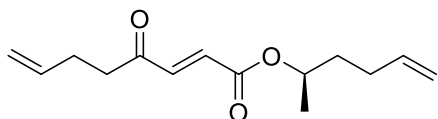


Synthesis of (*R*)-hex-5-en-2-ol (3.13).

To a solution of (*R*)-2-methyloxirane (1 g, 17.2 mmol) in diethyl ether (200 mL) at -78 °C was added allylmagnesium bromide (1M in hexanes, 17.2 mL, 1 equiv.), dropwise. The reaction mixture was stirred for 12 h at -78 °C, and a saturated solution of NH_4Cl was added. The mixture was extracted with diethyl ether thrice, and the combined organic extracts were dried over MgSO_4 , filtered, and concentrated under reduced pressure with great care to afford 1.3 g of the desired ester as a clear oil in 76% yield.

$^1\text{H NMR}$ (400 MHz, MeOD) δ 5.85 (ddt, $J = 16.9, 10.2, 6.7$ Hz, 1H), 5.12 – 4.91 (m, 2H), 3.78 – 3.69 (m, 1H), 2.25 – 2.05 (m, 2H), 1.62 – 1.42 (m, 2H), 1.18 (d, $J = 6.2$ Hz, 3H).

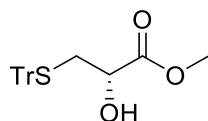
$^{13}\text{C NMR}$ (101 MHz, MeOD) δ 138.26, 113.42, 66.46, 37.94, 29.69, 22.01. $R_f = 0.85$ (5% EtOAc), stains with Seebach's stain. Analytical data are in accordance with the literature.



Synthesis of (*S*)-hex-5-en-2-yl (*E*)-4-oxoocta-2,7-dienoate (3.12).

(*E*)-4-oxoocta-2,7-dienoic acid (1.5 mmol; 231 mg) was dissolved in DCM (15 mL), and the mixture was cooled to 0 °C. DCC (1.2 equiv; 1.8 mmol; 370 mg), (*R*)-hex-5-en-2-ol (1.1 equiv; 1.63 mmol; 164 mg), and DMAP (0.1 equiv; 0.15 mmol; 14 mg) were added

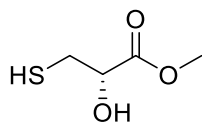
to the reaction mixture, which was stirred at 0 °C for 30 min and at rt for 2 h. Reaction mixture was filtered of the urea byproduct, concentration and purified by flash chromatography (hexanes/EtOAc = 4:1) which afforded 348 mg of the desired ester as a clear oil in 98% yield. **¹H NMR (400 MHz, MeOD)** δ 6.92 (d, J = 16.1 Hz, 1H), 6.59 (d, J = 16.1 Hz, 1H), 5.73 (dt, J = 16.8, 10.2, 6.6 Hz, 2H), 4.98 – 4.82 (m, 6H), 2.71 (t, J = 7.3 Hz, 2H), 2.25 (q, J = 7.0 Hz, 2H), 2.06 – 1.96 (m, 2H), 1.73 – 1.49 (m, 2H), 1.18 (d, J = 6.3 Hz, 3H). **Rf** = 0.85 (5% EtOAc),



Synthesis of (S)-2-hydroxy-3-(tritylthio)propanoic acid (3.#).

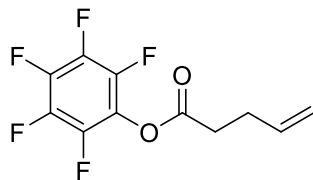
Triphenylmethanethiol (2.75 g, 10 mmol) was dissolved in THF (40 mL) and the reaction mixture was cooled to 0 °C. NaH (60% dispersion in mineral oil; 400 mg, 10 mmol) was added portionwise, and the resulting solution was stirred at 0 °C for an additional 15 min. Potassium (*R*)-oxirane-2-carboxylate 11 (1 g; 7.5 mmol) was added in one portion, and the resulting reaction mixture was then gradually warmed to RT, stirred for 14 h before being poured into H₂O (250 mL), and extracted with Et₂O thrice. The Et₂O layer was discarded, and the aqueous phase was acidified by 1 N HCl to pH 3 and was extracted with EtOAc thrice. The combined EtOAc layers were washed with brine, dried over anhydrous MgSO₄, and concentrated to provide the crude product as a pale yellow viscous oil, which was crystallized from acetonitrile, affording (*R*)-2-hydroxy-3-(tritylthio)propanoic acid (1.98 g, 72%) as a white solid. **¹H NMR (400 MHz, MeOD)** δ 5.85 (ddt, J = 16.9, 10.2, 6.7 Hz, 1H), 5.12 – 4.91 (m, 2H), 3.78 – 3.69 (m, 1H), 2.25 –

2.05 (m, 2H), 1.62 – 1.42 (m, 2H), 1.18 (d, J = 6.2 Hz, 3H). **¹³C NMR (101 MHz, MeOD)** δ 138.26, 113.42, 66.46, 37.94, 29.69, 22.01. **Rf** = 0.85 (5% EtOAc), stains with Seebach's stain. Analytical data are in accordance with the literature.



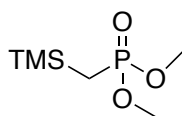
Synthesis of methyl (S)-2-hydroxy-3-mercaptopropanoate (3.#).

(S)-2-hydroxy-3-(tritylthio)propanoic acid (4 mmol; 1.5 g) was dissolved in DCM (24 mL), and triethylsilane (3 equiv; 12 mmol; 2.0 mL) was added in one portion. The reaction mixture was cooled to 0 °C, and trifluoroacetic acid (2.4 mL) was added dropwise. After 30 min, the reaction mixture was concentrated under reduced pressure, resulting in a white solid. The crude product was washed 4 times with hexanes to remove triphenylmethane and dried under reduced pressure, yielding (S)-2-hydroxy-3-mercaptopropanoic acid (436 mg, 85%) of as a white solid. The crude acid was taken up in MeOH (40 mL) and HCl (400 μL), and allowed to stir for 24 h. The reaction mixture was concentrated under reduced pressure, and the resulting residue taken up in hot DCM, which afforded 474 mgs of methyl (S)-2-hydroxy-3-mercaptopropanoate in quantitative yields. **¹H NMR (400 MHz, MeOD)** δ 5.85 (ddt, J = 16.9, 10.2, 6.7 Hz, 1H), 5.12 – 4.91 (m, 2H), 3.78 – 3.69 (m, 1H), 2.25 – 2.05 (m, 2H), 1.62 – 1.42 (m, 2H), 1.18 (d, J = 6.2 Hz, 3H). **¹³C NMR (101 MHz, MeOD)** δ 138.26, 113.42, 66.46, 37.94, 29.69, 22.01. **Rf** = 0.85 (5% EtOAc), stains with Seebach's stain. Analytical data are in accordance with the literature.



Synthesis of perfluorophenyl pent-4-enoate (3.21).

To a solution of pent-4-enoic acid (305 mg, 2.50 mmol) and pentafluorophenol (506 mg, 2.75 mmol, 1.1 equiv) in DCM (12 mL) at 0 °C were added DCC (719 mg, 3.75 mmol, 1.5 equiv) and DMAP (61 mg, 0.5 mmol, 0.2 equiv). The mixture was stirred at rt for 1 h, and a saturated solution of NH₄Cl was added. The mixture was extracted with EtOAc, and the combined organic extracts were dried over MgSO₄, filtered, and concentrated under reduced pressure. Purification of the residue by flash chromatography (hexanes/EtOAc = 98:2) afforded 709 mg of the desired ester as a white solid. **¹H NMR (400 MHz, CDCl₃)** δ 5.80 (ddt, *J* = 16.8, 10.2, 6.4 Hz, 1H), 5.16 – 4.92 (m, 2H), 2.70 (t, *J* = 7.4 Hz, 2H), 2.55 – 2.33 (m, 2H). **¹³C NMR (101 MHz, MeOD)** δ 172.97, 136.47, 127.71, 114.54, 65.75, 33.00, 28.51. **R_f** = 0.85 (5% EtOAc).



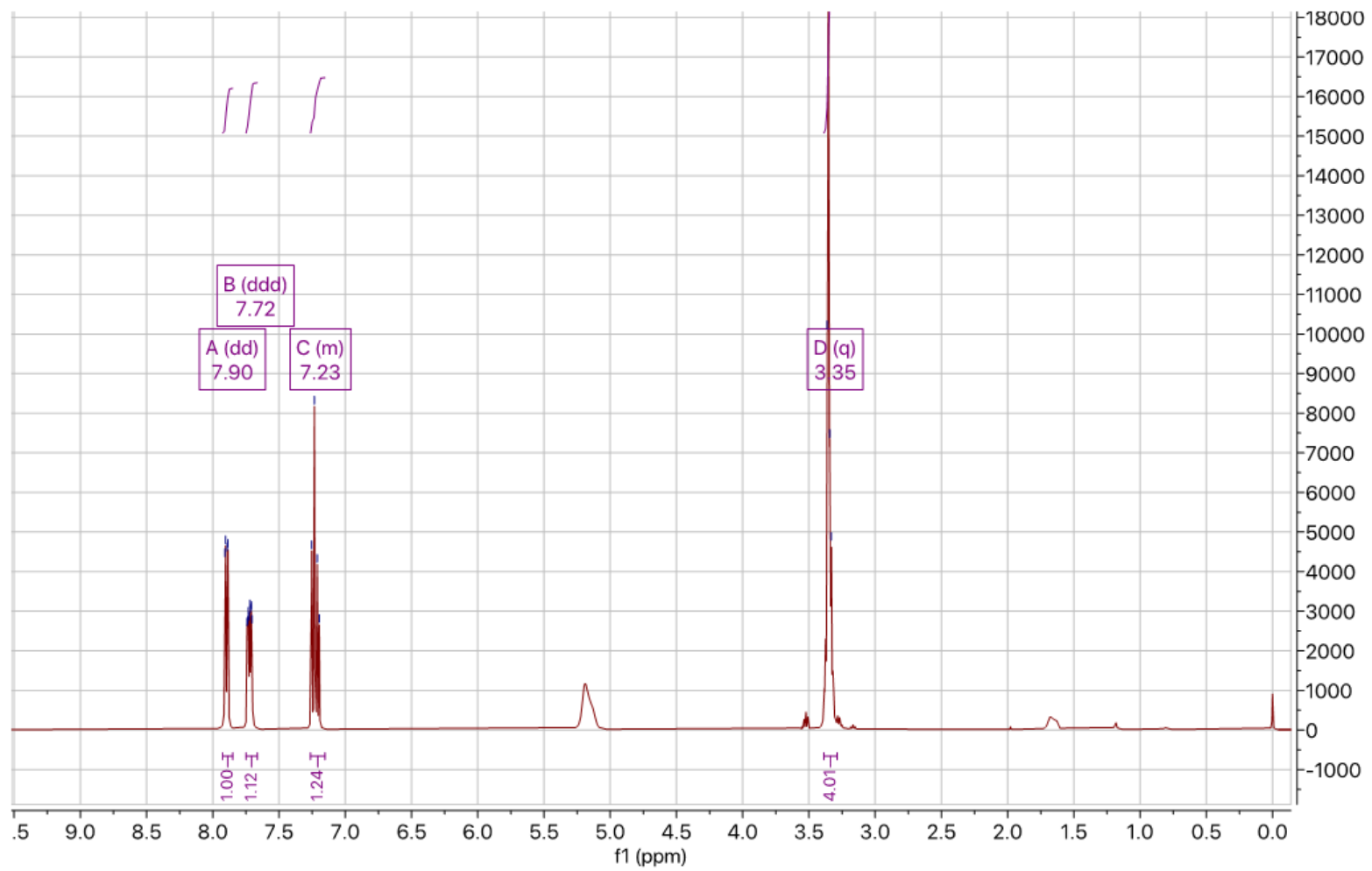
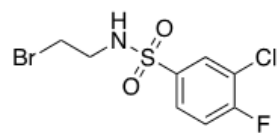
Synthesis of α-(trimethylsilyl)methylphosphonate.

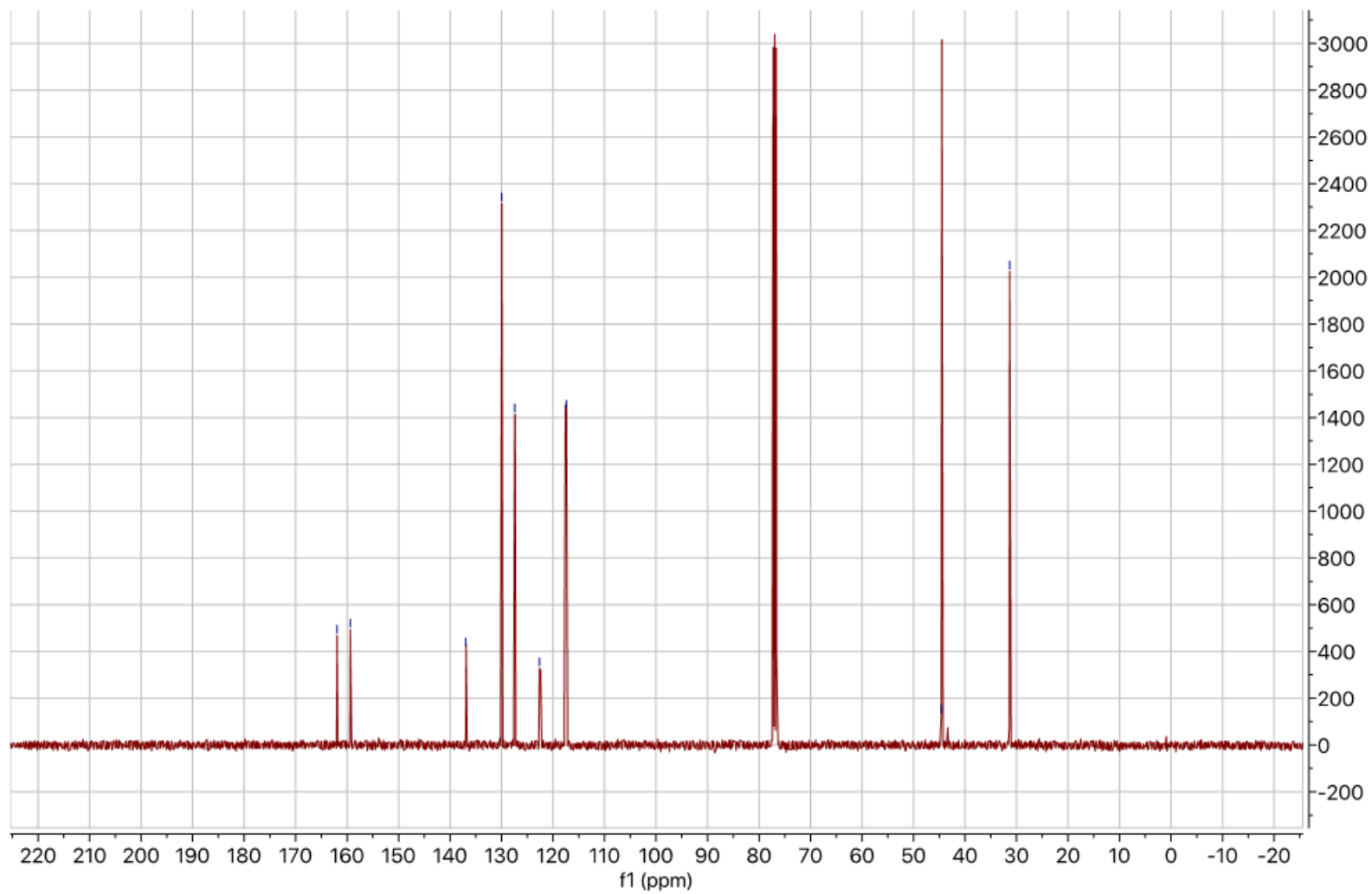
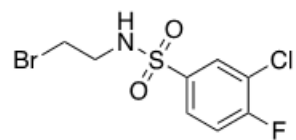
To a solution of n-BuLi (2.6 mL, 2.5 M in hexanes, 6.6 mmol, 2.2 equiv) in THF (15 mL) at –78 °C was added DMMP (750 μL, 6.9 mmol, 2.3 equiv). After 30 min at –78 °C, a solution of TMSCl (3.0 mmol, 1 equiv) in THF (15 mL) was added dropwise. The reaction mixture was stirred for 30 min at –78 °C, and a saturated solution of NH₄Cl was added. The mixture was extracted with EtOAc, and the combined organic extracts were

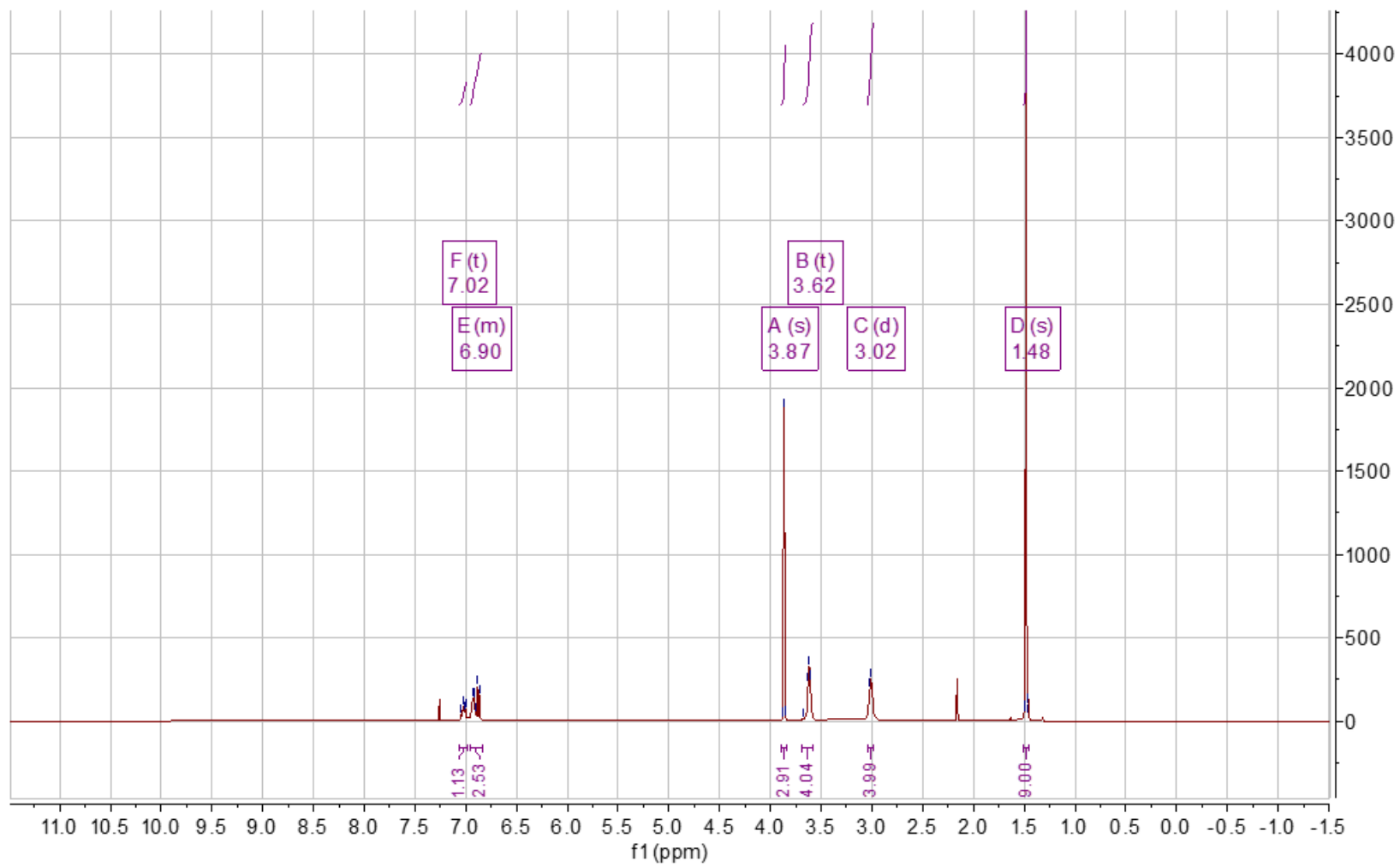
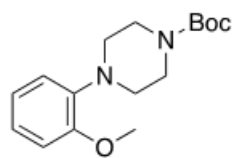
dried over MgSO₄, filtered, and concentrated under reduced pressure to afford 1.08 g of the desired α -(trimethylsilyl)methylphosphonate as a clear oil in 82% yield. **¹H NMR (400 MHz, CDCl₃)** δ 3.54 (d, J = 11.1 Hz, 6H), 0.99 (d, J = 22.1 Hz, 2H), 0.00 (d, J = 12.5 Hz, 10H). **¹³C NMR (101 MHz, CDCl₃)** δ 51.76, 13.91, 12.63, -0.61.

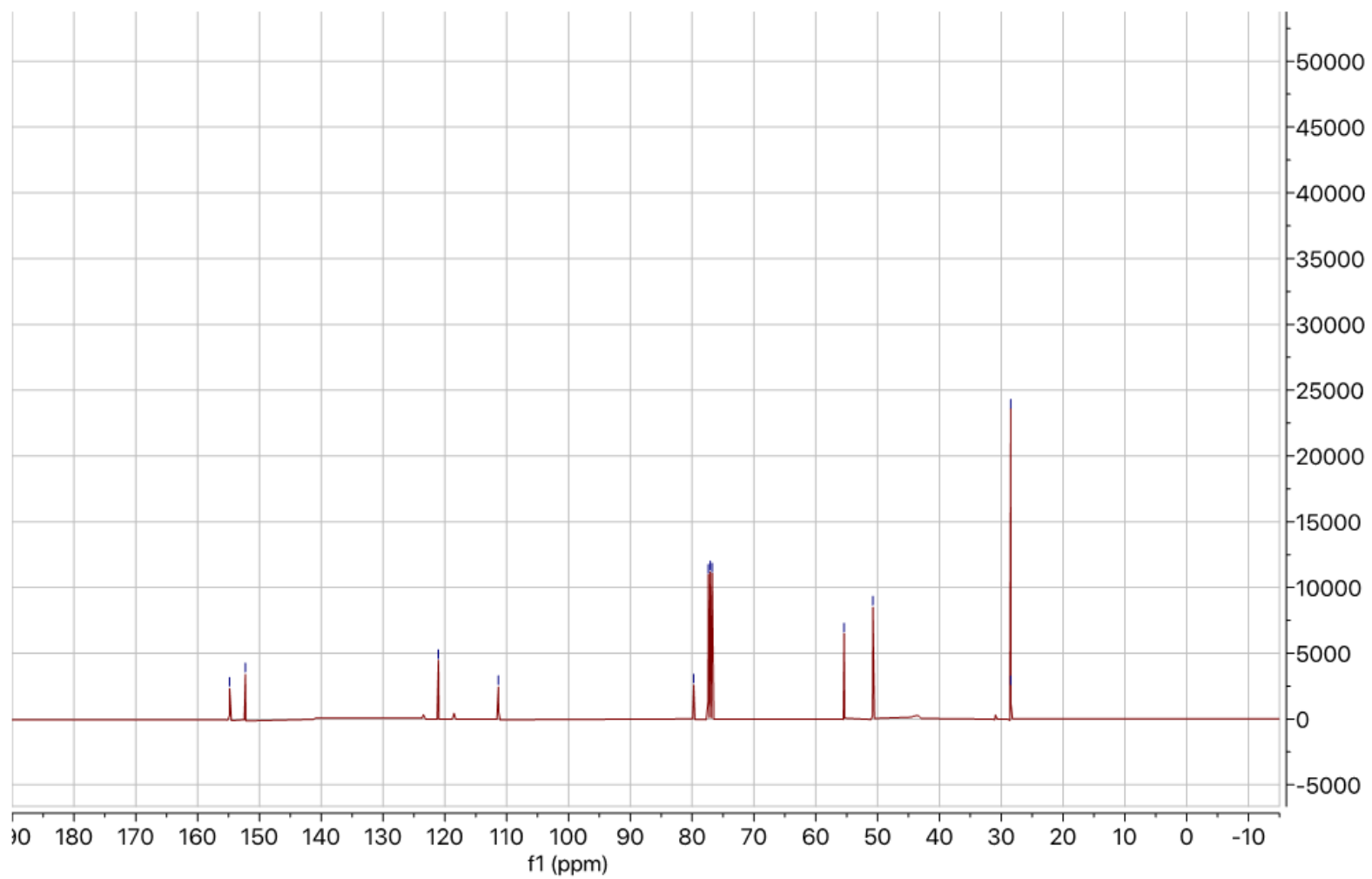
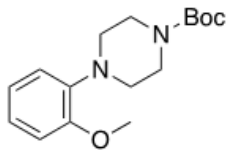
Appendix A

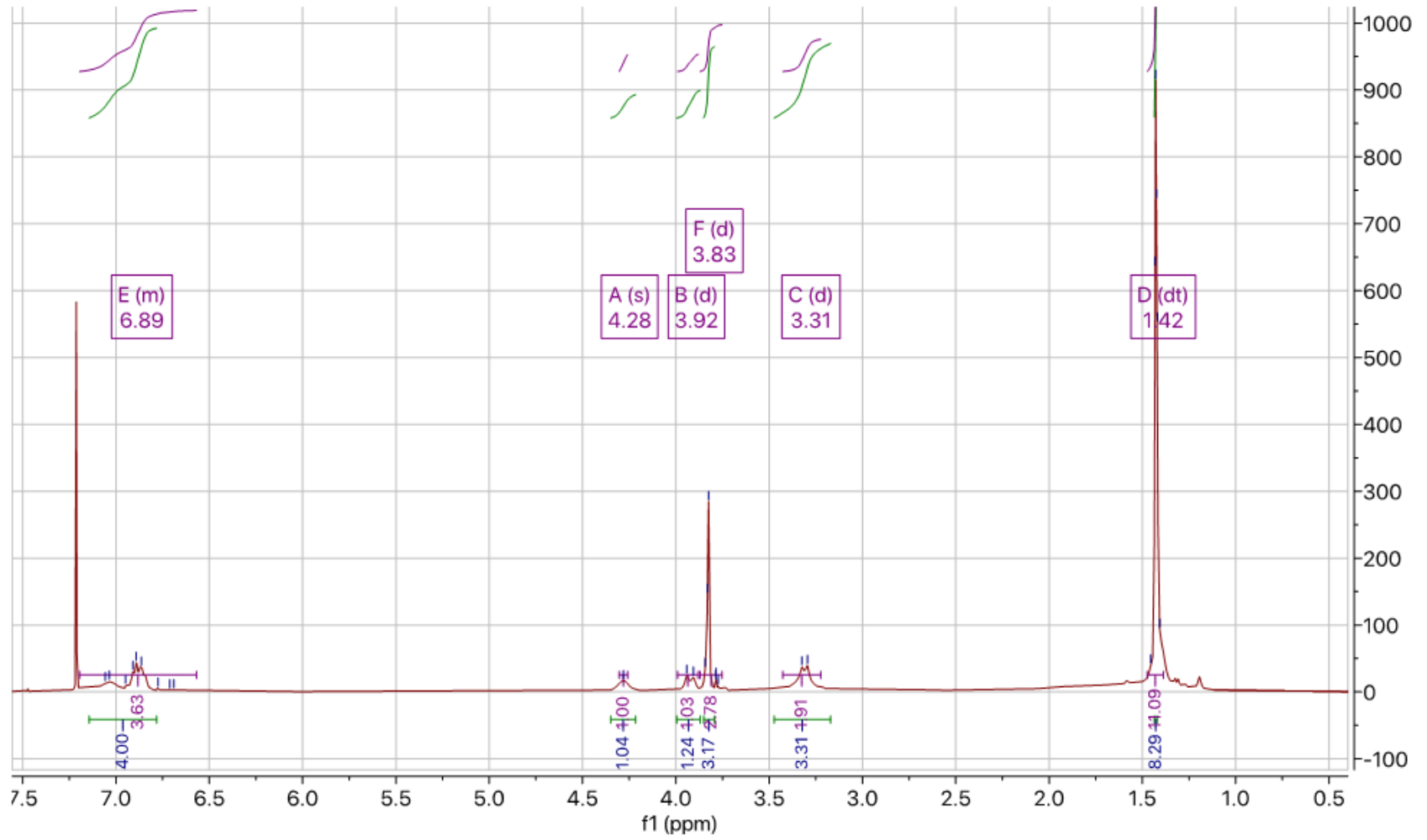
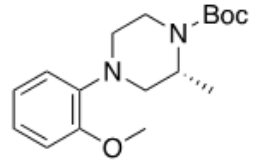
Relevant Spectra to Chapter I

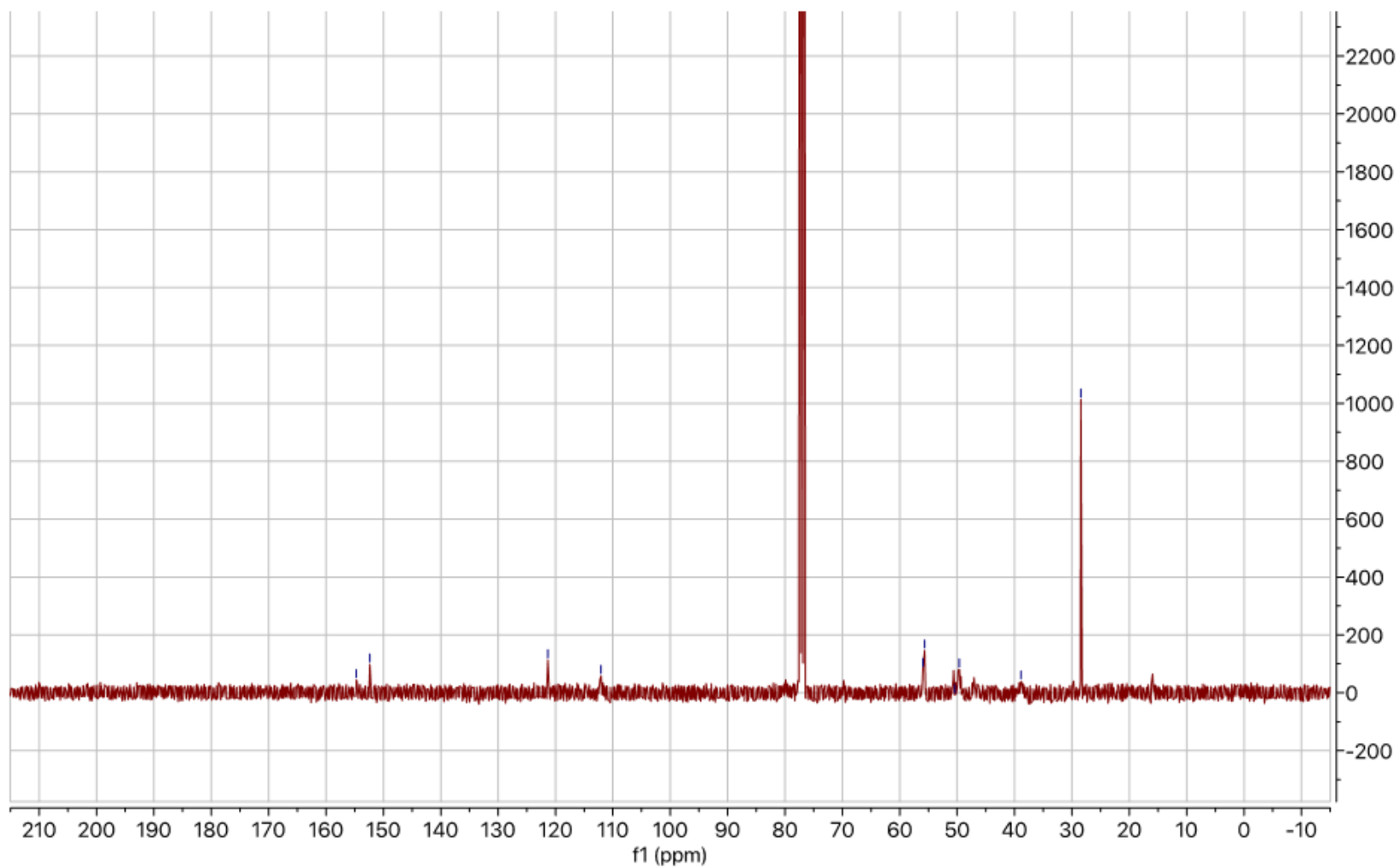
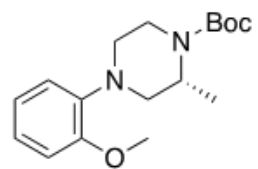




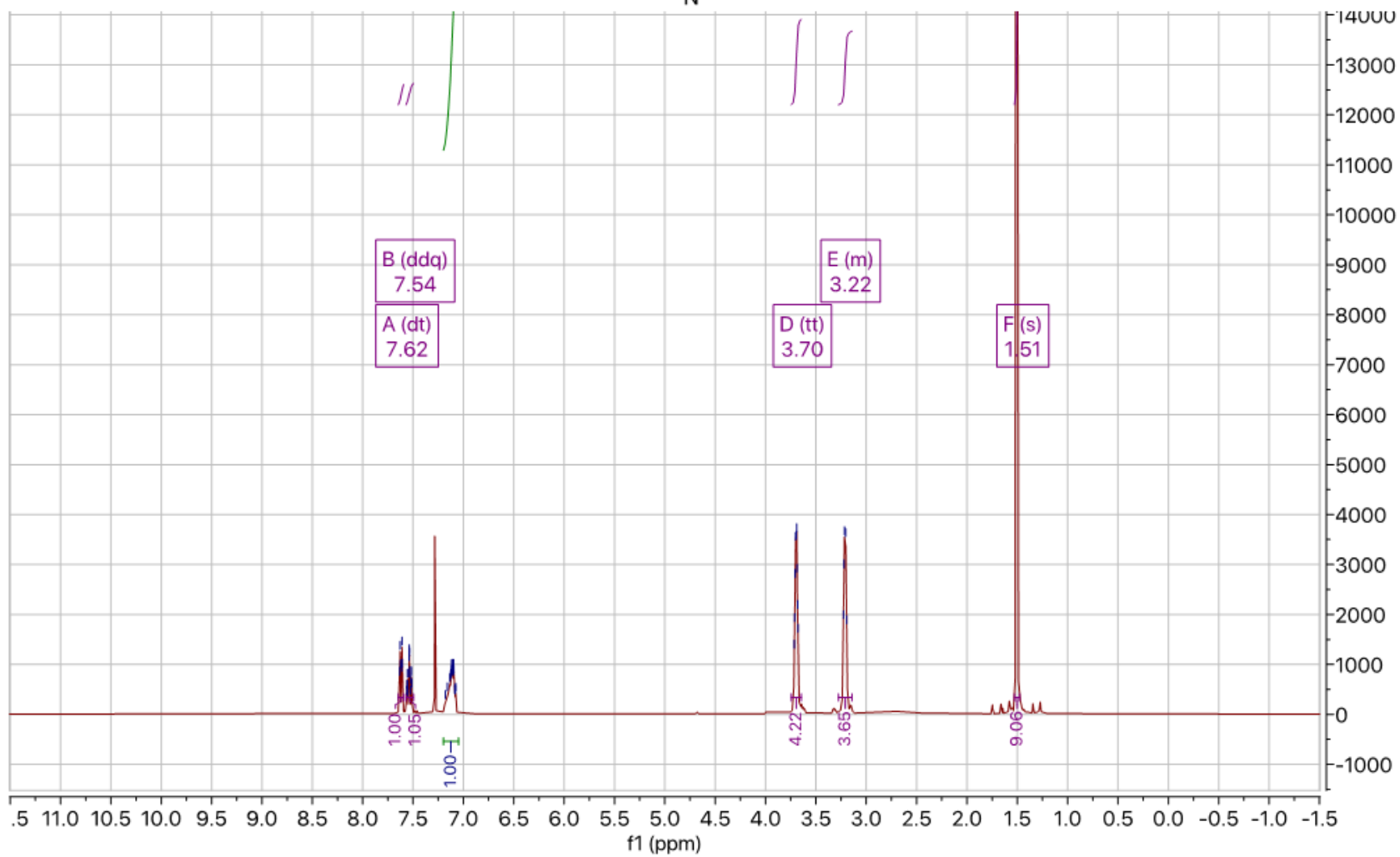
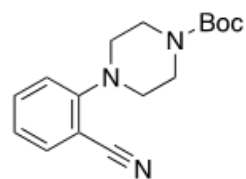


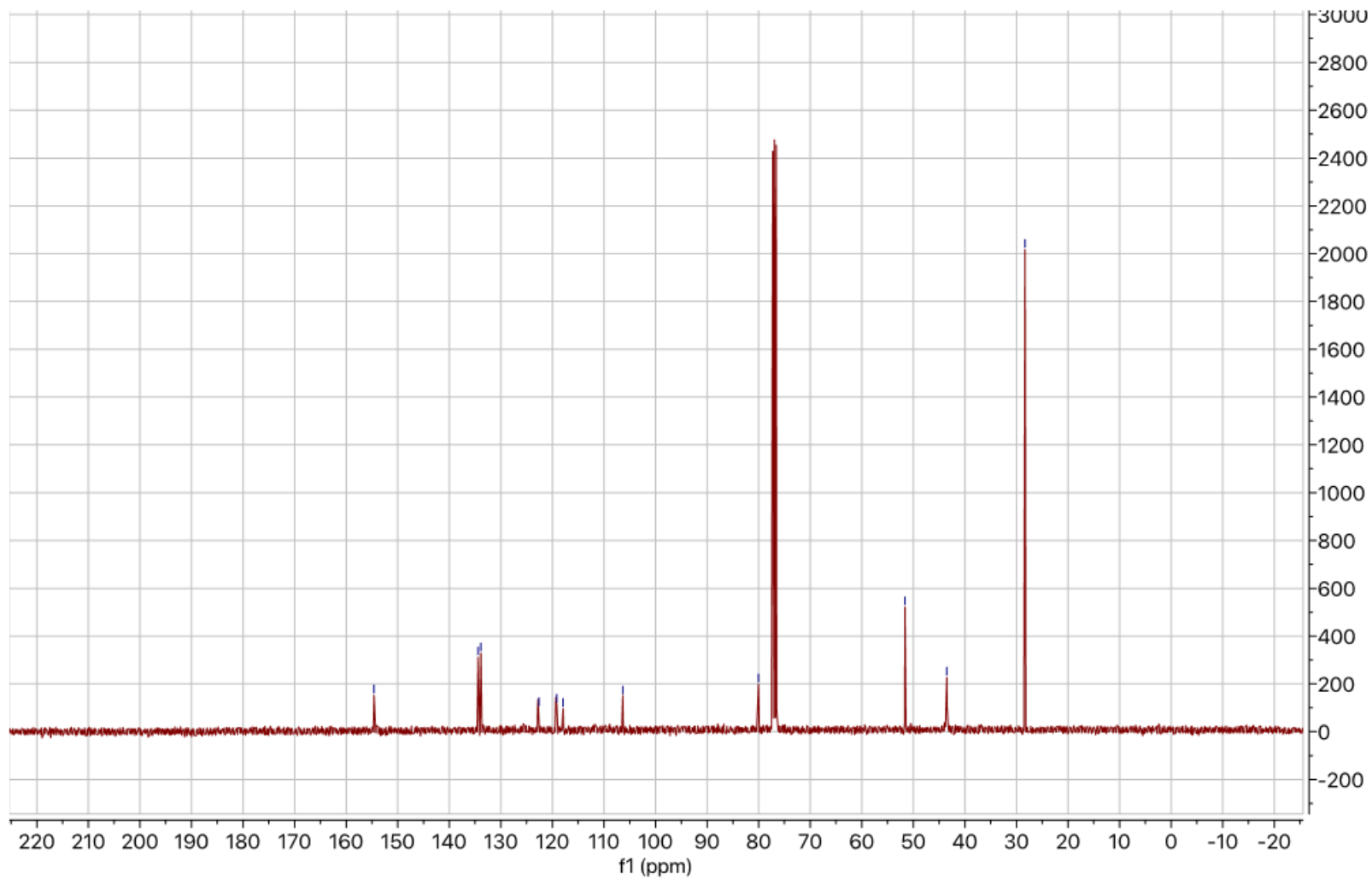
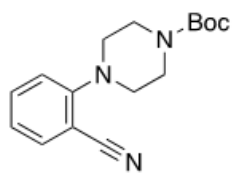


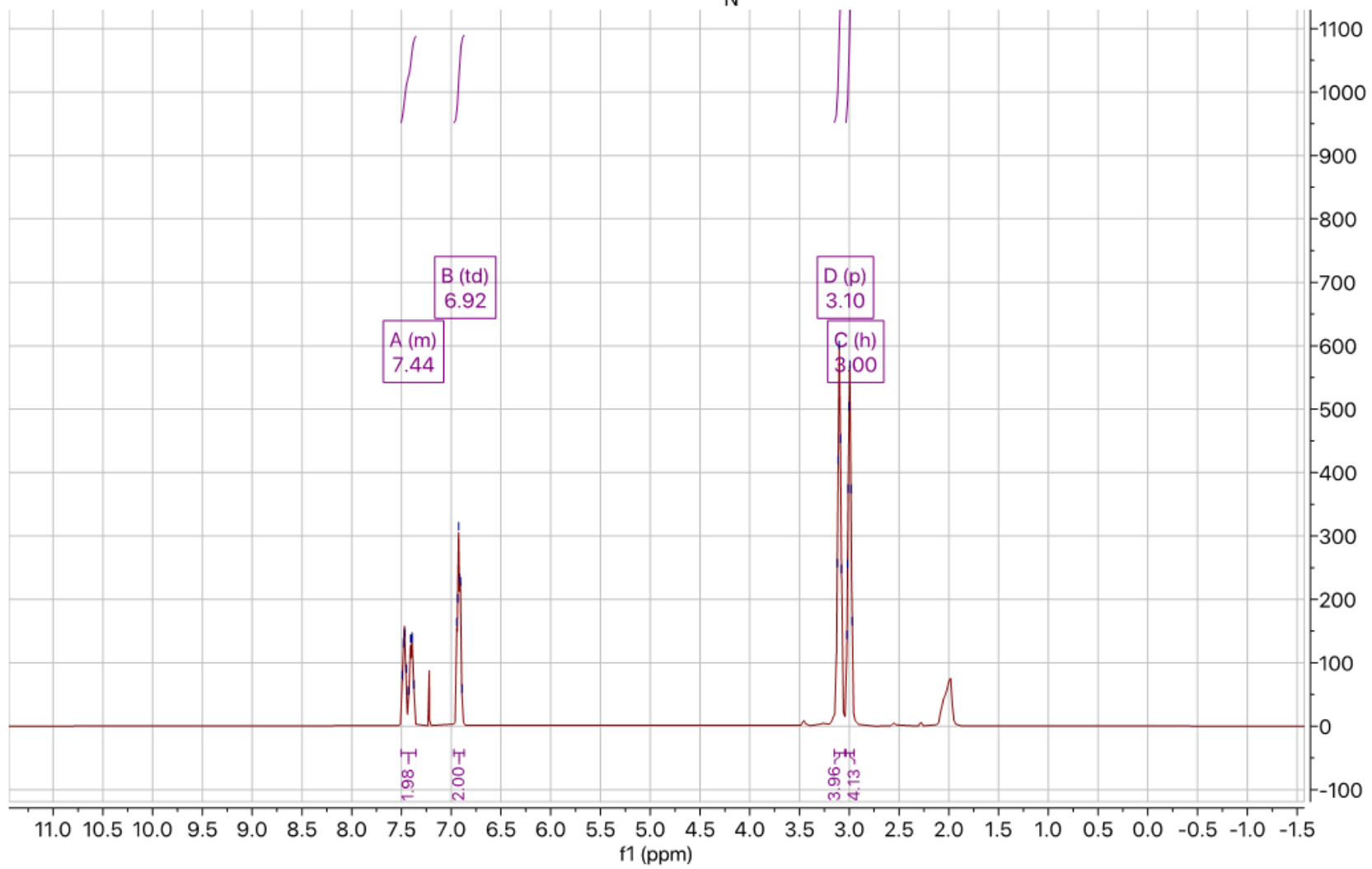
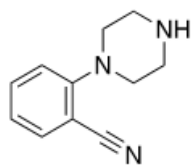


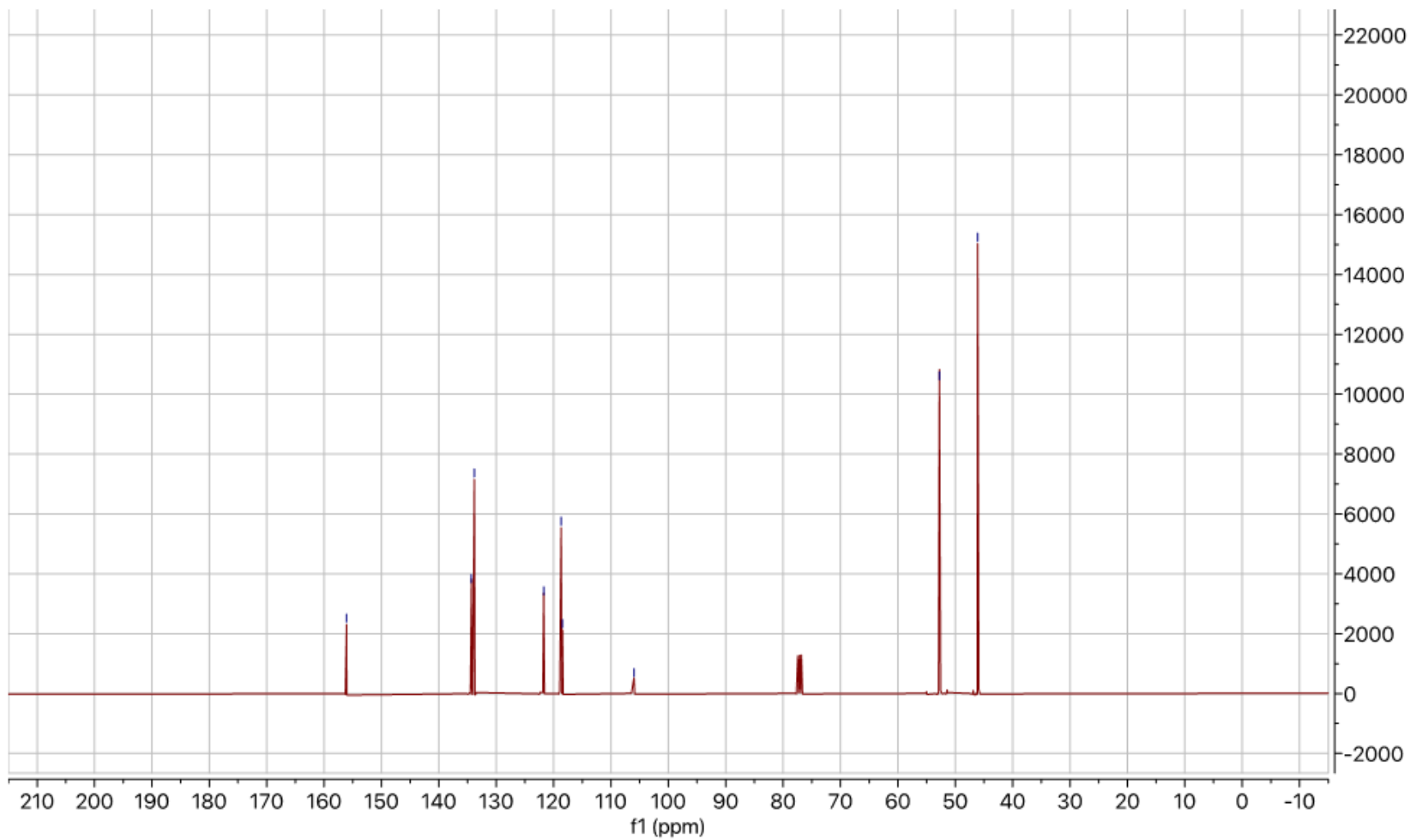
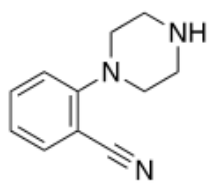


111

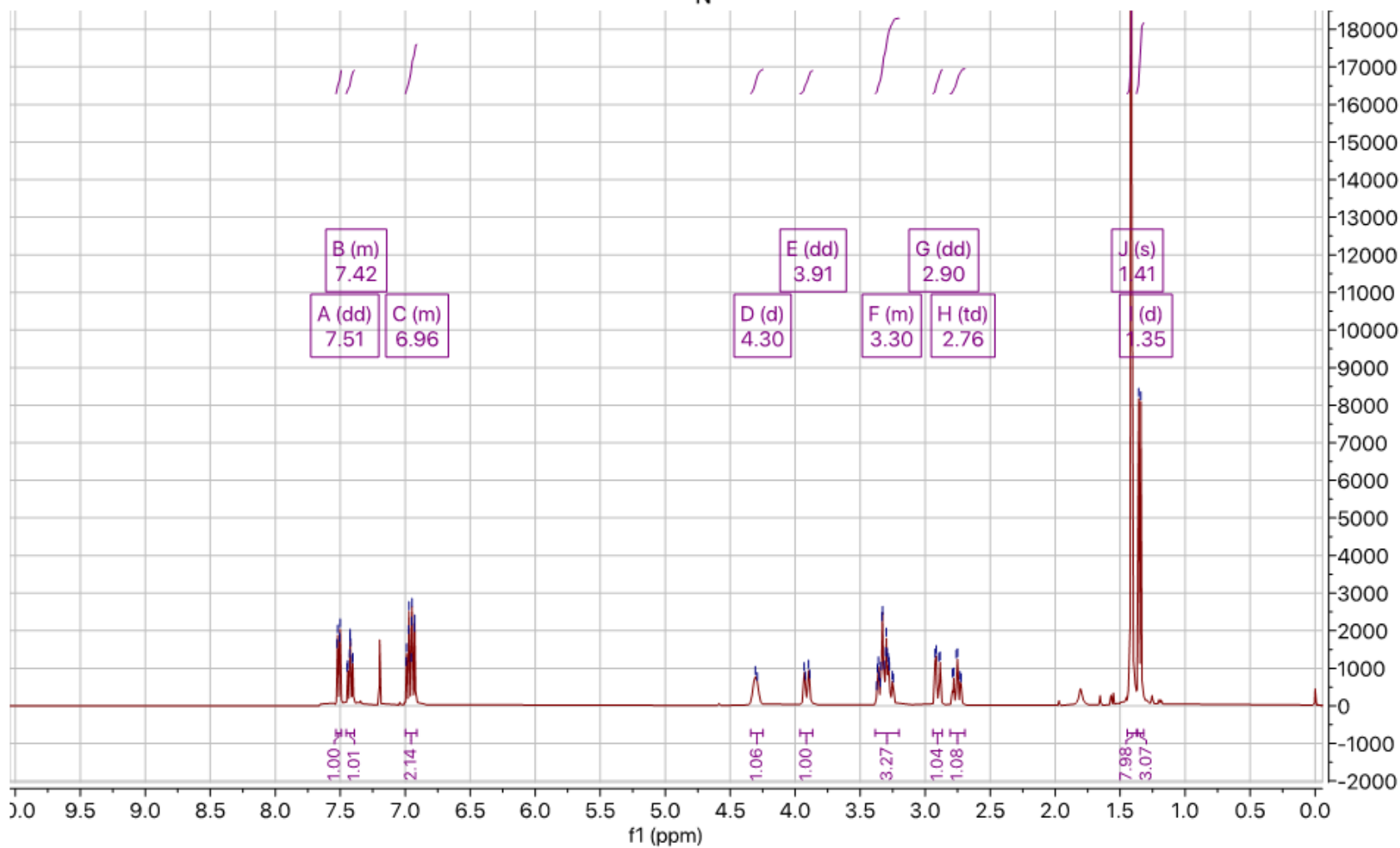
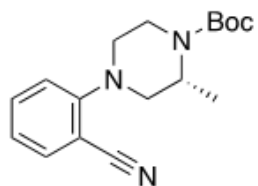


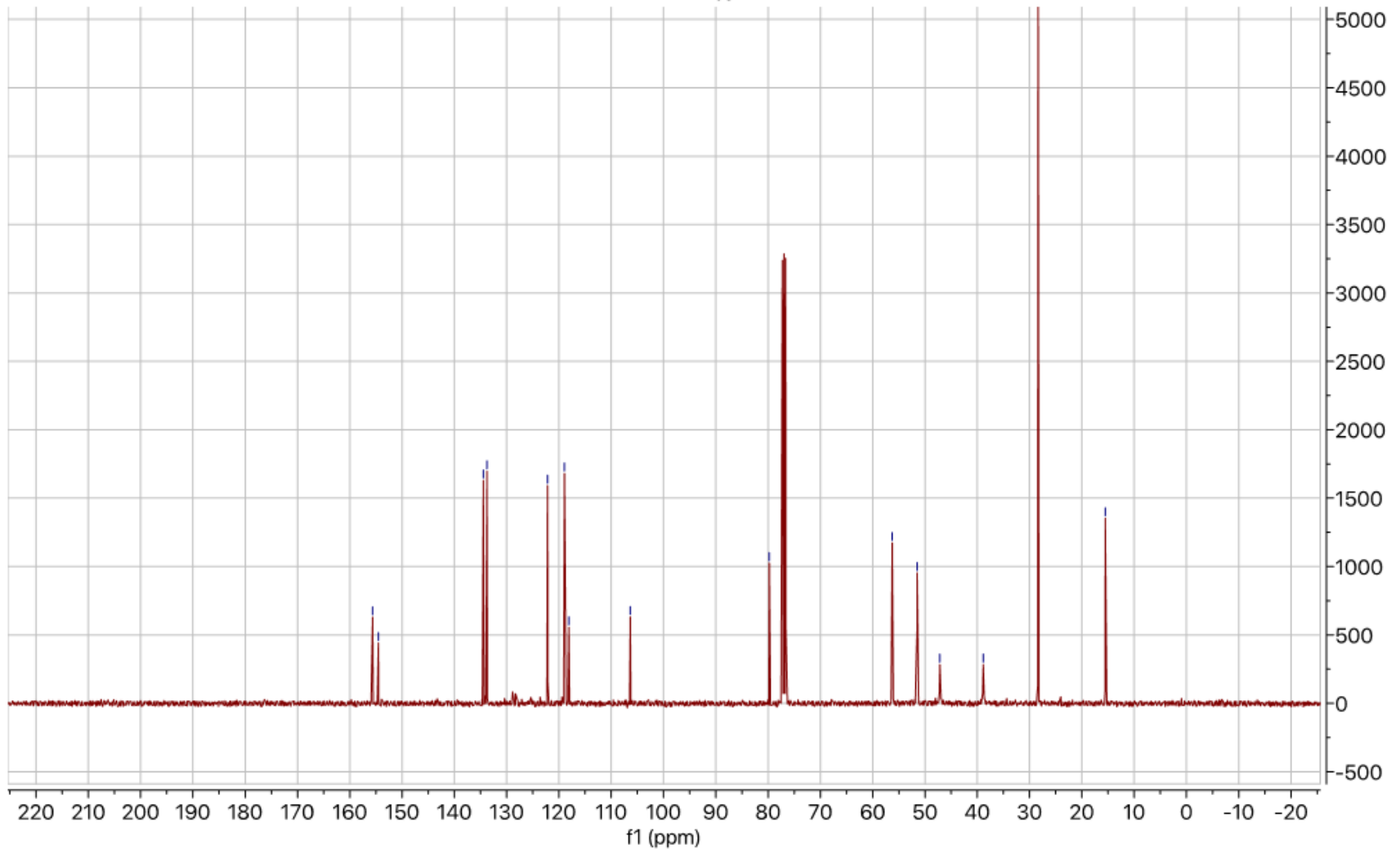
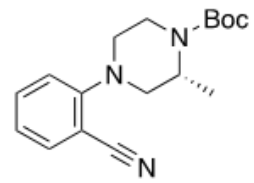


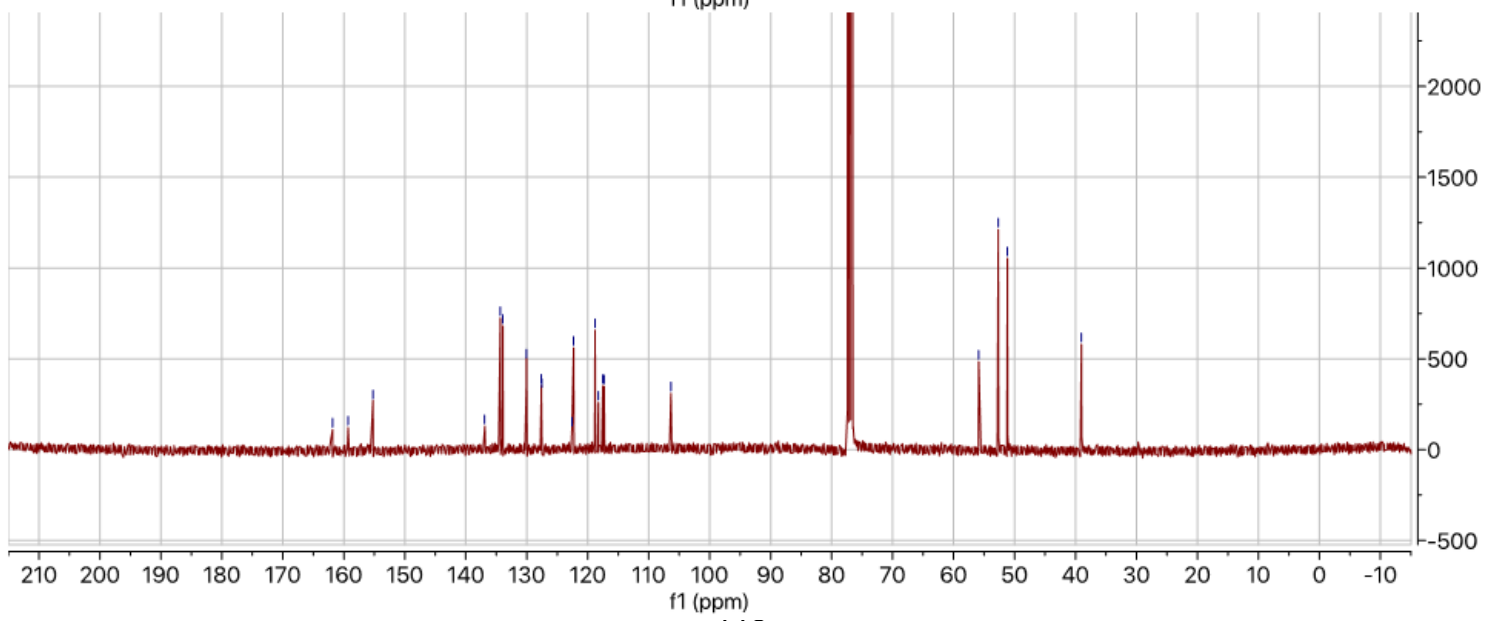
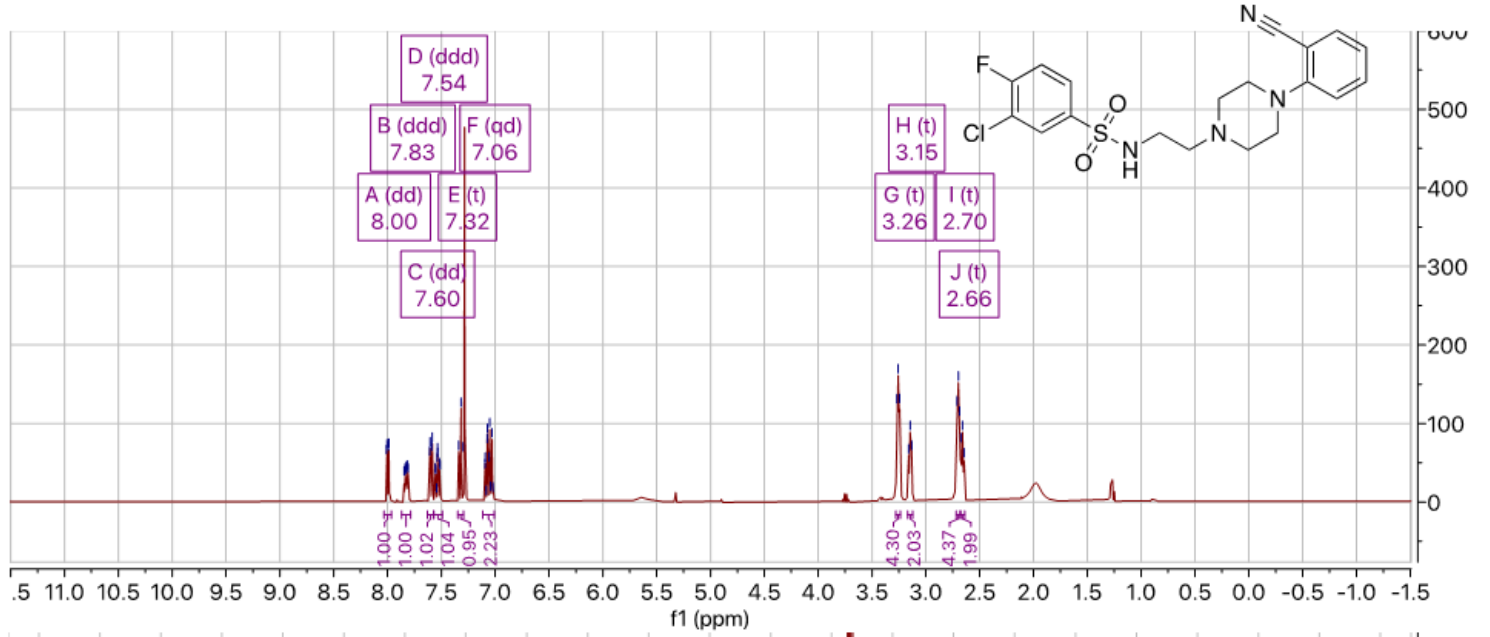


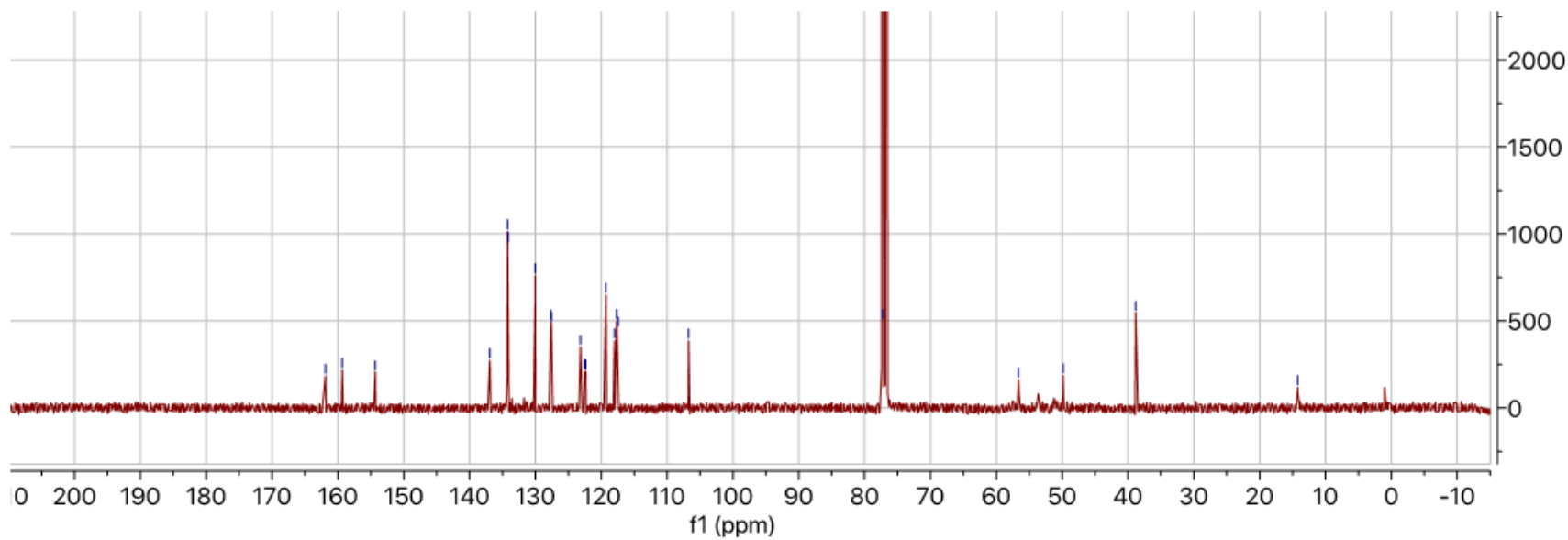
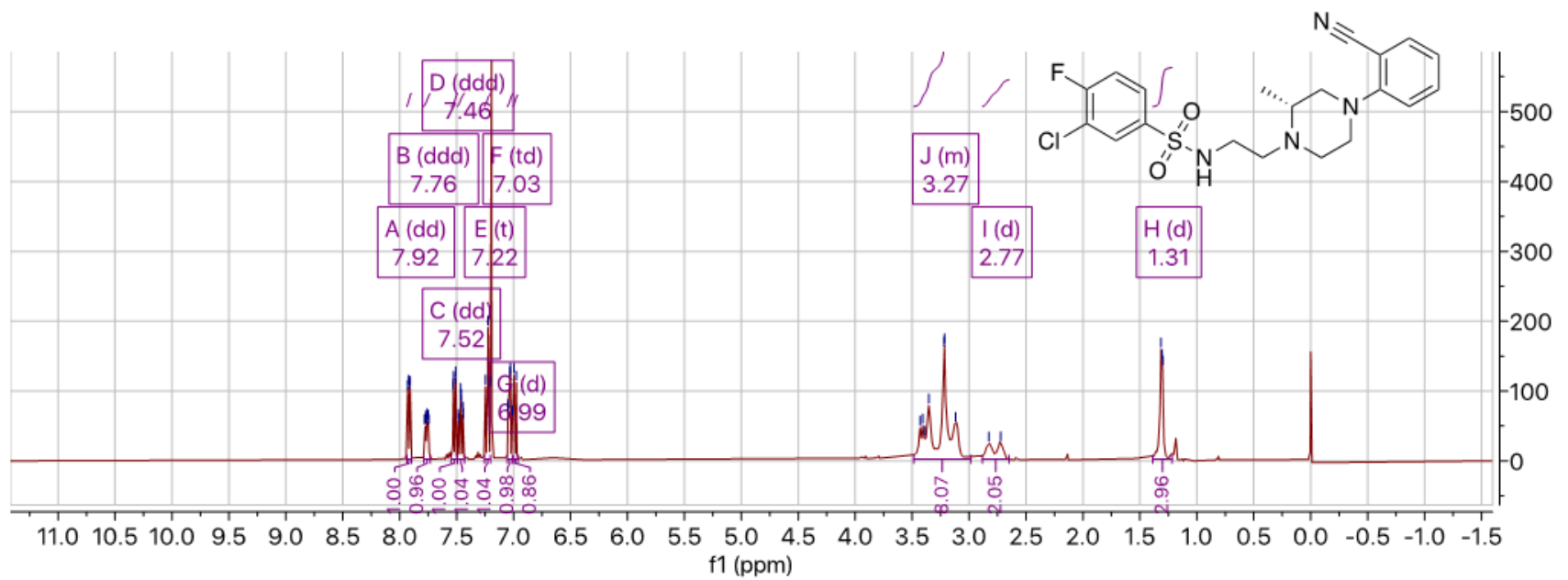


115



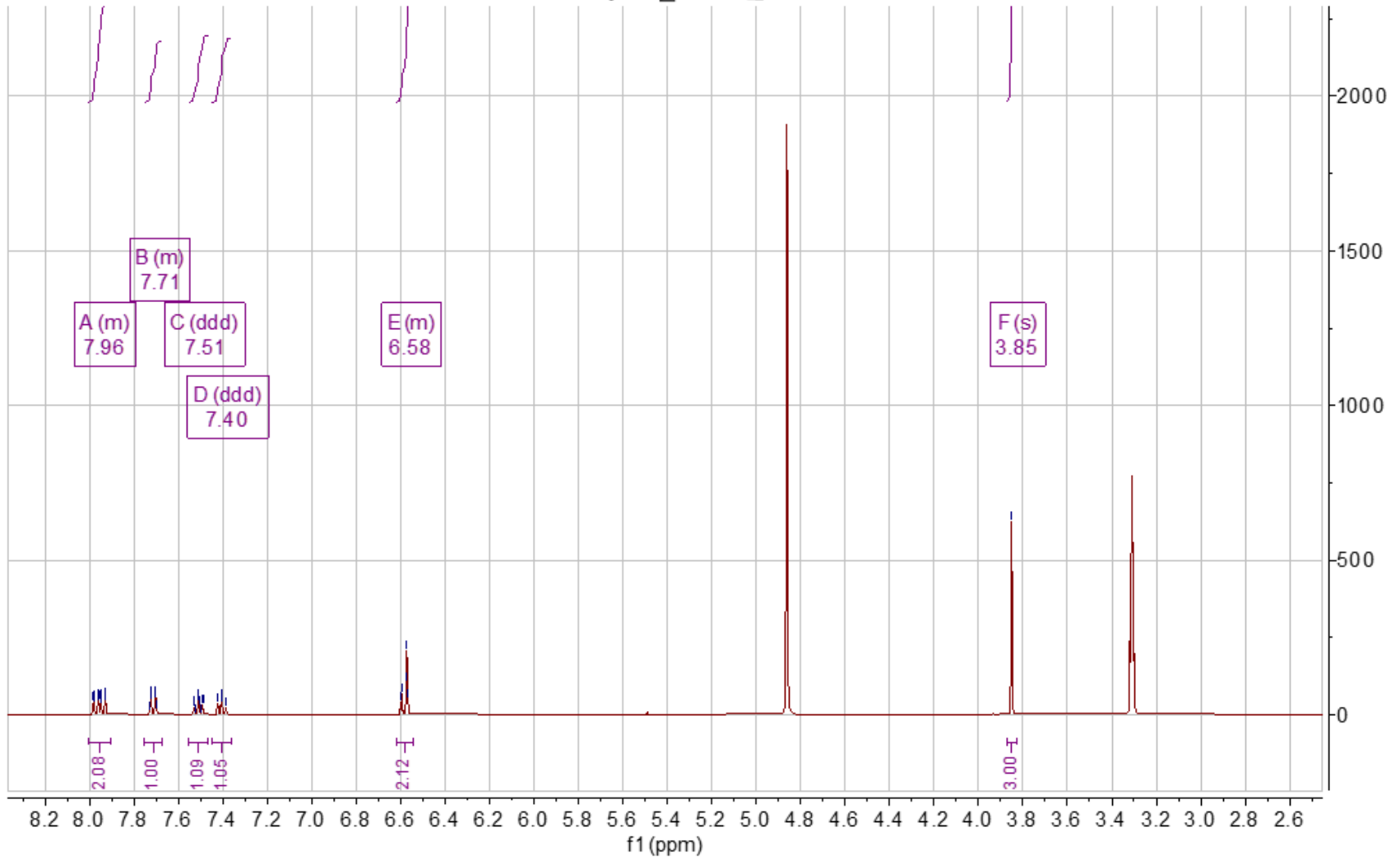
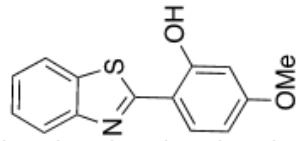


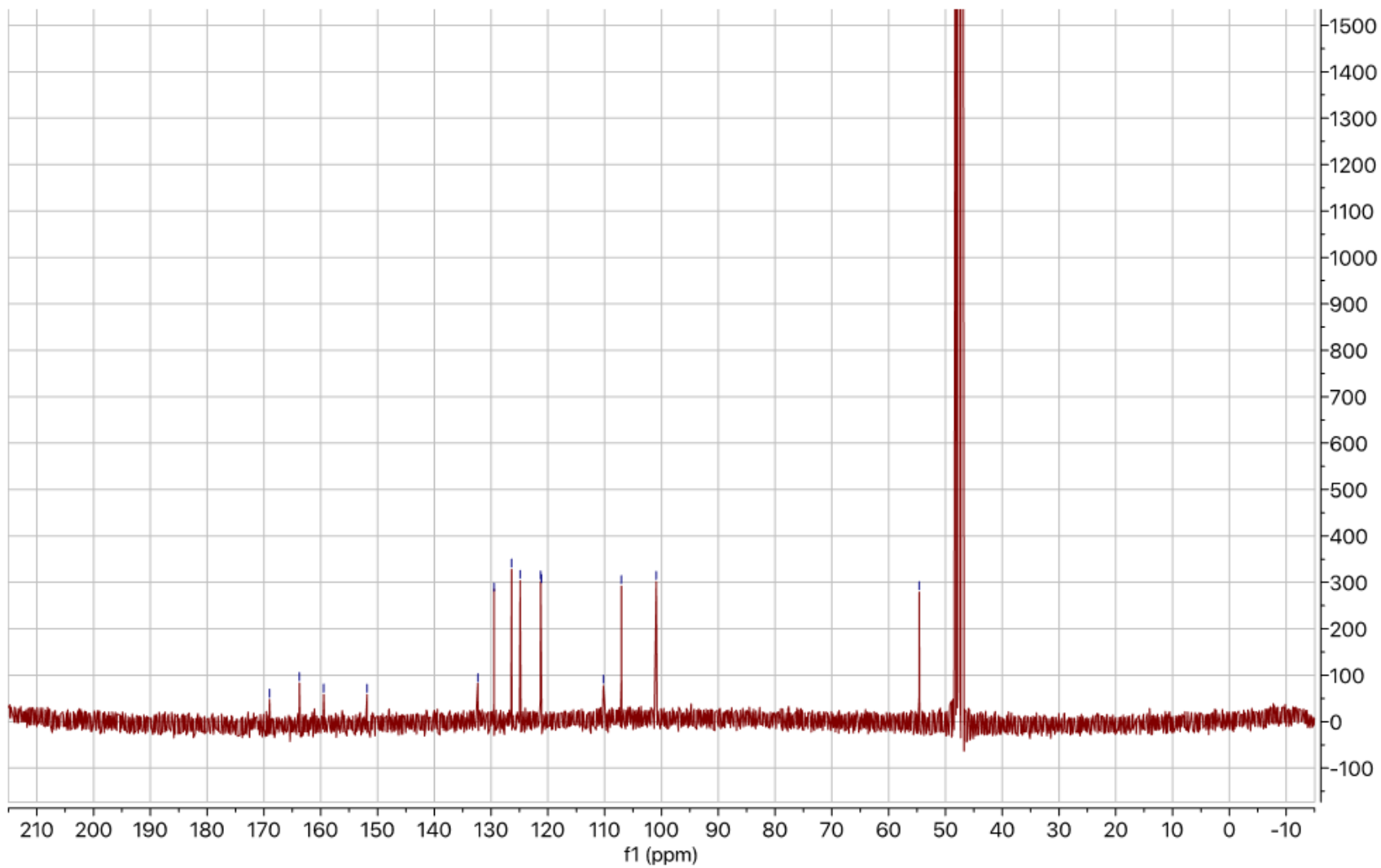
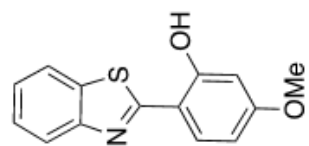




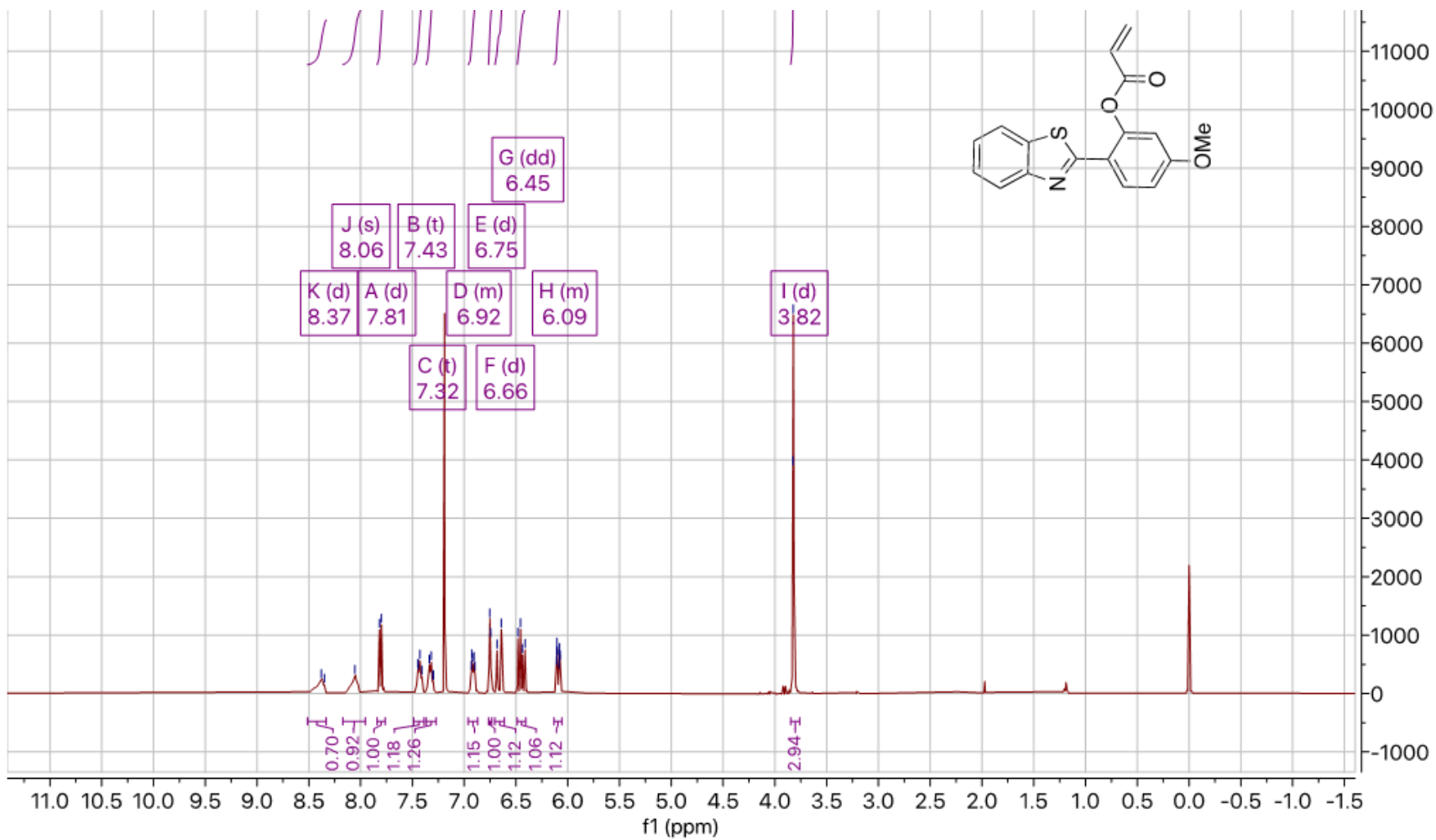
Appendix B

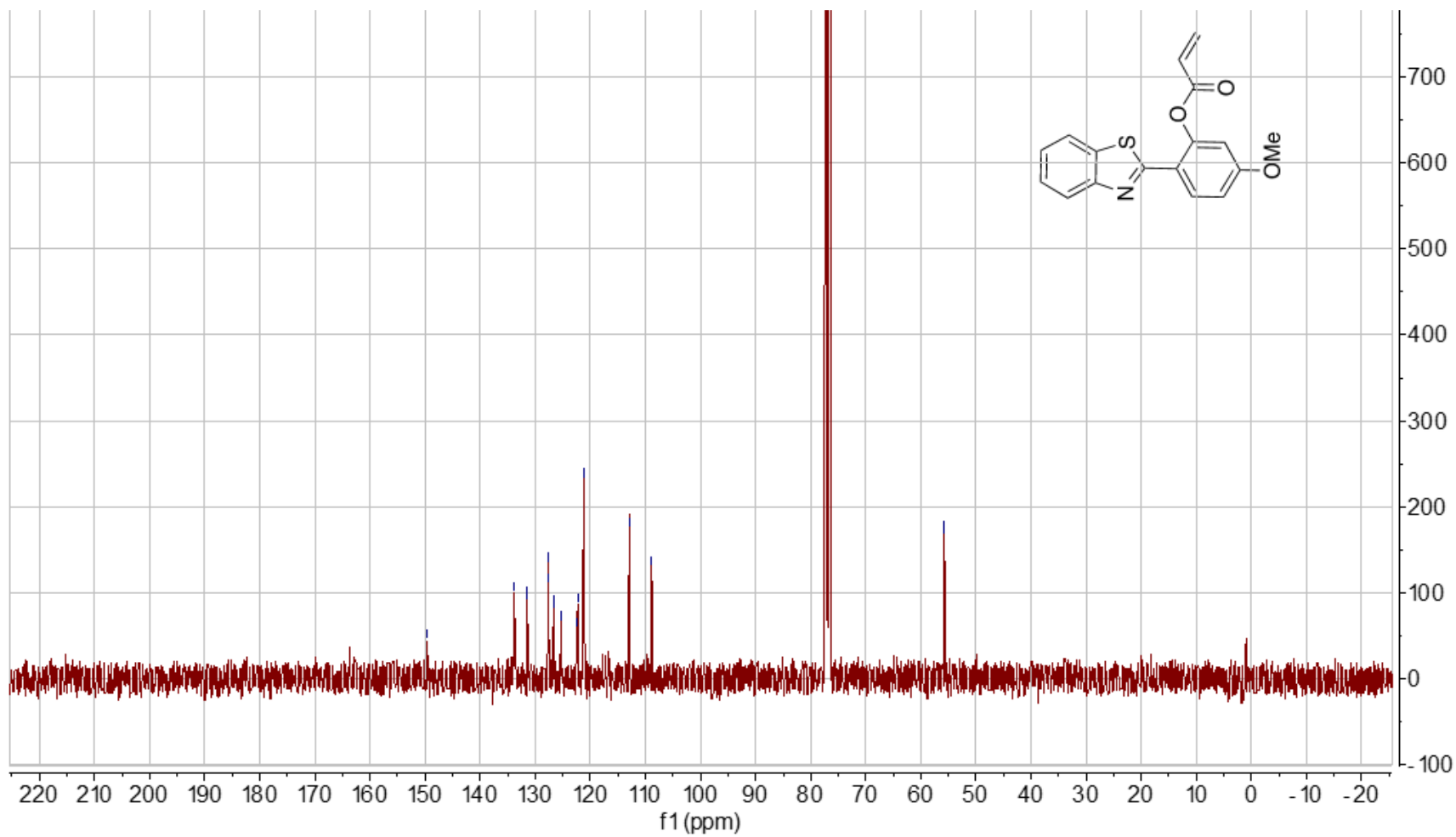
Relevant Spectra to Chapter II

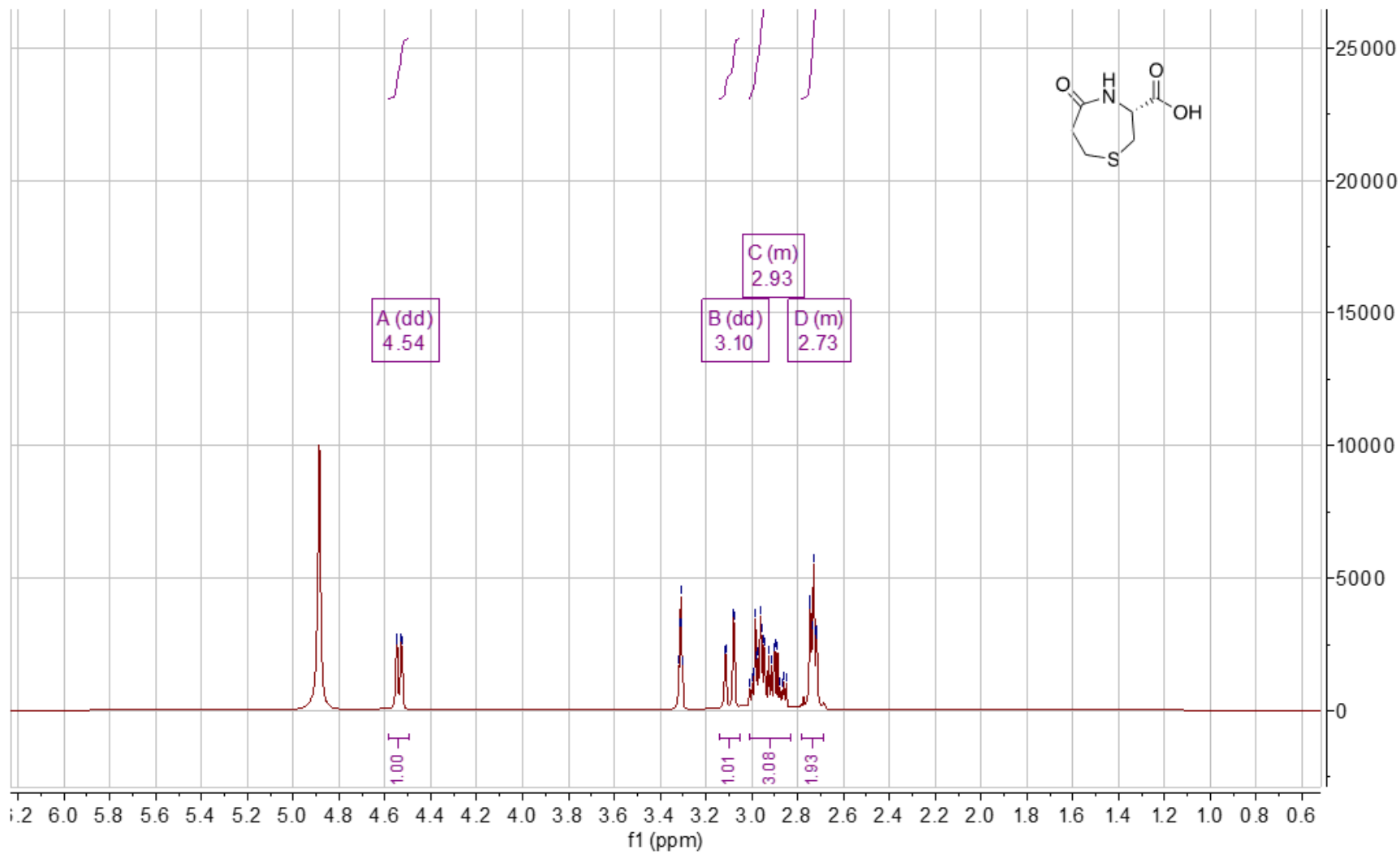


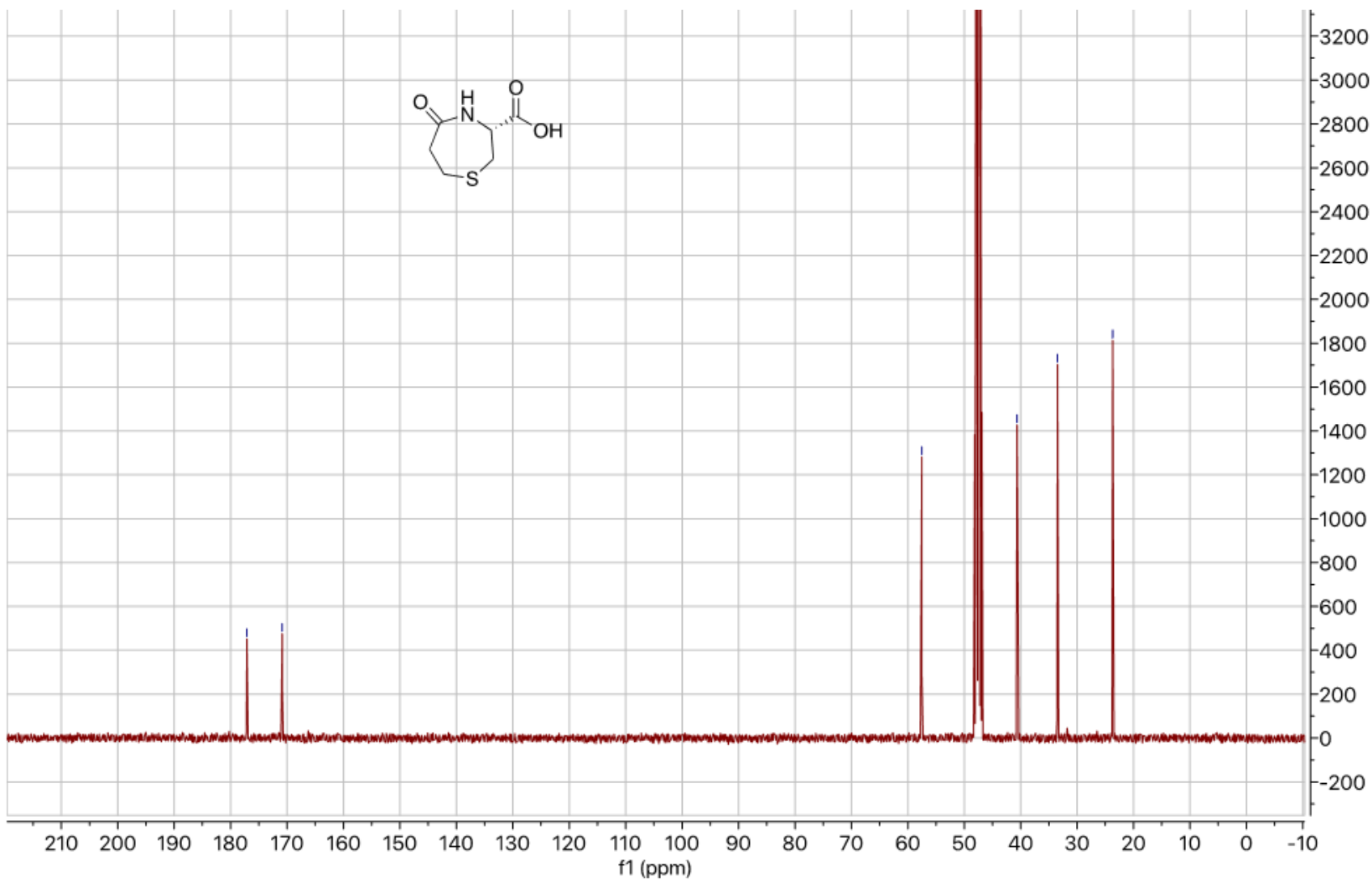


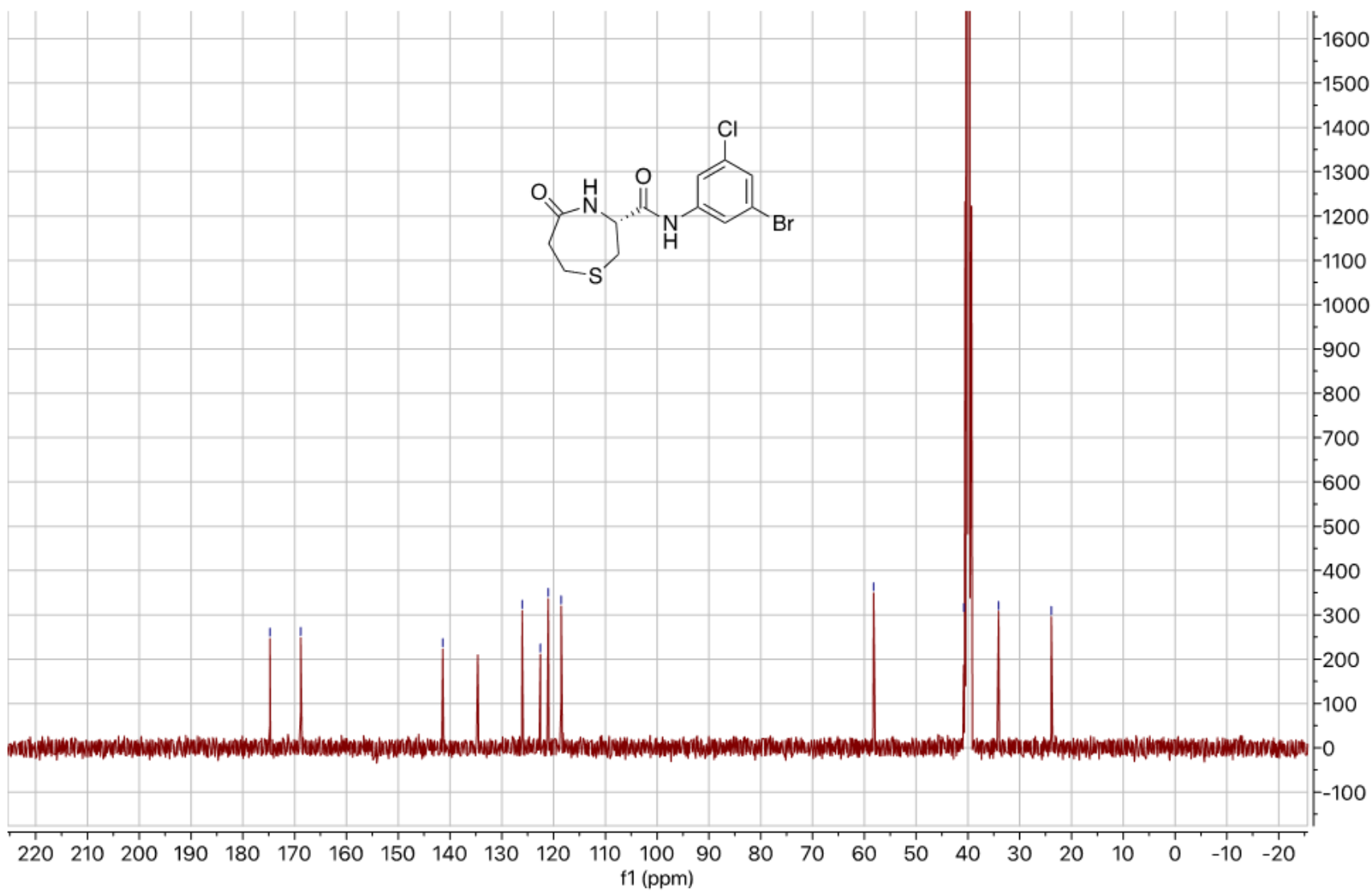
122

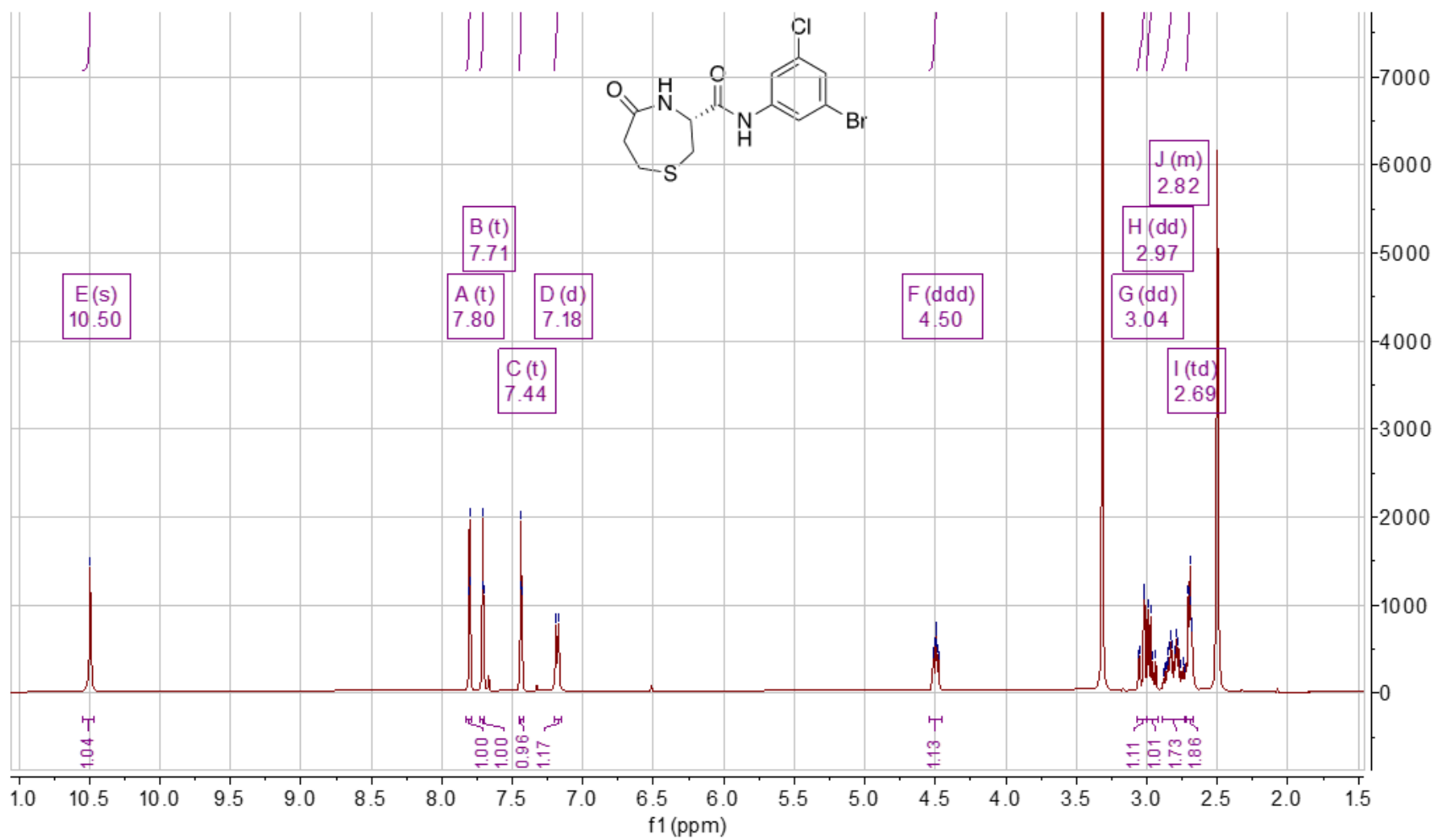






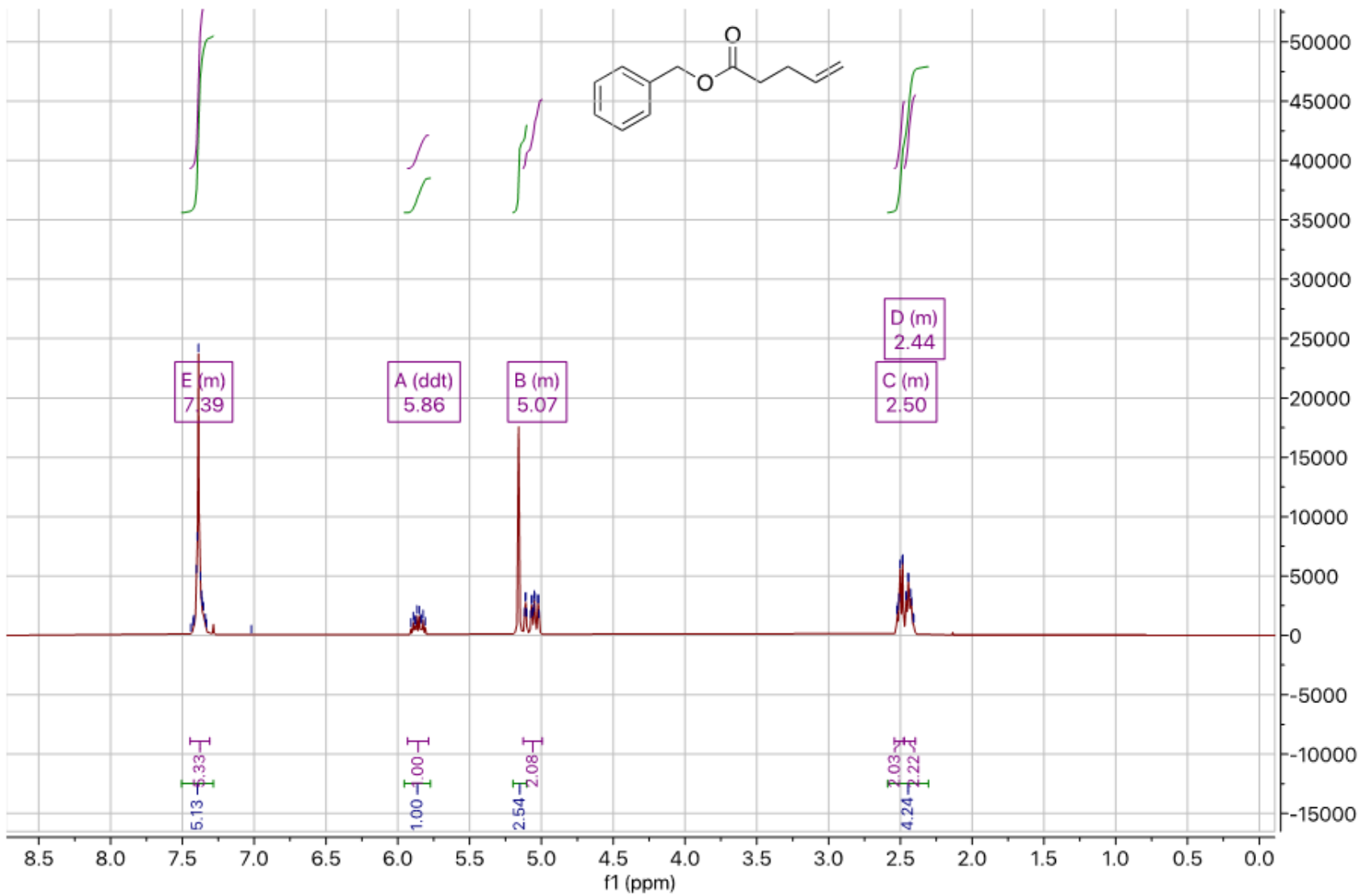


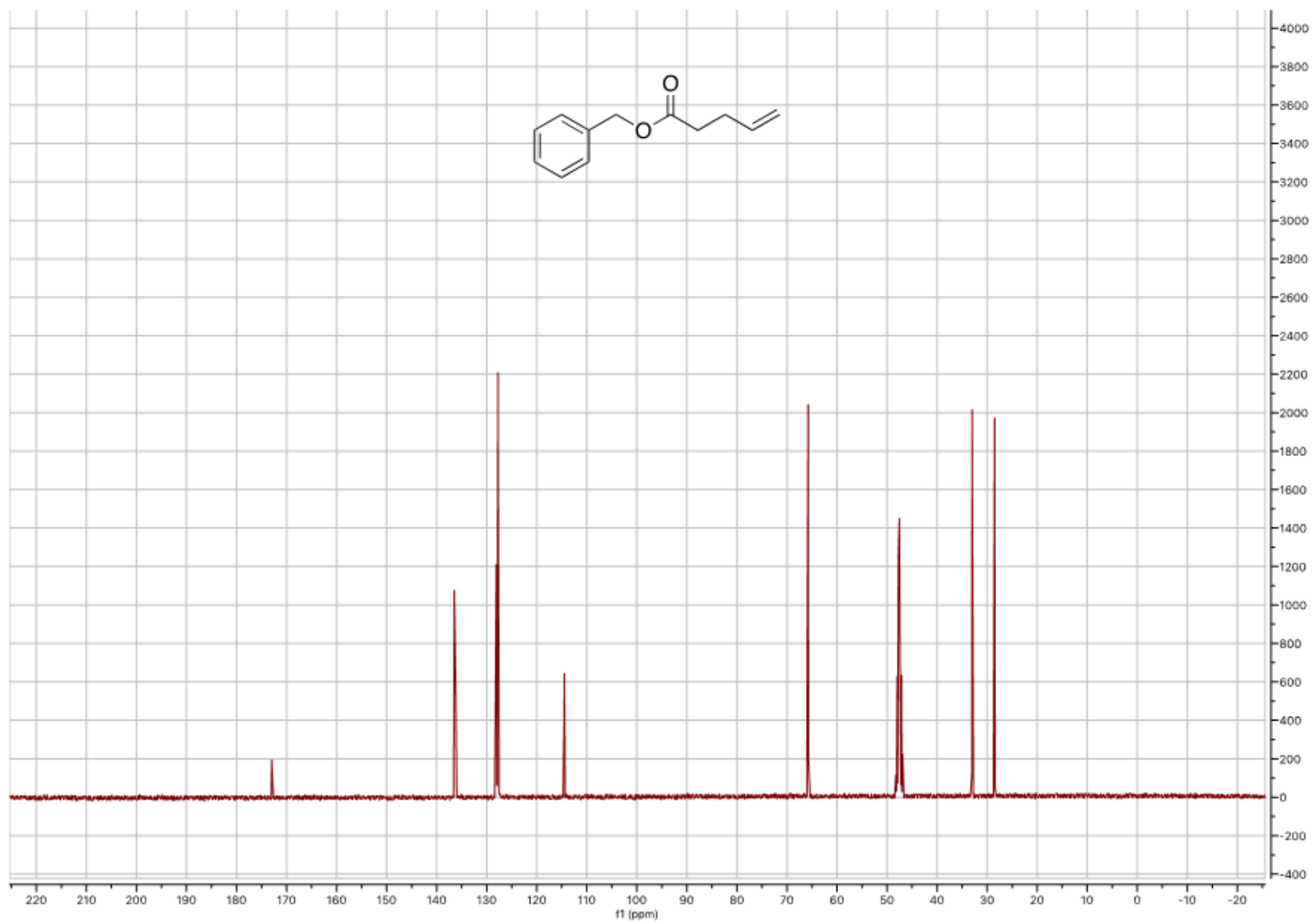


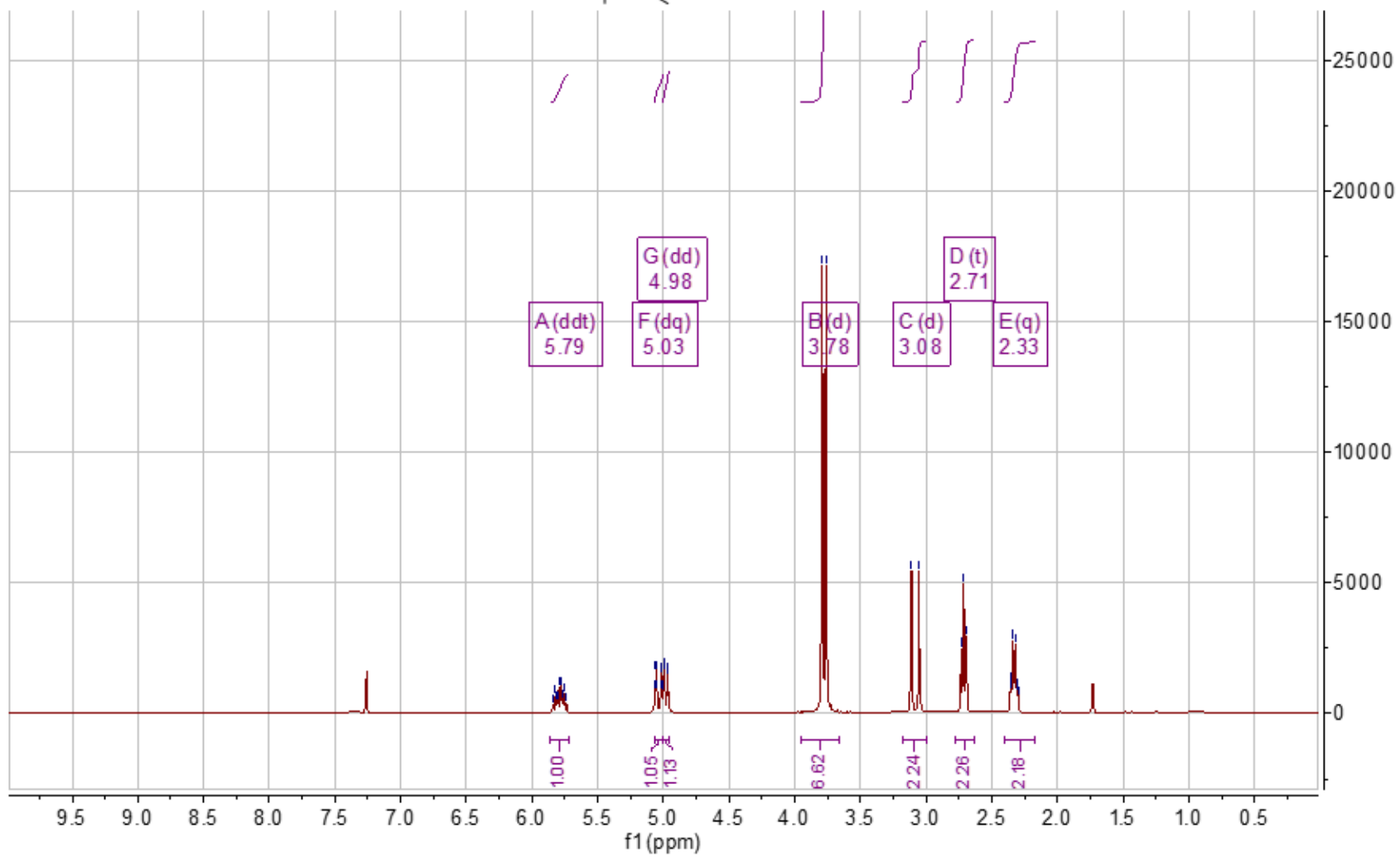
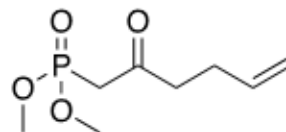


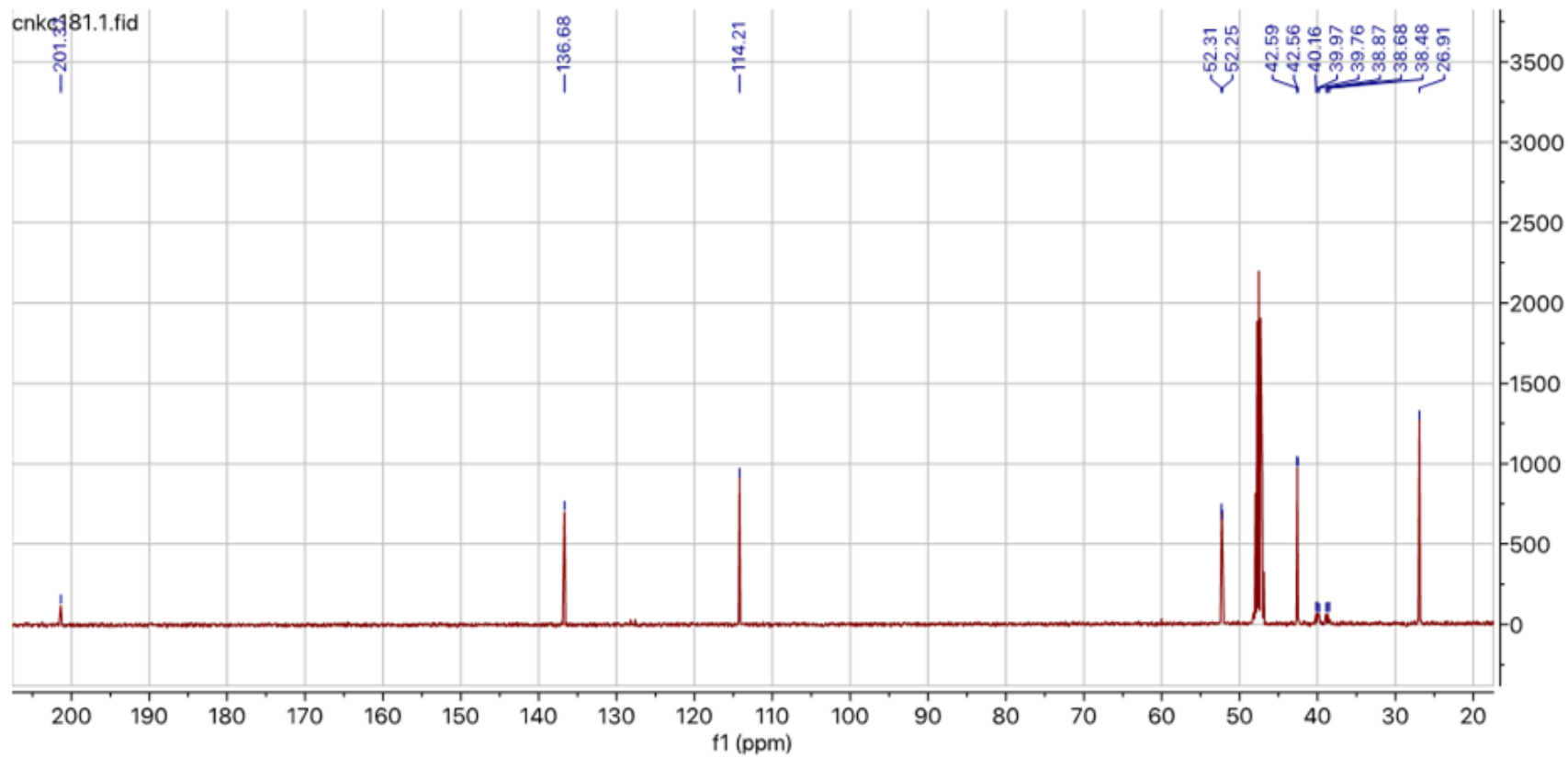
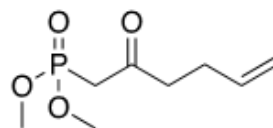
Appendix C

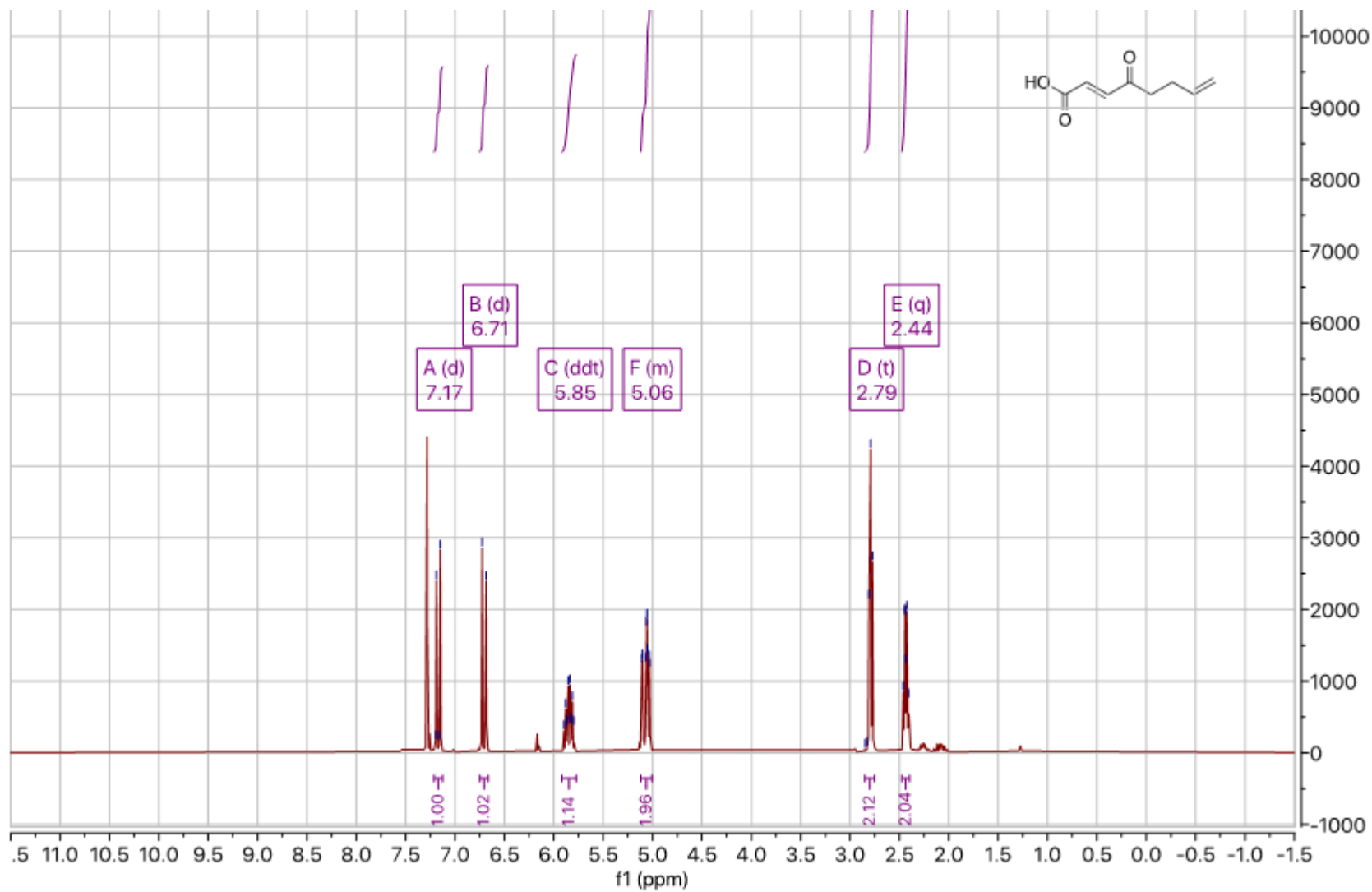
Relevant Spectra to Chapter III

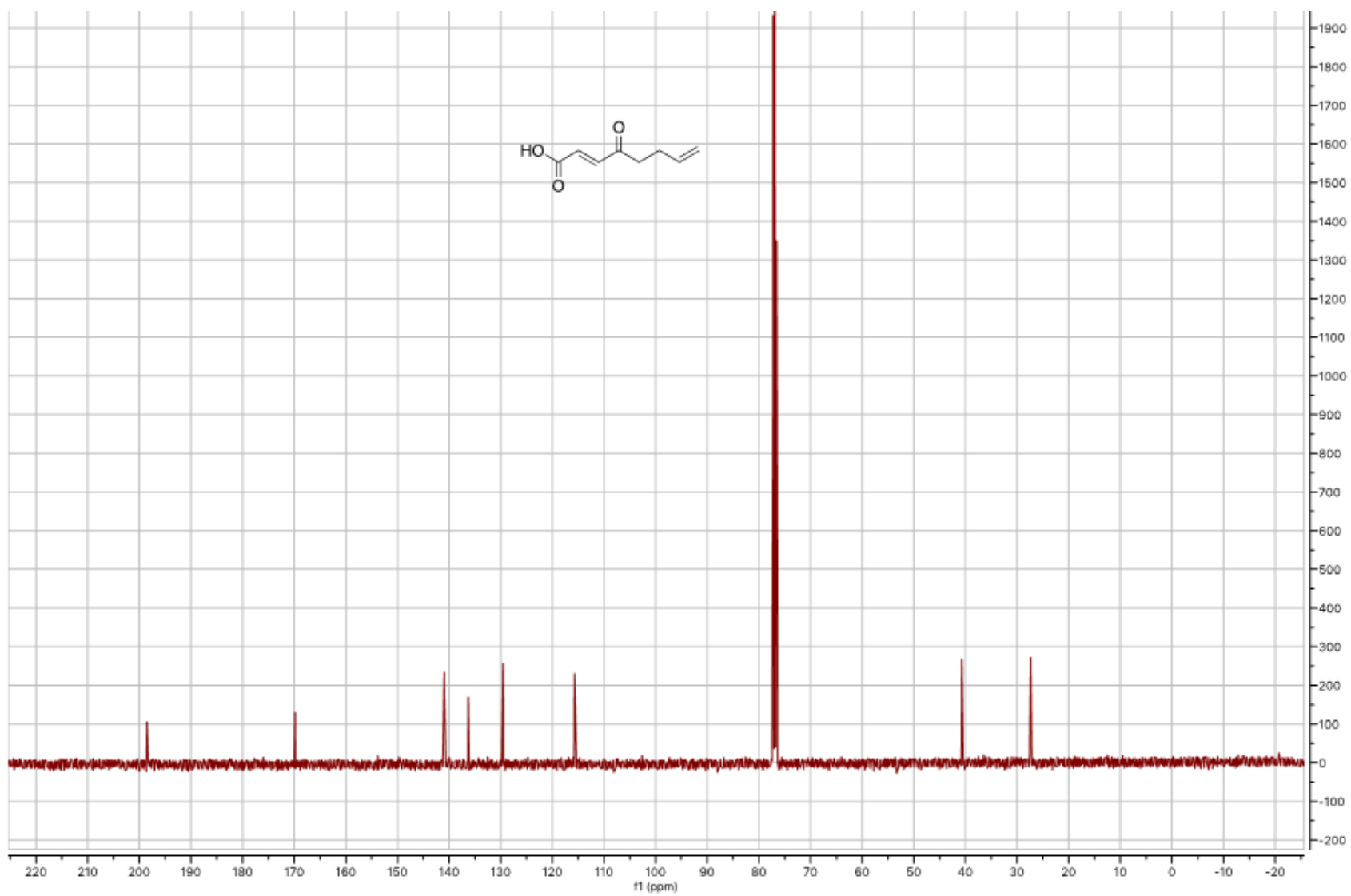


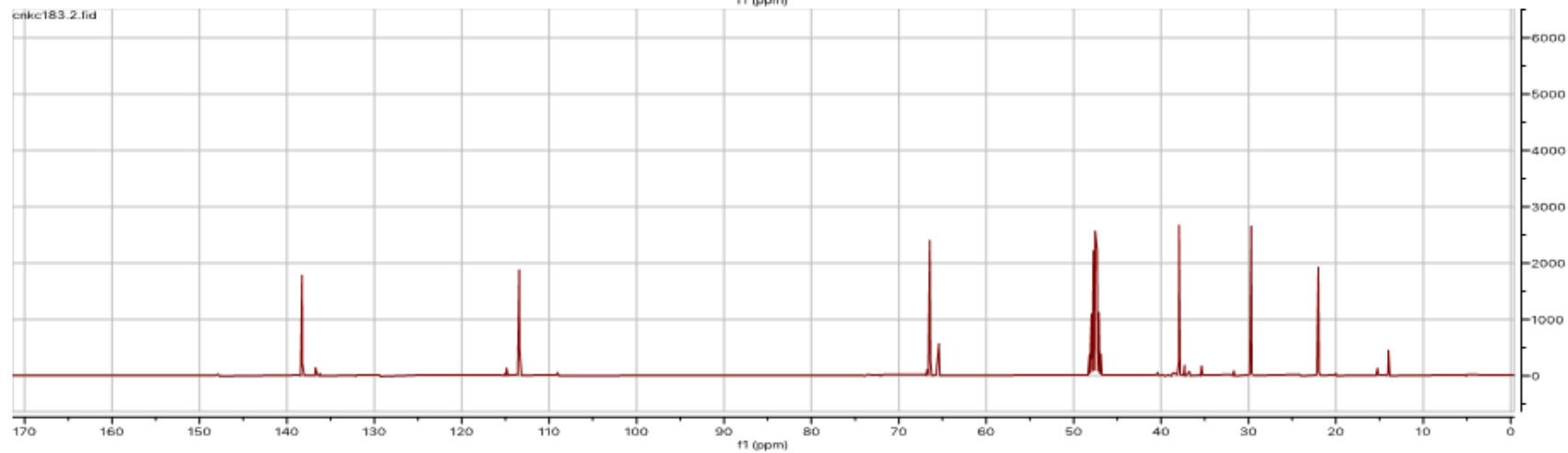
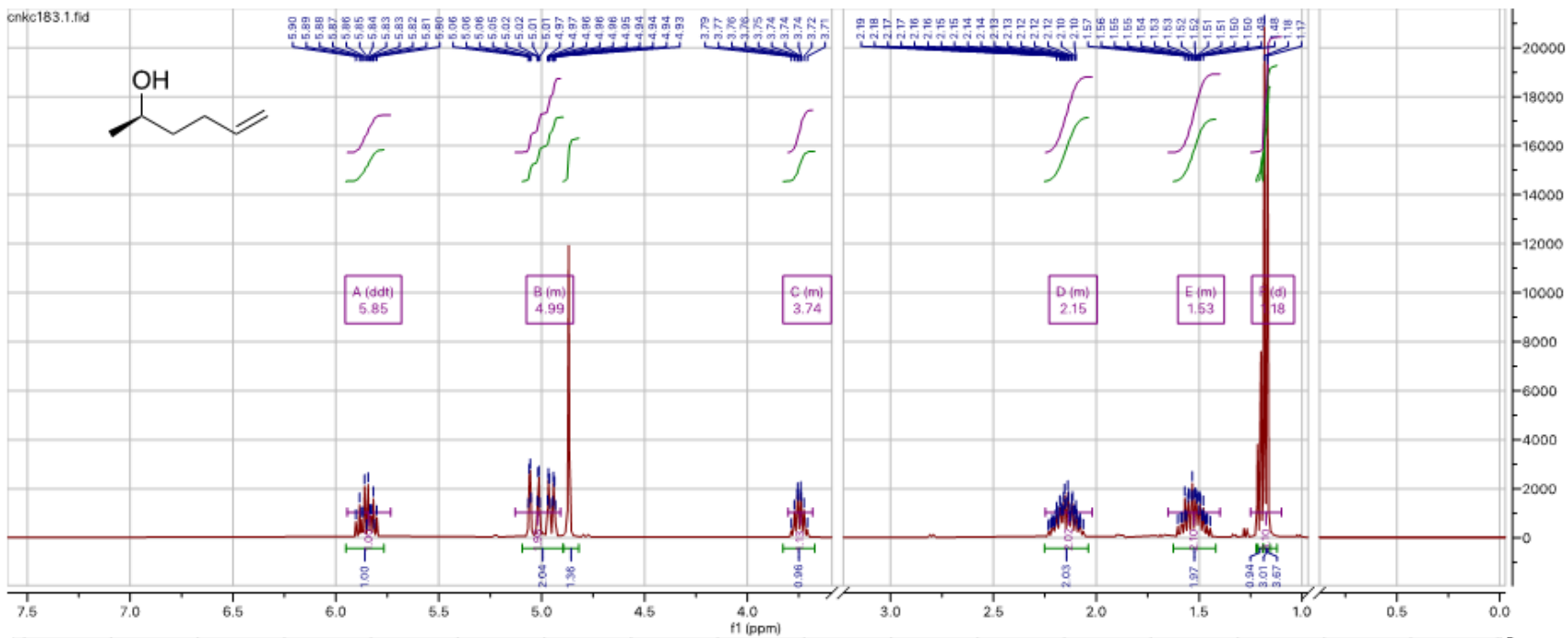


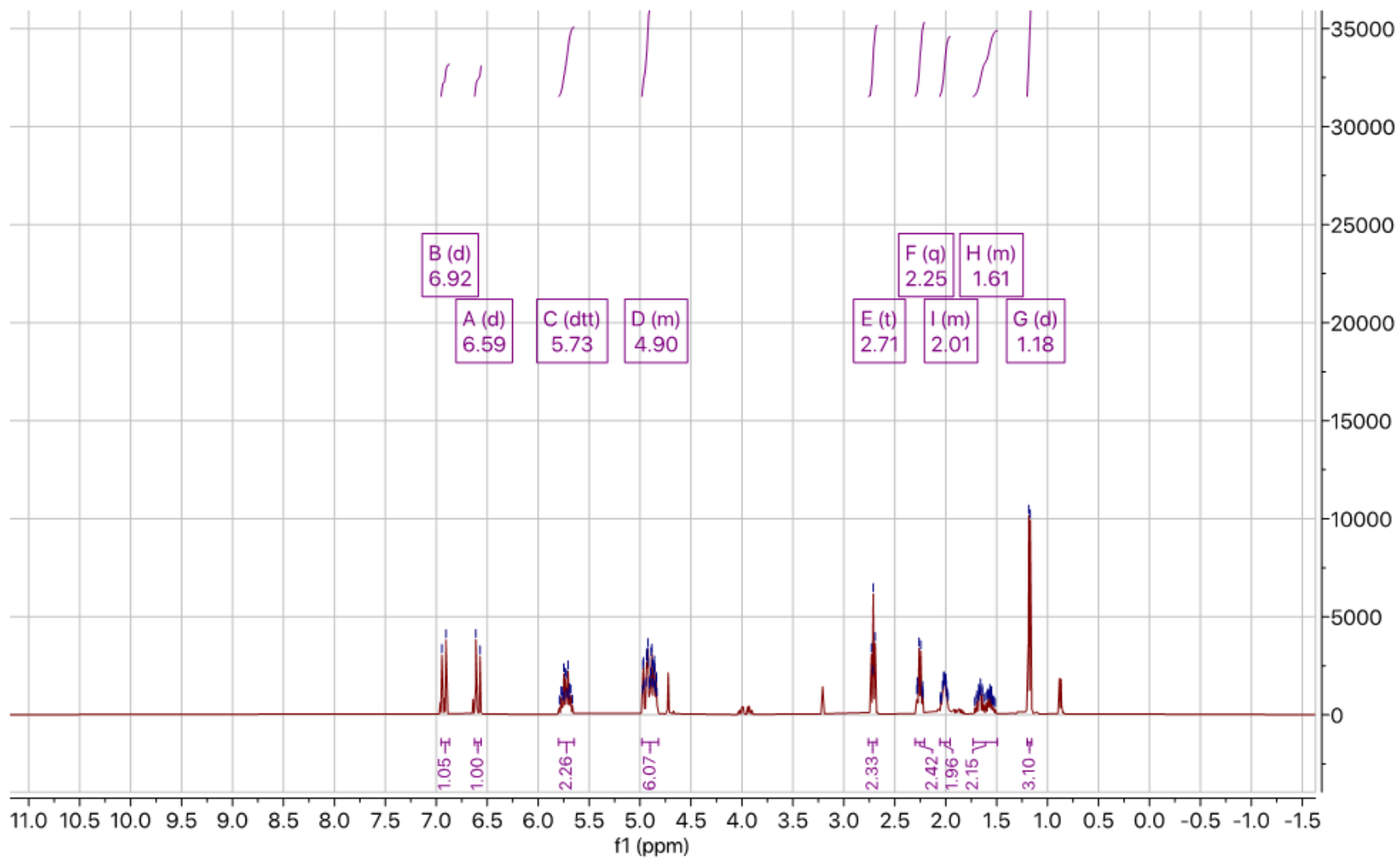
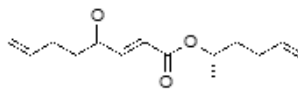


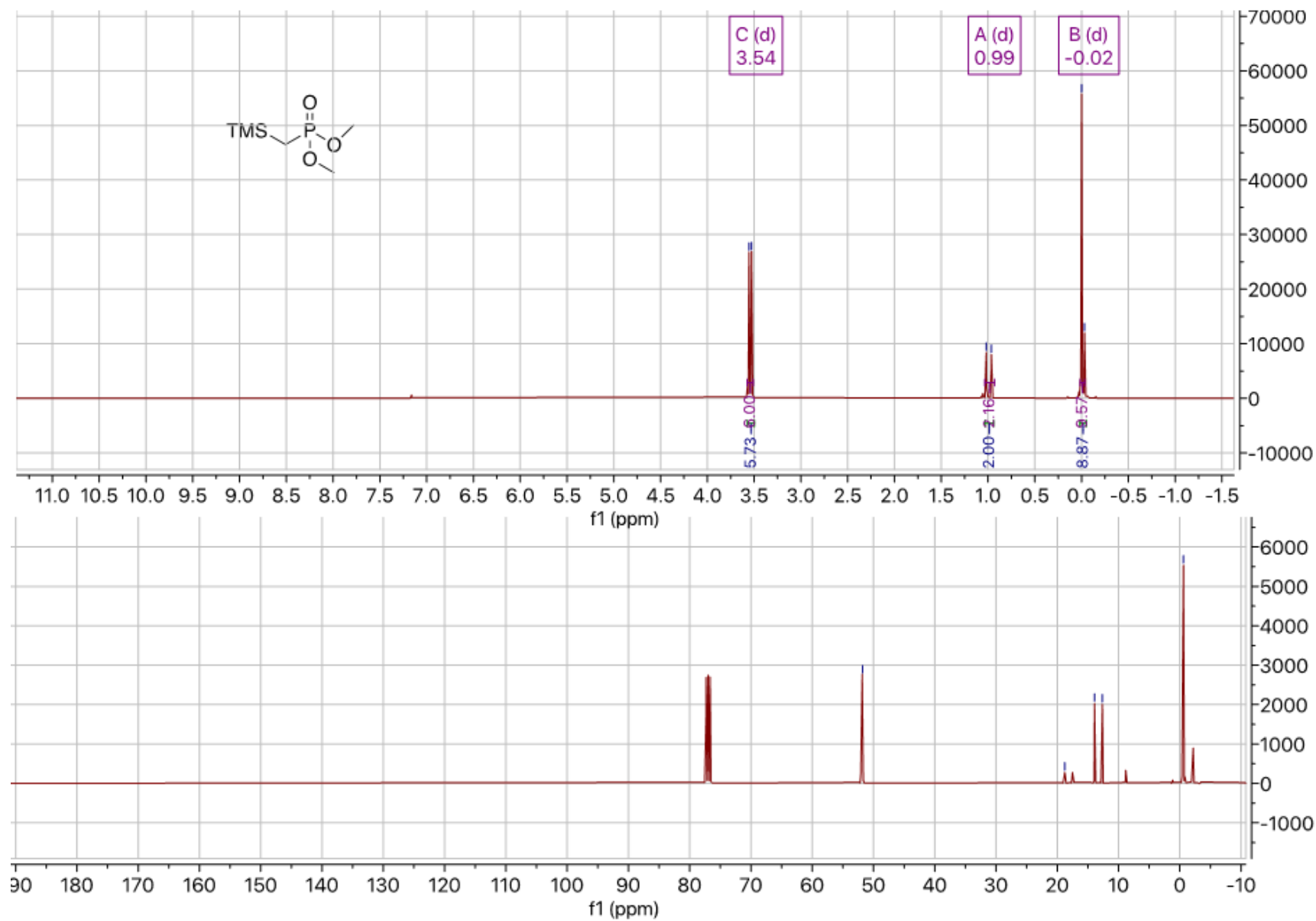


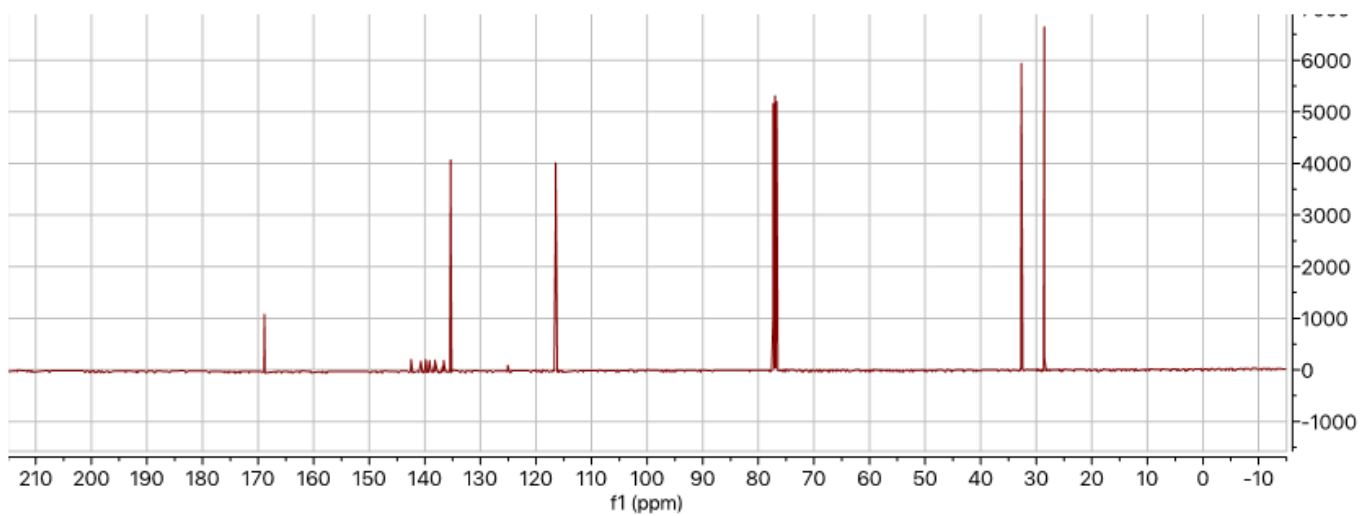
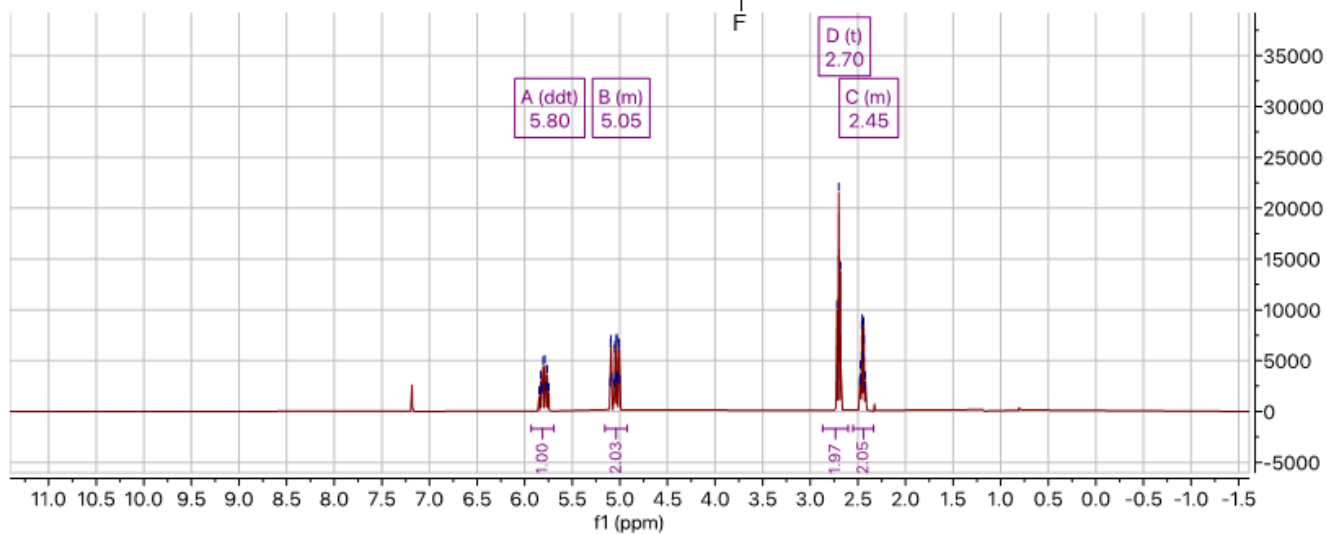
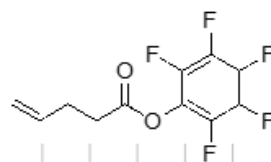


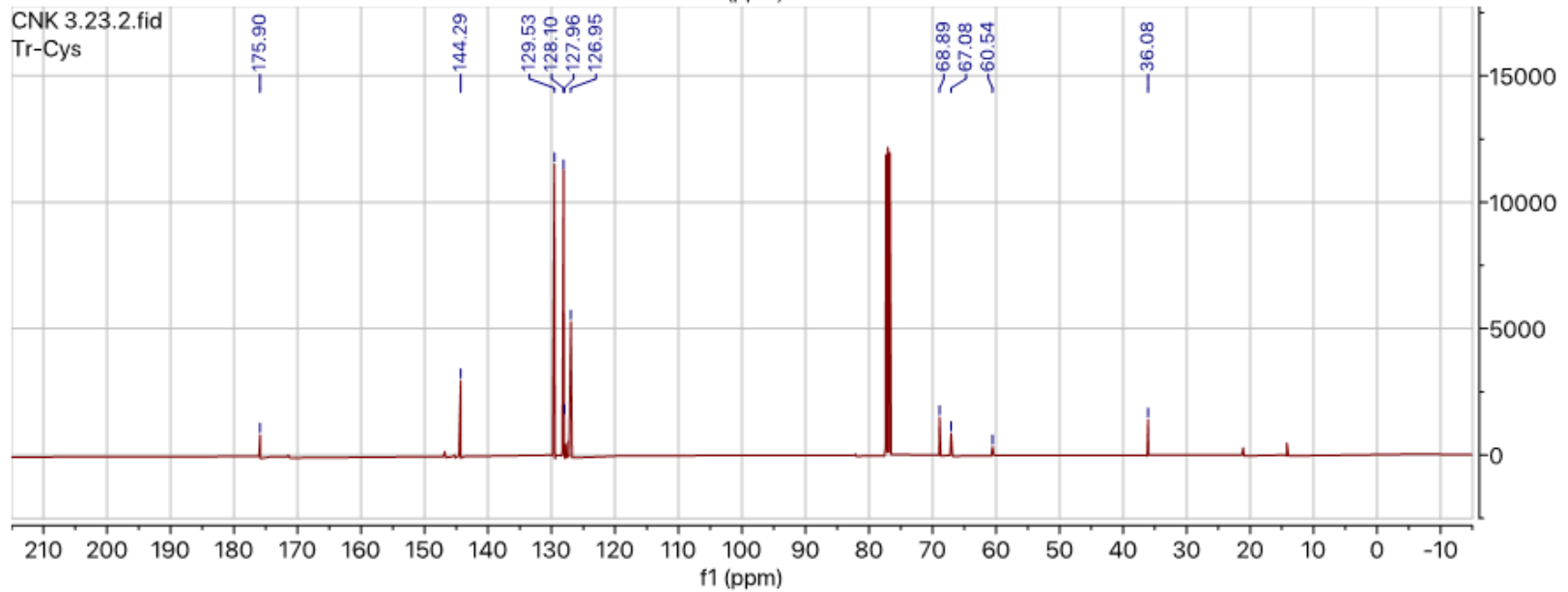
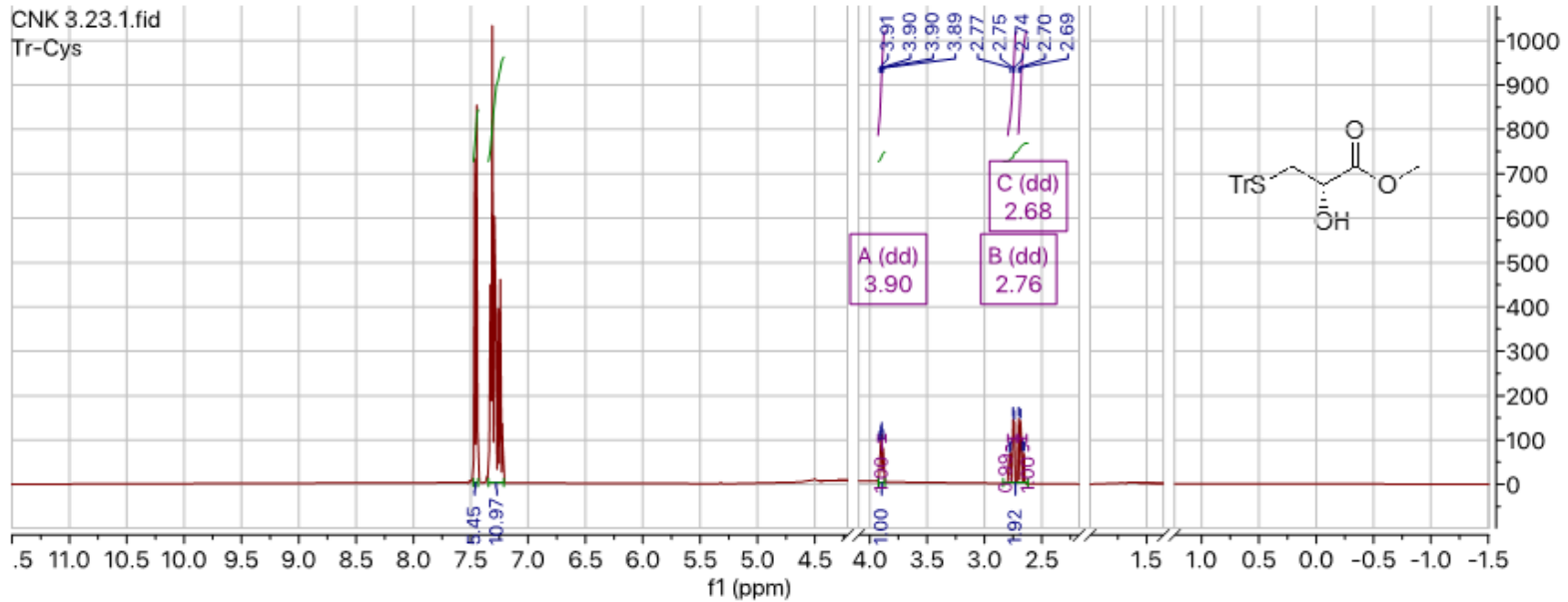


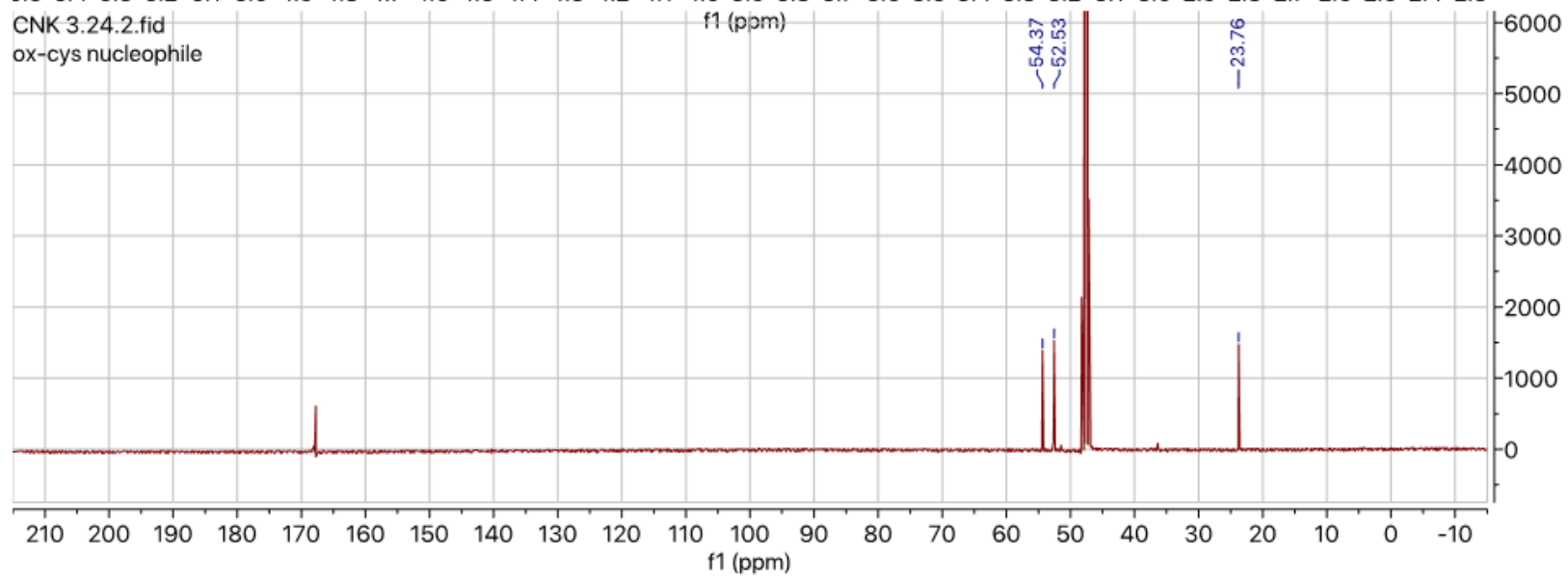
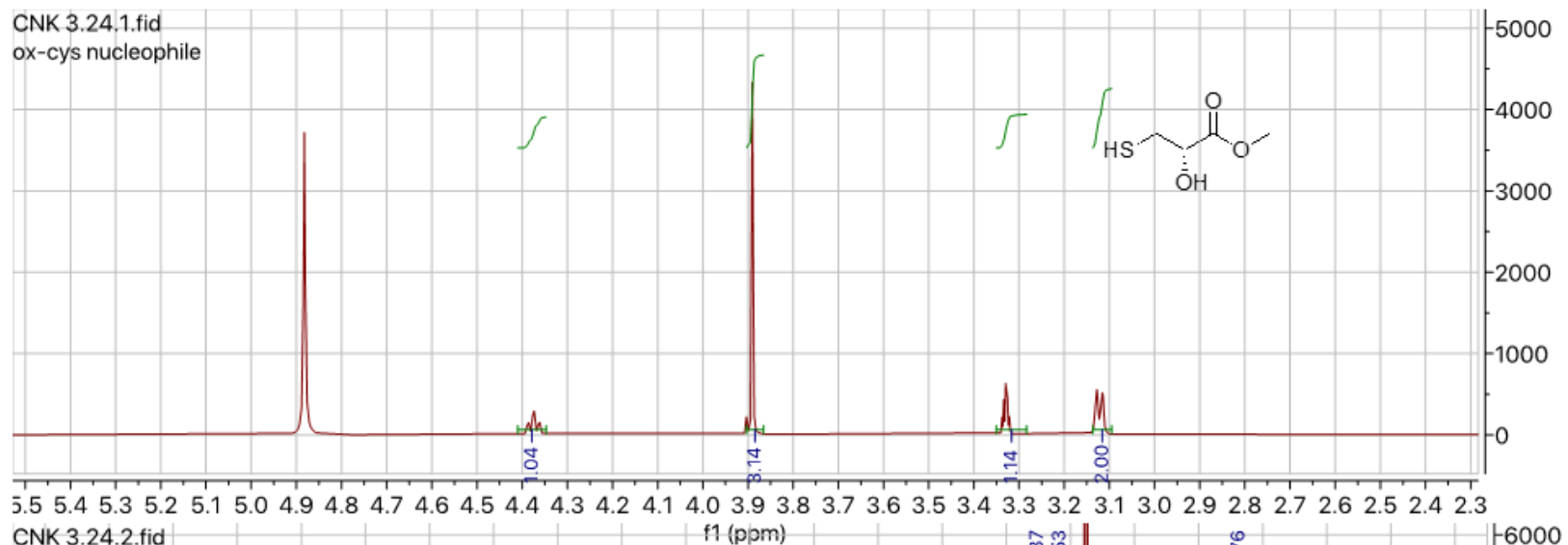












REFERENCES

1. Isacoff, E. Y.; Jan, L. Y.; Minor, D. L., Jr., Conduits of life's spark: a perspective on ion channel research since the birth of neuron. *Neuron* **2013**, *80* (3), 658-674.
2. Hille, B., Ionic channels of excitable membranes. *Sinauer Asso* **1984**.
3. Kuang, Q.; Purhonen, P.; Hebert, H., Structure of potassium channels. *Cell Mol Life Sci* **2015**, *72* (19), 3677-93.
4. Bean, B. P., The action potential in mammalian central neurons. *Nature Reviews Neuroscience* **2007**, *8* (6), 451-465.
5. Jan, L. Y.; Jan, Y. N., Voltage-gated potassium channels and the diversity of electrical signalling. *J Physiol* **2012**, *590* (11), 2591-9.
6. Hagiwara, S., Membrane potential-dependent ion channels in cell membrane. *Phylogenetic and Developmental Approaches* **1983**.
7. Haider, S.; Khalid, S.; Tucker, S. J.; Ashcroft, F. M.; Sansom, M. S., Molecular dynamics simulations of inwardly rectifying (Kir) potassium channels: a comparative study. *Biochemistry* **2007**, *46* (12), 3643-52.
8. Hibino, H.; Inanobe, A.; Furutani, K.; Murakami, S.; Findlay, I.; Kurachi, Y., Inwardly Rectifying Potassium Channels: Their Structure, Function, and Physiological Roles. *Physiological Reviews* **2010**, *90* (1), 291-366.
9. Sakmann, B.; Trube, G., Conductance properties of single inwardly rectifying potassium channels in ventricular cells from guinea-pig heart. *J Physiol* **1984**, *347*, 641-57.

10. Bond, C.; Pessia, M.; Xia, X.; Lagrutta, A.; Kavanaugh, M.; Adelman, J., Cloning and expression of a family of inward rectifier potassium channels. *Receptors & channels* **1994**, 2 (3), 183.
11. Glowatzki, E.; Fakler, G.; Brändle, U.; Rexhausen, U.; Zenner, H. P.; Ruppertsberg, J. P.; Fakler, B., Subunit-dependent assembly of inward-rectifier K⁺ channels. *Proc Biol Sci* **1995**, 261 (1361), 251-61.
12. Schram, G.; Melnyk, P.; Pourrier, M.; Wang, Z.; Nattel, S., Kir2.4 and Kir2.1 K(+) channel subunits co-assemble: a potential new contributor to inward rectifier current heterogeneity. *J Physiol* **2002**, 544 (2), 337-49.
13. Preisig-Müller, R.; Schlichthörl, G.; Goerge, T.; Heinen, S.; Brüggemann, A.; Rajan, S.; Derst, C.; Veh, R. W.; Daut, J., Heteromerization of Kir2.x potassium channels contributes to the phenotype of Andersen's syndrome. *Proc Natl Acad Sci U S A* **2002**, 99 (11), 7774-9.
14. Pessia, M.; Tucker, S. J.; Lee, K.; Bond, C. T.; Adelman, J. P., Subunit positional effects revealed by novel heteromeric inwardly rectifying K⁺ channels. *The EMBO Journal* **1996**, 15 (12), 2980-2987.
15. Abraham, M. R.; Jahangir, A.; Alekseev, A. E.; Terzic, A., Channelopathies of inwardly rectifying potassium channels. *Faseb j* **1999**, 13 (14), 1901-10.
16. Wu, J.-X.; Ding, D.; Wang, M.; Kang, Y.; Zeng, X.; Chen, L., Ligand binding and conformational changes of SUR1 subunit in pancreatic ATP-sensitive potassium channels. *Protein & Cell* **2018**, 9 (6), 553-567.
17. Kharade, S. V.; Kurata, H.; Bender, A. M.; Blobaum, A. L.; Figueroa, E. E.; Duran, A.; Kramer, M.; Days, E.; Vinson, P.; Flores, D.; Satlin, L. M.; Meiler, J.;

- Weaver, C. D.; Lindsley, C. W.; Hopkins, C. R.; Denton, J. S., Discovery, Characterization, and Effects on Renal Fluid and Electrolyte Excretion of the Kir4.1 Potassium Channel Pore Blocker, VU0134992. *Molecular Pharmacology* **2018**, *94* (2), 926-937.
18. Takumi, T.; Ishii, T.; Horio, Y.; Morishige, K.; Takahashi, N.; Yamada, M.; Yamashita, T.; Kiyama, H.; Sohmiya, K.; Nakanishi, S.; et al., A novel ATP-dependent inward rectifier potassium channel expressed predominantly in glial cells. *J Biol Chem* **1995**, *270* (27), 16339-46.
19. Hibino, H.; Fujita, A.; Iwai, K.; Yamada, M.; Kurachi, Y., Differential Assembly of Inwardly Rectifying K⁺ Channel Subunits, Kir4.1 and Kir5.1, in Brain Astrocytes. **2004**, *279* (42), 44065-44073.
20. Kaiser, M.; Maletzki, I.; Hülsmann, S.; Holtmann, B.; Schulz-Schaeffer, W.; Kirchhoff, F.; Bähr, M.; Neusch, C., Progressive loss of a glial potassium channel (KCNJ10) in the spinal cord of the SOD1 (G93A) transgenic mouse model of amyotrophic lateral sclerosis. *J Neurochem* **2006**, *99* (3), 900-12.
21. Newman, E. A., Regional specialization of retinal glial cell membrane. *Nature* **1984**, *309* (5964), 155-7.
22. Pannicke, T.; Uckermann, O.; Iandiev, I.; Biedermann, B.; Wiedemann, P.; Perlman, I.; Reichenbach, A.; Bringmann, A., Altered membrane physiology in Müller glial cells after transient ischemia of the rat retina. *Glia* **2005**, *50* (1), 1-11.
23. Kinboshi, M.; Mukai, T.; Nagao, Y.; Matsuba, Y.; Tsuji, Y.; Tanaka, S.; Tokudome, K.; Shimizu, S.; Ito, H.; Ikeda, A.; Inanobe, A.; Kurachi, Y.; Inoue, S.; Ohno, Y., Inhibition of Inwardly Rectifying Potassium (Kir) 4.1 Channels Facilitates

Brain-Derived Neurotrophic Factor (BDNF) Expression in Astrocytes. *Front Mol Neurosci* **2017**, *10*, 408.

24. Tong, X.; Ao, Y.; Faas, G. C.; Nwaobi, S. E.; Xu, J.; Haustein, M. D.; Anderson, M. A.; Mody, I.; Olsen, M. L.; Sofroniew, M. V.; Khakh, B. S., Astrocyte Kir4.1 ion channel deficits contribute to neuronal dysfunction in Huntington's disease model mice. *Nat Neurosci* **2014**, *17* (5), 694-703.

25. Kahanovitch, U.; Cuddapah, V. A.; Pacheco, N. L.; Holt, L. M.; Mulkey, D. K.; Percy, A. K.; Olsen, M. L., MeCP2 deficiency leads to loss of glial Kir4. 1. *Eneuro* **2018**.

26. Reichold, M.; Zdebik, A. A.; Lieberer, E.; Rapedius, M.; Schmidt, K.; Bandulik, S.; Sterner, C.; Tegtmeyer, I.; Penton, D.; Baukrowitz, T.; Hulton, S. A.; Witzgall, R.; Ben-Zeev, B.; Howie, A. J.; Kleta, R.; Bockenbauer, D.; Warth, R., KCNJ10 gene mutations causing EAST syndrome (epilepsy, ataxia, sensorineural deafness, and tubulopathy) disrupt channel function. **2010**, *107* (32), 14490-14495.

27. Su, X.-T.; Ellison, D. H.; Wang, W.-H., Kir4.1/Kir5.1 in the DCT plays a role in the regulation of renal K(+) excretion. *Am J Physiol Renal Physiol* **2019**, *316* (3), F582-F586.

28. Su, X.-T.; Wang, W.-H., The expression, regulation, and function of Kir4. 1 (Kcnj10) in the mammalian kidney. *American Journal of Physiology-Renal Physiology* **2016**, *311* (1), F12-F15.

29. Thomson, M. N.; Cuevas, C. A.; Bewarder, T. M.; Dittmayer, C.; Miller, L. N.; Si, J.; Cornelius, R. J.; Su, X.-T.; Yang, C.-L.; McCormick, J. A., WNK bodies cluster WNK4 and SPAK/OSR1 to promote NCC activation in hypokalemia. *American Journal of Physiology-Renal Physiology* **2020**, *318* (1), F216-F228.

30. Paulais, M.; Bloch-Faure, M.; Picard, N.; Jacques, T.; Ramakrishnan, S. K.; Keck, M.; Sohet, F.; Eladari, D.; Houillier, P.; Lourdel, S.; Teulon, J.; Tucker, S. J., Renal phenotype in mice lacking the Kir5.1 (Kcnj16) K⁺ channel subunit contrasts with that observed in SeSAME/EAST syndrome. *Proceedings of the National Academy of Sciences* **2011**, *108* (25), 10361-10366.
31. Ohno, Y.; Hibino, H.; Lossin, C.; Inanobe, A.; Kurachi, Y., Inhibition of astroglial Kir4.1 channels by selective serotonin reuptake inhibitors. *Brain Res* **2007**, *1178*, 44-51.
32. Su, S.; Ohno, Y.; Lossin, C.; Hibino, H.; Inanobe, A.; Kurachi, Y., Inhibition of astroglial inwardly rectifying Kir4.1 channels by a tricyclic antidepressant, nortriptyline. *J Pharmacol Exp Ther* **2007**, *320* (2), 573-80.
33. Degorce, S. L.; Bodnarchuk, M. S.; Scott, J. S., Lowering Lipophilicity by Adding Carbon: AzaSpiroHeptanes, a logD Lowering Twist. *ACS Medicinal Chemistry Letters* **2019**, *10* (8), 1198-1204.
34. DeLorbe, J. E.; Clements, J. H.; Teresk, M. G.; Benfield, A. P.; Plake, H. R.; Millspaugh, L. E.; Martin, S. F., Thermodynamic and Structural Effects of Conformational Constraints in Protein–Ligand Interactions. Entropic Paradoxy Associated with Ligand Preorganization. *Journal of the American Chemical Society* **2009**, *131* (46), 16758-16770.
35. Pajouhesh, H.; Lenz, G. R., Medicinal chemical properties of successful central nervous system drugs. *NeuroRx* **2005**, *2* (4), 541-53.
36. Hudspith, M., Glutamate: a role in normal brain function, anaesthesia, analgesia and CNS injury. *British journal of anaesthesia* **1997**, *78* (6), 731-747.

37. Conn, P. J.; Pin, J. P., Pharmacology and functions of metabotropic glutamate receptors. *Annu Rev Pharmacol Toxicol* **1997**, *37*, 205-37.
38. Rosenbaum, D. M.; Rasmussen, S. G.; Kobilka, B. K., The structure and function of G-protein-coupled receptors. *Nature* **2009**, *459* (7245), 356-63.
39. Lv, X.; Liu, J.; Shi, Q.; Tan, Q.; Wu, D.; Skinner, J. J.; Walker, A. L.; Zhao, L.; Gu, X.; Chen, N.; Xue, L.; Si, P.; Zhang, L.; Wang, Z.; Katritch, V.; Liu, Z. J.; Stevens, R. C., In vitro expression and analysis of the 826 human G protein-coupled receptors. *Protein Cell* **2016**, *7* (5), 325-37.
40. Hauser, A. S.; Attwood, M. M.; Rask-Andersen, M.; Schiöth, H. B.; Gloriam, D. E., Trends in GPCR drug discovery: new agents, targets and indications. *Nature Reviews Drug Discovery* **2017**, *16* (12), 829-842.
41. Pin, J. P.; Galvez, T.; Prézeau, L., Evolution, structure, and activation mechanism of family 3/C G-protein-coupled receptors. *Pharmacol Ther* **2003**, *98* (3), 325-54.
42. Gomeza, J.; Joly, C.; Kuhn, R.; Knöpfel, T.; Bockaert, J.; Pin, J. P., The second intracellular loop of metabotropic glutamate receptor 1 cooperates with the other intracellular domains to control coupling to G-proteins. *J Biol Chem* **1996**, *271* (4), 2199-205.
43. Acher, F. C.; Bertrand, H. O., Amino acid recognition by Venus flytrap domains is encoded in an 8-residue motif. *Biopolymers* **2005**, *80* (2-3), 357-66.
44. Coutinho, V.; Knöpfel, T., Metabotropic glutamate receptors: electrical and chemical signaling properties. *Neuroscientist* **2002**, *8* (6), 551-61.

45. Kunishima, N.; Shimada, Y.; Tsuji, Y.; Sato, T.; Yamamoto, M.; Kumasaka, T.; Nakanishi, S.; Jingami, H.; Morikawa, K., Structural basis of glutamate recognition by a dimeric metabotropic glutamate receptor. *Nature* **2000**, *407* (6807), 971-977.
46. Niswender, C. M.; Conn, P. J., Metabotropic glutamate receptors: physiology, pharmacology, and disease. *Annu Rev Pharmacol Toxicol* **2010**, *50*, 295-322.
47. Knöpfel, T.; Uusisaari, M., Modulation of excitation by metabotropic glutamate receptors. *Results Probl Cell Differ* **2008**, *44*, 163-75.
48. Nicoletti, F.; Bockaert, J.; Collingridge, G. L.; Conn, P. J.; Ferraguti, F.; Schoepp, D. D.; Wroblewski, J. T.; Pin, J. P., Metabotropic glutamate receptors: From the workbench to the bedside. *Neuropharmacology* **2011**, *60* (7), 1017-1041.
49. Levitz, J.; Habrian, C.; Bharill, S.; Fu, Z.; Vafabakhsh, R.; Isacoff, E. Y., Mechanism of Assembly and Cooperativity of Homomeric and Heteromeric Metabotropic Glutamate Receptors. *Neuron* **2016**, *92* (1), 143-159.
50. Tuteja, N., Signaling through G protein coupled receptors. *Plant Signal Behav* **2009**, *4* (10), 942-7.
51. Jaffe, D. B.; Brown, T. H., Metabotropic glutamate receptor activation induces calcium waves within hippocampal dendrites. *Journal of Neurophysiology* **1994**, *72* (1), 471-474.
52. Willard, S. S.; Koochekpour, S., Glutamate, glutamate receptors, and downstream signaling pathways. *Int J Biol Sci* **2013**, *9* (9), 948-59.
53. Kim, H. R.; Xu, J.; Maeda, S.; Duc, N. M.; Ahn, D.; Du, Y.; Chung, K. Y., Structural mechanism underlying primary and secondary coupling between GPCRs and the Gi/o family. *Nature Communications* **2020**, *11* (1), 3160.

54. Lindsley, C. W.; Emmitte, K. A.; Hopkins, C. R.; Bridges, T. M.; Gregory, K. J.; Niswender, C. M.; Conn, P. J., Practical Strategies and Concepts in GPCR Allosteric Modulator Discovery: Recent Advances with Metabotropic Glutamate Receptors. *Chemical Reviews* **2016**, *116* (11), 6707-6741.
55. Schoepp, D. D.; Jane, D. E.; Monn, J. A., Pharmacological agents acting at subtypes of metabotropic glutamate receptors. *Neuropharmacology* **1999**, *38* (10), 1431-1476.
56. Jeffrey Conn, P.; Christopoulos, A.; Lindsley, C. W., Allosteric modulators of GPCRs: a novel approach for the treatment of CNS disorders. *Nature Reviews Drug Discovery* **2009**, *8* (1), 41-54.
57. Kelly, E.; Bailey, C. P.; Henderson, G., Agonist-selective mechanisms of GPCR desensitization. *Br J Pharmacol* **2008**, *153 Suppl 1* (Suppl 1), S379-88.
58. Ferguson, S. S.; Barak, L. S.; Zhang, J.; Caron, M. G., G-protein-coupled receptor regulation: role of G-protein-coupled receptor kinases and arrestins. *Canadian journal of physiology and pharmacology* **1996**, *74* (10), 1095-1110.
59. Nestler, E. J.; Aghajanian, G. K., Molecular and cellular basis of addiction. *Science* **1997**, *278* (5335), 58-63.
60. Gainetdinov, R. R.; Premont, R. T.; Bohn, L. M.; Lefkowitz, R. J.; Caron, M. G., Desensitization of G protein-coupled receptors and neuronal functions. *Annu Rev Neurosci* **2004**, *27*, 107-44.
61. Allouche, S.; Noble, F.; Marie, N., Opioid receptor desensitization: mechanisms and its link to tolerance. *Frontiers in Pharmacology* **2014**, *5* (280).

62. Andersen, M. B.; Fink-Jensen, A.; Peacock, L.; Gerlach, J.; Bymaster, F.; Lundbæk, J. A.; Werge, T., The Muscarinic M1/M4 Receptor Agonist Xanomeline Exhibits Antipsychotic-Like Activity in *Cebus apella* Monkeys. *Neuropsychopharmacology* **2003**, *28* (6), 1168-1175.
63. Bradley, S. J.; Molloy, C.; Bundgaard, C.; Mogg, A. J.; Thompson, K. J.; Dwomoh, L.; Sanger, H. E.; Crabtree, M. D.; Brooke, S. M.; Sexton, P. M.; Felder, C. C.; Christopoulos, A.; Broad, L. M.; Tobin, A. B.; Langmead, C. J., Bitopic Binding Mode of an M₁ Muscarinic Acetylcholine Receptor Agonist Associated with Adverse Clinical Trial Outcomes. *Molecular Pharmacology* **2018**, *93* (6), 645-656.
64. Bender, A. M.; Jones, C. K.; Lindsley, C. W., Classics in Chemical Neuroscience: Xanomeline. *ACS Chem Neurosci* **2017**, *8* (3), 435-443.
65. Patel, M. M.; Patel, B. M., Crossing the Blood-Brain Barrier: Recent Advances in Drug Delivery to the Brain. *CNS Drugs* **2017**, *31* (2), 109-133.
66. Bridges, T. M.; Lindsley, C. W., G-Protein-Coupled Receptors: From Classical Modes of Modulation to Allosteric Mechanisms. *ACS Chemical Biology* **2008**, *3* (9), 530-541.
67. Grover, A. K., Use of allosteric targets in the discovery of safer drugs. *Med Princ Pract* **2013**, *22* (5), 418-26.
68. Wenthur, C. J.; Gentry, P. R.; Mathews, T. P.; Lindsley, C. W., Drugs for allosteric sites on receptors. *Annu Rev Pharmacol Toxicol* **2014**, *54*, 165-84.
69. Nussinov, R.; Tsai, C. J., Allostery in disease and in drug discovery. *Cell* **2013**, *153* (2), 293-305.

70. Lane, J. R.; Abdul-Ridha, A.; Canals, M., Regulation of G Protein-Coupled Receptors by Allosteric Ligands. *ACS Chemical Neuroscience* **2013**, *4* (4), 527-534.
71. Möhler, H.; Fritschy, J. M.; Rudolph, U., A new benzodiazepine pharmacology. *J Pharmacol Exp Ther* **2002**, *300* (1), 2-8.
72. López-Muñoz, F.; Alamo, C.; García-García, P., The discovery of chlordiazepoxide and the clinical introduction of benzodiazepines: half a century of anxiolytic drugs. *J Anxiety Disord* **2011**, *25* (4), 554-62.
73. Wang, Q.; Zheng, M.; Huang, Z.; Liu, X.; Zhou, H.; Chen, Y.; Shi, T.; Zhang, J., Toward understanding the molecular basis for chemical allosteric modulator design. *Journal of Molecular Graphics and Modelling* **2012**, *38*, 324-333.
74. Smith, N. J.; Milligan, G., Allosterism at G protein-coupled receptor homo- and heteromers: uncharted pharmacological landscapes. *Pharmacol Rev* **2010**, *62* (4), 701-25.
75. Conn, P. J.; Lindsley, C. W.; Meiler, J.; Niswender, C. M., Opportunities and challenges in the discovery of allosteric modulators of GPCRs for treating CNS disorders. *Nature Reviews Drug Discovery* **2014**, *13* (9), 692-708.
76. Tysnes, O.-B.; Storstein, A., Epidemiology of Parkinson's disease. *Journal of Neural Transmission* **2017**, *124* (8), 901-905.
77. Ascherio, A.; Schwarzschild, M. A., The epidemiology of Parkinson's disease: risk factors and prevention. *The Lancet Neurology* **2016**, *15* (12), 1257-1272.
78. Hopkins, C. R.; Lindsley, C. W.; Niswender, C. M., mGluR4-positive allosteric modulation as potential treatment for Parkinson's disease. *Future Med Chem* **2009**, *1* (3), 501-13.

79. Hacker, M. L.; DeLong, M. R.; Turchan, M.; Heusinkveld, L. E.; Ostrem, J. L.; Molinari, A. L.; Currie, A. D.; Konrad, P. E.; Davis, T. L.; Phibbs, F. T.; Hedera, P.; Cannard, K. R.; Drye, L. T.; Sternberg, A. L.; Shade, D. M.; Tonascia, J.; Charles, D., Effects of deep brain stimulation on rest tremor progression in early stage Parkinson disease. *Neurology* **2018**, *91* (5), e463-e471.
80. Charvin, D.; Medori, R.; Hauser, R. A.; Rascol, O., Therapeutic strategies for Parkinson disease: beyond dopaminergic drugs. *Nature Reviews Drug Discovery* **2018**, *17* (11), 804-822.
81. Bespalov, A.; Miller, R.; Pietraszek, M.; Kalinichev, M.; Doller, D., A case study of foliglurax, the first clinical mGluR4 PAM for symptomatic treatment of Parkinson's disease: Translational gaps or a failing industry innovation model? *Expert Opinion on Investigational Drugs* **2020**, null-null.
82. Whitfield, A. C.; Moore, B. T.; Daniels, R. N., Classics in Chemical Neuroscience: Levodopa. *ACS Chemical Neuroscience* **2014**, *5* (12), 1192-1197.
83. Obeso, J. A.; Rodríguez-Oroz, M. C.; Benitez-Temino, B.; Blesa, F. J.; Guridi, J.; Marin, C.; Rodriguez, M., Functional organization of the basal ganglia: therapeutic implications for Parkinson's disease. *Mov Disord* **2008**, *23 Suppl 3*, S548-59.
84. Lanciego, J. L.; Luquin, N.; Obeso, J. A., Functional neuroanatomy of the basal ganglia. *Cold Spring Harb Perspect Med* **2012**, *2* (12), a009621.
85. Corti, C.; Aldegheri, L.; Somogyi, P.; Ferraguti, F., Distribution and synaptic localisation of the metabotropic glutamate receptor 4 (mGluR4) in the rodent CNS. *Neuroscience* **2002**, *110* (3), 403-20.

86. Valenti, O.; Mannaioni, G.; Seabrook, G. R.; Conn, P. J.; Marino, M. J., Group III metabotropic glutamate-receptor-mediated modulation of excitatory transmission in rodent substantia nigra pars compacta dopamine neurons. *Journal of Pharmacology and Experimental Therapeutics* **2005**, *313* (3), 1296-1304.
87. Betts, M. J.; O'Neill, M. J.; Duty, S., Allosteric modulation of the group III mGlu4 receptor provides functional neuroprotection in the 6-hydroxydopamine rat model of Parkinson's disease. *Br J Pharmacol* **2012**, *166* (8), 2317-30.
88. Kalinichev, M.; Le Poul, E.; Boléa, C.; Girard, F.; Campo, B.; Fonsi, M.; Royer-Urios, I.; Browne, S. E.; Uslaner, J. M.; Davis, M. J.; Raber, J.; Duvoisin, R.; Bate, S. T.; Reynolds, I. J.; Poli, S.; Celanire, S., Characterization of the novel positive allosteric modulator of the metabotropic glutamate receptor 4 ADX88178 in rodent models of neuropsychiatric disorders. *J Pharmacol Exp Ther* **2014**, *350* (3), 495-505.
89. Ossowska, K.; Wardas, J.; Berghauzen-Maciejewska, K.; Głowacka, U.; Kuter, K.; Pilc, A.; Zorn, S. H.; Doller, D., Lu AF21934, a positive allosteric modulator of mGlu4 receptors, reduces the harmaline-induced hyperactivity but not tremor in rats. *Neuropharmacology* **2014**, *83*, 28-35.
90. Engers, D. W.; Jones, C. K.; Bubser, M.; Thompson, A. D.; Blobaum, A. L.; Sheffler, D. J.; Zamorano, R.; Carrington, S. J. S.; Bridges, T. M.; Morrison, R. D.; Daniels, J. S.; Conn, P. J.; Lindsley, C. W.; Niswender, C. M.; Hopkins, C. R., Discovery of a novel metabotropic glutamate receptor 4 (mGlu(4)) positive allosteric modulator (PAM) extended probe: Characterization of ML292, a potent and selective mGlu(4) PAM which produces efficacy alone or in combination with L-DOPA in preclinical rodent models of Parkinson's disease. In *Probe Reports from the NIH*

Molecular Libraries Program, National Center for Biotechnology Information (US): Bethesda (MD), 2010.

91. Charvin, D.; Pomel, V.; Ortiz, M.; Frauli, M.; Scheffler, S.; Steinberg, E.; Baron, L.; Deshons, L.; Rudigier, R.; Thiarç, D.; Morice, C.; Manteau, B.; Mayer, S.; Graham, D.; Giethlen, B.; Brugger, N.; Hédou, G.; Conquet, F.; Schann, S., Discovery, Structure–Activity Relationship, and Antiparkinsonian Effect of a Potent and Brain-Penetrant Chemical Series of Positive Allosteric Modulators of Metabotropic Glutamate Receptor 4. *Journal of Medicinal Chemistry* **2017**, *60* (20), 8515-8537.
92. Zoller, G.; Anagnostopulos, H. Preparation of 5-oxoperhydro-1,4-thiazepine-3-carboxylates as mucolytics and bronchospasmolytics. DE3801404A1, 1989.
93. Blondeau, P.; Gauthier, R.; Berse, C.; Gravel, D., Synthesis of stable 7-halo-1,4-thiazepines. Potential substituted penam precursors. *Can. J. Chem.* **1971**, *49* (23), 3866-76.
94. Wang, J.; Li, B.; Zhao, W.; Zhang, X.; Luo, X.; Corkins, M. E.; Cole, S. L.; Wang, C.; Xiao, Y.; Bi, X.; Pang, Y.; McElroy, C. A.; Bird, A. J.; Dong, Y., Two-Photon Near Infrared Fluorescent Turn-On Probe Toward Cysteine and Its Imaging Applications. *ACS Sens.* **2016**, *1* (7), 882-887.
95. Strongin, R. M.; Guo, Y.; Hakuna, L.; Lowry, M. A.; Escobedo Cordova, J. O. Selective detection of thiols. US20150010938A1, 2015.
96. Liu, H.; Wang, X.; Xiang, Y.; Tong, A., Fluorescence turn-on detection of cysteine over homocysteine and glutathione based on "ESIPT" and "AIE". *Anal. Methods* **2015**, *7* (12), 5028-5033.

97. He, X.; Wu, Y.; Jin, W.; Wang, X.; Wu, C.; Shang, Y., Highly efficient AgNO₃-catalyzed approach to 2-(benzo[d]azol-2-yl)phenols from salicylaldehydes with 2-aminothiophenol, 2-aminophenol and benzene-1,2-diamine. *Appl. Organomet. Chem.* **2018**, 32 (4), n/a.
98. Yang, X.; Guo, Y.; Strongin, R. M., Conjugate Addition/Cyclization Sequence Enables Selective and Simultaneous Fluorescence Detection of Cysteine and Homocysteine. *Angew. Chem., Int. Ed.* **2011**, 50 (45), 10690-10693, S10690/1-S10690/28.
99. Prachayasittikul, V.; Prachayasittikul, V., P-glycoprotein transporter in drug development. *Excli j* **2016**, 15, 113-8.
100. Hansch, C.; Rockwell, S. D.; Jow, P. Y. C.; Leo, A.; Steller, E. E., Substituent constants for correlation analysis. *Journal of Medicinal Chemistry* **1977**, 20 (2), 304-306.
101. Pingale, T.; Gupta, G. L., Classic and evolving animal models in Parkinson's disease. *Pharmacology Biochemistry and Behavior* **2020**, 199, 173060.
102. Jones, C. K.; Bubser, M.; Thompson, A. D.; Dickerson, J. W.; Turle-Lorenzo, N.; Amalric, M.; Blobaum, A. L.; Bridges, T. M.; Morrison, R. D.; Jadhav, S.; Engers, D. W.; Italiano, K.; Bode, J.; Daniels, J. S.; Lindsley, C. W.; Hopkins, C. R.; Conn, P. J.; Niswender, C. M., The metabotropic glutamate receptor 4-positive allosteric modulator VU0364770 produces efficacy alone and in combination with L-DOPA or an adenosine 2A antagonist in preclinical rodent models of Parkinson's disease. *J Pharmacol Exp Ther* **2012**, 340 (2), 404-21.
103. Katz, L.; Baltz, R. H., Natural product discovery: past, present, and future. *J Ind Microbiol Biotechnol* **2016**, 43 (2-3), 155-76.

104. Newman, D. J.; Cragg, G. M., Natural Products as Sources of New Drugs from 1981 to 2014. *J Nat Prod* **2016**, *79* (3), 629-61.
105. Rossiter, S. E.; Fletcher, M. H.; Wuest, W. M., Natural Products as Platforms To Overcome Antibiotic Resistance. *Chem Rev* **2017**, *117* (19), 12415-12474.
106. Hutchings, M. I.; Truman, A. W.; Wilkinson, B., Antibiotics: past, present and future. *Curr Opin Microbiol* **2019**, *51*, 72-80.
107. Levy, S. B.; Marshall, B., Antibacterial resistance worldwide: causes, challenges and responses. *Nature medicine* **2004**, *10* (12), S122-S129.
108. Brown, E. D.; Wright, G. D., Antibacterial drug discovery in the resistance era. *Nature* **2016**, *529* (7586), 336-43.
109. Božena, D. K.; Iwona, D.; Ilona, K., The mycobiome – a friendly cross-talk between fungal colonizers and their host. *Ann Parasitol* **2016**, *62* (3), 175–184.
110. Keller, N. P., Fungal secondary metabolism: regulation, function and drug discovery. *Nat Rev Microbiol* **2019**, *17* (3), 167-180.
111. Smith, C. J.; Abbanat, D.; Bernan, V. S.; Maiese, W. M.; Greenstein, M.; Jompa, J.; Tahir, A.; Ireland, C. M., Novel polyketide metabolites from a species of marine fungi. *J Nat Prod* **2000**, *63* (1), 142-5.
112. Clevenger, K. D.; Bok, J. W.; Ye, R.; Miley, G. P.; Verdán, M. H.; Velk, T.; Chen, C.; Yang, K.; Robey, M. T.; Gao, P.; Lamprecht, M.; Thomas, P. M.; Islam, M. N.; Palmer, J. M.; Wu, C. C.; Keller, N. P.; Kelleher, N. L., A scalable platform to identify fungal secondary metabolites and their gene clusters. *Nat Chem Biol* **2017**, *13* (8), 895-901.

113. Ferko, B.; Zeman, M.; Formica, M.; Veselý, S.; Doháňošová, J.; Moncol, J.; Olejníková, P.; Berkeš, D.; Jakubec, P.; Dixon, D. J.; Caletková, O., Total Synthesis of Berkeleylactone A. *J Org Chem* **2019**, *84* (11), 7159-7165.
114. Stierle, A. A.; Stierle, D. B.; Decato, D.; Priestley, N. D.; Alverson, J. B.; Hoody, J.; McGrath, K.; Klepacki, D., The Berkeleylactones, Antibiotic Macrolides from Fungal Coculture. *J Nat Prod* **2017**, *80* (4), 1150-1160.
115. Huang, C.; Chen, T.; Yan, Z.; Guo, H.; Hou, X.; Jiang, L.; Long, Y., Thiocladospolide E and cladospamide A, novel 12-membered macrolide and macrolide lactam from mangrove endophytic fungus *Cladosporium* sp. SCNU-F0001. *Fitoterapia* **2019**, *137*, 104246.
116. Zhang, F. Z.; Li, X. M.; Yang, S. Q.; Meng, L. H.; Wang, B. G., Thiocladospolides A-D, 12-Membered Macrolides from the Mangrove-Derived Endophytic Fungus *Cladosporium cladosporioides* MA-299 and Structure Revision of Pandangolide 3. *J Nat Prod* **2019**, *82* (6), 1535-1541.
117. Ronsheim, M. D.; Zercher, C. K., Ring expansions of beta-keto lactones with zinc carbenoids: syntheses of (+)-patulolide A and (+/-)-patulolide B. *J Org Chem* **2003**, *68* (5), 1878-85.
118. Kobayashi, Y.; Nakano, M.; Kumar, G. B.; Kishihara, K., Efficient Conditions for Conversion of 2-Substituted Furans into 4-Oxygenated 2-Enoic Acids and Its Application to Synthesis of (+)-Aspicilin, (+)-Patulolide A, and (-)-Pyrenophorin. *J Org Chem* **1998**, *63* (21), 7505-7515.
119. Sharma, A.; Sankaranarayanan, S.; Chattopadhyay, S., Expedient Synthesis of (R)-Patulolide A. *J Org Chem* **1996**, *61* (5), 1814-1816.

120. Makita, A.; Yamada, Y.; Okada, H., The total synthesis of (+/-)-patulolide A. *J Antibiot (Tokyo)* **1986**, 39 (9), 1257-62.
121. Krenske, E. H.; Petter, R. C.; Houk, K. N., Kinetics and Thermodynamics of Reversible Thiol Additions to Mono- and Diactivated Michael Acceptors: Implications for the Design of Drugs That Bind Covalently to Cysteines. *The Journal of Organic Chemistry* **2016**, 81 (23), 11726-11733.
122. Trnka, T. M.; Grubbs, R. H., The Development of L2X2RuCHR Olefin Metathesis Catalysts: An Organometallic Success Story. *Accounts of Chemical Research* **2001**, 34 (1), 18-29.
123. Neises, B.; Steglich, W., Simple Method for the Esterification of Carboxylic Acids. *Angewandte Chemie International Edition in English* **1978**, 17 (7), 522-524.
124. Leijondahl, K.; Borén, L.; Braun, R.; Bäckvall, J. E., Enzyme- and ruthenium-catalyzed dynamic kinetic asymmetric transformation of 1,5-diols. Application to the synthesis of (+)-Solenopsin A. *J Org Chem* **2009**, 74 (5), 1988-93.
125. Annangudi, S. P.; Sun, M.; Salomon, R. G., An efficient synthesis of 4-oxoalkenoic acids from 2-alkylfurans. *Synlett* **2005**, (9), 1468-1470.
126. Sivák, I.; Václav, J.; Berkeš, D.; Kolarovič, A., Straightforward synthesis of functionalized (E)-3-acylacrylic acids. *Tetrahedron* **2015**, 71 (47), 8876-8884.
127. Specklin, S.; Cossy, J., Chemoselective synthesis of β -ketophosphonates using lithiated α -(trimethylsilyl)methylphosphonate. *J Org Chem* **2015**, 80 (6), 3302-8.
128. Grayson, M. N.; Houk, K. N., Cinchona Urea-Catalyzed Asymmetric Sulfa-Michael Reactions: The Brønsted Acid-Hydrogen Bonding Model. *Journal of the American Chemical Society* **2016**, 138 (29), 9041-9044.

CAITLIN N. KENT

Scientist, Sanofi

caitlin.n.kent@vanderbilt.edu

617-312-4949

EDUCATION

Vanderbilt University, Nashville, TN

Doctorate of Philosophy, Chemistry, GPA: 3.88

Defense: November 24th 2020

The University of Kansas, Lawrence, KS

Master of Science, Medicinal Chemistry, GPA: 3.88

August 2017

University of Saint Joseph, West Hartford, CT

Bachelor of Science, Chemistry and Biology, GPA: 3.63

May 2015

RESEARCH EXPERIENCE

Sanofi, Integrated Drug Discovery, Waltham, MA

Scientist, Medicinal Chemistry, November 2020 - Present

Vanderbilt University, Department of Chemistry, Nashville, TN

Advisor: Craig Lindsley, Ph.D.

Graduate Research Assistant, June 2019 – November 2020

Total syntheses of Thiocladospolide analogues (natural and unnatural) as antibiotic agents, development of chemical methods to generate imidazo[1,2-a]pyridines, and the synthesis of small molecule allosteric modulators of GPCRs with therapeutic relevance.

Vanderbilt Center for Neuroscience Drug Discovery, Nashville, TN

Advisor: Bruce Melancon, Ph.D. and Craig Lindsley, Ph.D.

Research Assistant I, February 2019 – June 2019

Development of allosteric modulators of GPCRs with therapeutic relevance.

University of Notre Dame, Department of Chemistry and Biochemistry, South Bend, IN

Department of Medicinal Chemistry, The University of Kansas, Lawrence, KS

Advisor: Brian S.J. Blagg, Ph.D.

Graduate Research Assistant, August 2015 – January 2019

Design, synthesis, and biological evaluation of isoform-selective inhibitors of the Hsp90 N-terminus via structure-guided design, and the evaluation these tool compounds at the genomic and proteomic level to determine their therapeutic potential.

Department of Biology, University of Saint Joseph, West Hartford, CT.

Advisor: Irene G. Reed, Ph.D.

Undergraduate Researcher,

Research supports a hypothesis in which estrogen-dependent endometrial cancer undergoes epithelial-to-mesenchymal transition to suppress expression of the estrogen receptor, but remain estrogen-responsive via GPCR30.

PUBLICATIONS

5. Kent CN, Park C, Lindsley CW. "Classics in Chemical Neuroscience: Baclofen." *ACS Chemical Neuroscience* (2020).
4. Que NL, Crowley VM, Duerfeldt AS, Zhao J, **Kent CN**, Blagg BS, Gewirth DT. Structure based design of a Grp94-selective inhibitor: exploiting a key residue in Grp94 to optimize paralog-selective binding. *Journal of Medicinal Chemistry*. 2018 Mar 12;61(7):2793-805. doi:10.1021/acs.jmedchem.7b01608
3. Khandelwal A, **Kent CN**, Balch M, Peng S, Mishra SJ, Deng J, Day VW, Liu W, Subramanian C, Cohen M, Holzbeierlein JM. Structure-guided design of an Hsp90beta N-terminal isoform-selective inhibitor. *Nature Communications*. 2018 Jan;9. doi:10.1038/s41467-017-02013-1
2. Byrd KM, **Kent CN**, Blagg BS. Synthesis and Biological Evaluation of Stilbene Analogues as Hsp90 C-Terminal Inhibitors. *ChemMedChem*. 2017 Dec 19;12(24):2022-9. doi:10.1002/cmdc.201700630
1. **Kent CN**, Reed IG. Regulation of epithelial–mesenchymal transition in endometrial cancer: connecting PI3K, estrogen signaling, and microRNAs. *Clinical and Translational Oncology*. 2016 Nov;18(11):1056-61. doi:10.1007/s12094-016-1492-2

PATENTS

1. Blagg, Brian S. J.; Kent, Caitlin N.; Khandelwal, Anuj; Mishra, Sanket J. HSP90B N-TERMINAL ISOFORM SELECTIVE INHIBITORS, US Patent App. 16/477, 398, 2019.

PRESENTATIONS

8. **Caitlin N. Kent**, Sanket J. Mishra, Brian S.J. Blagg. Development and Characterization of Hsp90β Nterminal Isoform-selective Inhibitors. Poster, International Hsp90 Symposium, Leysin, Switzerland, Oct 2018.
7. **Caitlin N. Kent**. Development of Hsp90 N-terminal Isoform-selective Inhibitors. Oral Presentation, University of Notre Dame, March 2018.
6. **Caitlin N. Kent**. Development of Hsp90 N-terminal Isoform-selective Inhibitors. Oral Presentation, Chemical Biology Training Grant Symposium, The University of Kansas, March 2017.
5. **Caitlin N. Kent**. Sanket J. Mishra, Brian S.J. Blagg. Development and Characterization of Hsp90β Nterminal Isoform-selective Inhibitors. Poster, Chemical Biology Training Grant Symposium, The University of Kansas, March 2017.
4. **Caitlin N. Kent**. Regulation of Epithelial-Mesenchymal Transition in Endometrial Cancer. Oral Presentation, Beta Beta Beta Biological Honors Society Regional Conference, West Hartford, CT, May 2015.
3. **Caitlin N. Kent**. Regulation of Epithelial-Mesenchymal Transition in Endometrial Cancer. Oral Presentation, University of Saint Joseph Symposium Day, West Hartford, CT. May 2015.
2. **Caitlin N. Kent**. Pd-Catalyzed Amination of Arylhalides towards Efficient Synthesis of Sterically Demanding N-Arylpiperazines. Oral Presentation, University of St. Joseph Symposium Day, West Hartford, CT. May 2014.
1. **Caitlin N. Kent**, Steven W. Goldstein, Ola Ghoneim. Pd-Catalyzed Amination of Arylhalides towards Efficient Synthesis of Sterically Demanding N-Arylpiperazines. Poster, American Chemical Society North Eastern Regional Meeting, New Haven, CT, Oct 2013.

HONORS AND FELLOWSHIPS

July 2018 – Feb 2019 **Chemical Biology and Biochemistry Fellow**, NIH T32, Notre Dame, IN

July 2016 – July 2017 **Dynamic Aspects of Chemical Biology Fellow**, NIH T32, Lawrence, KS

Aug 2015 – May 2016 **University Graduate Fellow**, University of Kansas, Lawrence, KS

Aug 2015 – May 2016 **Edward E. Smissman Fellow**, University of Kansas, Lawrence, KS

May 2015 **Frank G. Brooks Award**, TriBeta National Biological Honors Society, NE Regional Section

- First place oral presentation, New England Regional Conference

May 2015 **Founder's Award**, Research in Biological Sciences, University of Saint Joseph, West Hartford, CT

May 2014 **Leadership in Biology Award**, University of Saint Joseph, West Hartford, CT

May 2014 **Outstanding Senior in Organic Chemistry Award**, ACS Connecticut Valley Section

May 2014 **Outstanding Performance in Chemistry Award**, ACS Connecticut Valley Section

INVITED SPEAKING ENGAGEMENTS

President's Circle Impact Lectures, University of Notre Dame, February 2018.

<https://www.youtube.com/watch?v=PdZ0s0gBvWM>

University of Saint Joseph Gala, The Sky's the Limit, July 2015.

<https://www.youtube.com/watch?v=XBKpXue6RLs>

University of Saint Joseph, Undergraduate Commencement Speaker, May 2015.

RELEVANT LEADERSHIP POSITIONS

2018-2019 Association of Women in Science

- Treasurer, University of Notre Dame, South Bend, IN.

2016-2017 Graduate Student Department Representative,

- Department of Medicinal Chemistry, The University of Kansas, Lawrence, KS.

2014-2015 Gamma Sigma Epsilon Chemistry Honors Society

- Founding Vice President, University of Saint Joseph, West Hartford, CT.

2012-2015 Beta Beta Beta Biology Honors Society

- Member, President, Vice President University of Saint Joseph, West Hartford, CT.

2012-2015 Center for Academic Excellence

- Chemistry Content Tutor, University of Saint Joseph, West Hartford, CT.

AFFILIATIONS

2014-Present American Chemical Society MEDI Division

2018-Present Association of Women in Science